

DSWA-TR-98-14

## REGIONAL DISCRIMINATION STUDIES

Approved for public release; distribution is unlimited.

July 2000



Prepared for:  
Defense Threat Reduction Agency  
45045 Aviation Drive  
Dulles, VA 20166-7517

F19628-95-C-0184

Eugene Herrin, et. al.

DTIC QUALITY INSPECTED 4

Prepared by: Southern Methodist University  
Department of Geological Sciences  
P.O. Box 395  
Dallas, TX 75275

20001207 009

*Technical Report*

**DESTRUCTION NOTICE:**

Destroy this report when it is no longer needed. Do not return to sender.

PLEASE NOTIFY THE DEFENSE THREAT REDUC-  
TION AGENCY, ATTN: ADM, 45045 AVIATION  
DRIVE, DULLES, VA 20166-7517, IF YOUR ADDRESS  
IS INCORRECT, IF YOU WISH IT DELETED FROM  
THE DISTRIBUTION LIST, OR IF THE ADDRESSEE IS  
NO LONGER EMPLOYED BY YOUR ORGANIZATION.

# DISTRIBUTION LIST UPDATE

This mailer is provided to enable DTRA to maintain current distribution lists for reports. (We would appreciate you providing the requested information.)

- Add the individual listed to your distribution list.
- Delete the cited organization/individual.
- Change of address.

**Note:**  
Please return the mailing label from the document so that any additions, changes, corrections or deletions can be made easily. For distribution cancellation or more information call DTRA/ADM (703) 325-1036.

NAME: \_\_\_\_\_

ORGANIZATION: \_\_\_\_\_

**OLD ADDRESS**

**NEW ADDRESS**

\_\_\_\_\_  
\_\_\_\_\_  
\_\_\_\_\_

\_\_\_\_\_  
\_\_\_\_\_  
\_\_\_\_\_

TELEPHONE NUMBER: (    ) \_\_\_\_\_

**DTRA PUBLICATION NUMBER/TITLE**

**CHANGES/DELETIONS/ADDITIONS, etc.)**  
*(Attach Sheet if more Space is Required)*

\_\_\_\_\_  
\_\_\_\_\_  
\_\_\_\_\_

\_\_\_\_\_  
\_\_\_\_\_  
\_\_\_\_\_

DTRA or other GOVERNMENT CONTRACT NUMBER: \_\_\_\_\_

CERTIFICATION of NEED-TO-KNOW BY GOVERNMENT SPONSOR (if other than DTRA):

SPONSORING ORGANIZATION: \_\_\_\_\_

CONTRACTING OFFICER or REPRESENTATIVE: \_\_\_\_\_

SIGNATURE: \_\_\_\_\_

CUT HERE AND RETURN

DEFENSE THREAT REDUCTION AGENCY  
ATTN: ADM  
45045 AVIATION DRIVE  
DULLES, VA 20166-7517

DEFENSE THREAT REDUCTION AGENCY  
ATTN: ADM  
6801 TELEGRAPH ROAD  
ALEXANDRIA, VA 22310-3398

# REPORT DOCUMENTATION PAGE

*Form Approved*  
OMB No. 0704-0188

Public reporting burden for this collection of information is estimated to average 1 hour per response, including the time for reviewing instructions, searching existing data sources, gathering and maintaining the data needed, and completing and reviewing the collection of information. Send comments regarding this burden estimate or any other aspect of this collection of information, including suggestions for reducing this burden, to Washington Headquarters Services, Directorate for Information Operations and Reports, 1215 Jefferson Davis Highway, Suite 1204, Arlington, VA 22202-4302, and to the Office of Management and Budget, Paperwork Reduction Project (0704-0188), Washington, DC 20503

1. AGENCY USE ONLY (Leave blank)	2. REPORT DATE JULY 2000	3. REPORT TYPE AND DATES COVERED Technical 950928 - 980131	
4. TITLE AND SUBTITLE  Regional Discrimination Studies		5 FUNDING NUMBERS  C - F19629-95-C-0184	
6. AUTHOR(S) Eugene Herrin, Jesse Bonner, Paul Golden, Chris Hayward and Gordon G, Sorrells			
7. PERFORMING ORGANIZATION NAME(S) AND ADDRESS(ES) Southern Methodist University Department of Geological Sciences P. O. Box 395 Dallas, TX 75275-0395		8. PERFORMING ORGANIZATION REPORT NUMBER	
9. SPONSORING/MONITORING AGENCY NAME(S) AND ADDRESS(ES) Defense Threat Reduction Agency 45045 Aviation Drive Dulles, VA 20166-7517 CP/Hebert		10. SPONSORING/MONITORING AGENCY REPORT NUMBER  DSWA-TR-98-14	
11. SUPPLEMENTARY NOTES			
12a. DISTRIBUTION/AVAILABILITY STATEMENT  Approved for public release; distribution is unlimited.		12b. DISTRIBUTION CODE	
13. ABSTRACT (Maximum 200 words)  This final report on contract F19628-95-C-0184 consists of two parts, and five appendices. Part 1, "Regional Discrimination Studies" is a review of the contract via precis of integral parts of the Semiannual Reports. Part 2, consists of the Acknowledgements called for by the contract, which is a review of the work accomplished by SMU (1) in developing and deploying instrumentation for GSETT-2, (2) in the design and installation of GERESS and (3) in the design and installation of TEXESS [TXAR], prior to the Discrimination Contract. Appendix 1 is entitled Seismo-Acoustic Studies at TXAR. Appendix 2 is entitled Observation of Shuttle Quakes at TXAR. Appendix 3 is entitled Seismic "Bow" Waves: Parts I and II. Appendix 4 is entitled Preliminary Results of Alternative Infrasonic Sensor Designs. Appendix 5 is entitled Infrasound Recordings of Bolides and Explosions.			
14. SUBJECT TERMS Regional Ground Truth Data Bases Seismic and Infrasound Data Seismo-Acoustic Studies		Shuttle Quakes Bolides	15. NUMBER OF PAGES 136
17. SECURITY CLASSIFICATION OF REPORT UNCLASSIFIED		18. SECURITY CLASSIFICATION OF THIS PAGE UNCLASSIFIED	16. PRICE CODE
17. SECURITY CLASSIFICATION OF REPORT UNCLASSIFIED	18. SECURITY CLASSIFICATION OF THIS PAGE UNCLASSIFIED	19. SECURITY CLASSIFICATION OF ABSTRACT UNCLASSIFIED	20. LIMITATION OF ABSTRACT SAR

CONTENTS	PAGE
1. REGIONAL DISCRIMINATION STUDIES	1
1.1 INTRODUCTION	1
1.2 REPORTS AND OTHER DELIVERABLES	1
1.2.1 Reports	1
1.2.1.1. Scientific Report No. 1	1
1.2.1.1.1 Part 1. TXAR, The Prototype Alpha Array Of The New Improved Global Seismic System	2
1.2.1.1.2 Part 2. Calibration Studies At TXAR	3
1.2.1.1.3 Part 3. Ground Truth Database	4
1.2.1.2. Scientific Report No. 2	4
1.2.1.2.1 Part 1. Seismo-Acoustic Studies At TXAR	5
1.2.1.2.2 Part 2. Inversion Of Surface Waves For Shallow Velocity Structure In The Fort Worth Basin	5
1.2.1.2.3 Part 3. A Preliminary Investigation Of The Use Of Acoustic And Seismo-Acoustic Observations To Identify Vented Explosive Seismic Sources	6
1.2.1.3. Scientific Report No. 3	7
1.2.1.3.1 Part 1. Construction Of Regional Ground Truth Data Bases Using Seismic And Infrasound Data	8
1.2.1.3.2 Part 2. Seismic And Infrasound Data Observations At TXAR	8

<b>CONTENTS</b>	<b>PAGE</b>
1.2.2 Other Deliverables	9
<b>2. ACKNOWLEDGMENTS</b>	<b>9</b>
<b>2.1 PREVIOUS CONTRACTS AND PUBLICATIONS</b>	<b>9</b>
<b>2.1.1 Previous Contracts and Reports</b>	<b>9</b>
2.1.1.1 ARPA Contract # MDA 972-88-K-0001	9
2.1.1.2 ARPA Contract # MDA 972-89-C-0054	10
2.1.1.3 Contract # 19628-93-C-0057	12
<b>2.1.2 Publications</b>	<b>13</b>
<b>2.1.2.1 Special Reports, Papers, and Posters</b>	<b>13</b>
2.1.2.1 Publications	16
<b>APPENDIX 1. SEISMO-ACOUSTIC STUDIES AT TXAR</b>	<b>17</b>
<b>APPENDIX 2. OBSERVATION OF SHUTTLE QUAKES AT TXAR</b>	<b>41</b>
<b>APPENDIX 3. SEISMIC "BOW" WAVES: PARTS I AND II</b>	<b>66</b>
<b>APPENDIX 4. PRELIMINARY RESULTS OF ALTERNATIVE     INFRASONIC SENSOR DESIGNS</b>	<b>82</b>
<b>APPENDIX 5. INFRASOUND RECORDINGS OF BOLIDES AND     EXPLOSIONS</b>	<b>119</b>

# 1. REGIONAL DISCRIMINATION STUDIES

## 1.1 INTRODUCTION

Contract #F19628-95-C-0184 for "Regional Discrimination Studies" was awarded to SMU with a start date of 30 September 1995 and ending date of 29 September 1997. Research was contingent upon the use of data from the TXAR array that was installed by SMU in August 1993 under Contract #F19628-93-C-0057. Research was undertaken to calibrate the array, and establish a "Ground Truth Data Base." It soon became evident that acoustic data was needed to construct such a data base, and an a four-element infrasonic array was installed at TXAR in February 1996.

## 1.2 REPORTS AND OTHER DELIVERABLES

### 1.2.1 Reports

Research has been documented in Scientific Reports Nos. 1, 2, and 3. They consist of parts as described below plus an Acknowledgment part containing information on previous contracts and publications as is presented in Part 2 of this report.

#### 1.2.1.1 Scientific Report No. 1

PL-TR-96-2249, dated April 1996, consisted of three parts. Part 1 by Chris Hayward described TXAR in detail. Part 2 by Ileana Tibuleac and Eugene Herrin described the calibration study using 144 events recorded at TXAR for which USGS  $m_b$  values were available. Part 3 by G. G. Sorrells and Eugene Herrin described the construction of the ground truth data base using a variety of sources including mine explosions, normal earthquakes, earthquake swarms, and very shallow earthquakes induced by hydrocarbon production. The three parts are summarized in the following sections.

#### 1.2.1.1.1 Part 1. TXAR: The Prototype Alpha Array Of The New Improved Global Seismic System

SMU began research on mini-array technology in 1991 under Contract # MDA 972-89-C-0054, and was awarded Contract # F19628-93-C-0057 to install TEXESS on 5 April 1993. The array was installed by SMU personnel at their LTX site the week of 22 August 1993, and the first event was a local recorded on 31 August. With an aperture of 4 km, TEXESS [now TXAR] consists of nine sensor sites, which includes a central three-component, short-period seismometer installation in a vault at the hub, and eight vertical short-period seismometer installations in surrounding boreholes. In addition to the short-period instrumentation at the hub, a posthole K-S54000 long-period seismometer, owned by SMU, was installed in a shallow borehole. The term *posthole* was coined because the K-S54000 is slimmer than the K-S36000 and is installed in a shallow hole without a hole lock in such a manner that it can be leveled manually rather than remotely. Four infrasonic stations were subsequently established using porous hose arrays and inexpensive, low-frequency acoustical sensors collocated with the seismometers in the boreholes. The TXAR layout including infrasonic stations are shown in Figure 1-1 of Appendix 1.

TXAR was designed as an improvement upon regional arrays of the NORESS-ARCESS-GERESS type. Advancements in the TXAR design included the following:

1. The placement of seismometers, acoustical sensors, and electronics in boreholes to greatly reduce construction costs for piers and vaults,
2. The use of solar power at each site rather than a central-power source,
3. The use of GPS receivers for time data at each seismometer site to replace central timing from the hub,
4. The employment of radio links from seismometer sites to the hub to replace cable links and associated construction costs,
5. The use of modular equipment to facilitate the installation and maintenance of the array.

The above advancements in array design reduced costs by over an order of magnitude when compared with GERESS. Cost per element at GERESS was \$341,280 whereas cost per element at TXAR was \$33,000. With improved digital instrumentation to assure undistorted phase information and time-domain processing, azimuthal deviations for test events have been reduced significantly. As a result, TXAR is better than either a single, three-component station or larger arrays. After 35 years, we're back to the original Geneva-type array, or, in the words of Yogi Berra, "it's *dèjà vu* all over again."

#### 1.2.1.1.2 Part 2. Calibration Studies At TXAR

Calibration studies at TXAR used a modified version of the correlation method described by Cansi, Plantet and Massinon in order to estimate azimuth and horizontal phase velocity of 144 events for which USGS mb values were available. Modifications to the correlation method include the Fourier interpolation of the data by a factor of 8 to obtain a virtual sample rate of 320/sec, use of an L1 norm (least absolute deviation) to obtain estimates of the azimuth and phase velocity and a moving window display to indicate those portions of the waveform that show strongest correlation across the array.

Corrected phase velocities normally associated with Pn (less than 8.6 km/s) are generally seen for events at epicentral distance as far as 2000 km. For greater distances, upper mantle refracted first arrivals (P) with corrected phase velocities greater than 8.6 km/s are generally observed for epicentral distances beyond 1600 km. Phase identification is essential in order to select a suitable magnitude scale.

Based on the 144 well located events (USGS) and using the Denny, Taylor and Vergino formula, the most reliable magnitude estimates are as follows:

1. For horizontal phase velocity less than 8.6 km/sec:

$$mb(D) = \log A + 2.4 (\log D) - 3.95 + C \quad \text{with } C = +0.3$$

2. For horizontal phase velocity greater than 8.6 km/sec:

$$mb(D) = \log A + 2.4 (\log D) - 3.95 + C \quad \text{with } C = -0.50$$

The M-discontinuity beneath TXAR was determined to the first order to strike along an azimuth of 111 degrees (NW-SE) and dip 10 degrees to the northeast. This result is consistent with the tectonic setting for the area.

#### 1.2.1.1.3 Part 3. Ground Truth Database

The preliminary results of this study also demonstrate that the calculation of a running estimate of the normalized correlation coefficient between the outputs of collocated seismic and infrasonic sensors provides a simple but effective method for the detection of weak short period acoustic waves. The success of this approach at TXAR is attributed to the fact that while short period acoustic and seismo-acoustic signals share a common waveform, short period seismic and infrasonic noise are, for all practical purposes, statistically uncorrelated under both calm and windy atmospheric conditions. Statistically uncorrelated short period seismic and infrasonic noise is expected to be a property of all "hard rock" geologic environments including those which are likely to be the sites of future IMS installations. However, while acoustic and seismo-acoustic signals are always linearly related, they will share a common waveform only in those environments where the seismic velocities of the formation containing the seismic observation point are uniform over a depth range that is large compared to the wavelengths of the acoustic signals. In other environments, it will be necessary to determine the frequency response characteristics of the seismo-acoustic transfer function in order to optimize the performance of the correlator code. In this regard, it has been shown that the existing model for the prediction of seismo-acoustic transfer functions suffered from serious defects when it was tested at TXAR. Until the discrepancies between the observed and predicted values of the seismo-acoustic scaling factors at TXAR can be explained, experimental measurements should be used to determine the frequency response characteristics of local seismo-acoustic transfer functions.

#### 1.2.1.2 Scientific Report No. 2

PL-TR-96-2314, dated October 1996, consisted of three parts and an appendix. Part 1 by Eugene Herrin and G. G. Sorrells<sup>1</sup> described seismo-acoustic studies at TXAR. Part 2 by Jessie L. Bonner described a study of surface waves recorded at TXAR from quarry explosions near Waco, Texas. Part 3 by G. G. Sorrells and Eugene Herrin described the use of acoustic and seismo-acoustic data to identify vented explosive seismic sources. The appendix by Chris Hayward described the acoustical sensors installed at TXAR.

#### 1.2.1.2. 1 Part 1. Seismo-Acoustic Studies At TXAR

The use of seismic, acoustic and seismo-acoustic detections has been clearly established as a means of positively identifying surface and vented underground explosions. These identified events then become part of a ground-truth data base. This procedure can be used at collocated seismic and acoustic arrays that detect explosions of mb 2.5 or larger from regional sources.

Detection of acoustic signals allows the identification of clusters of similar seismic signals from explosions. Under light wind conditions the acoustic detection threshold is a few tenths of a microbar. Under moderate wind conditions the seismo-acoustic detection threshold is about a microbar. Acoustic signals from explosions in Coahuila, Mexico, with seismic magnitudes above about 2.5 are detectable during months with a favorable zonal stratospheric wind direction. We expect to detect acoustic signals from explosions in New Mexico and Arizona this winter when the zonal stratospheric winds are from the west.

#### 1.2.1.2. 2 Part 2. Inversion Of Surface Waves For Shallow Velocity Structure In The Fort Worth Basin

The Love and Rayleigh wave inversions were treated as separate problems to determine if the upper crust in the Fort Worth basin is transversely anisotropic. The initial results show two different velocity structures are obtained through the separate inversion of the Rayleigh (P-SV) and Love

---

<sup>1</sup> With contributions from Jessie L. Bonner, Valeriu Burlacu, Nancy Cunningham, Paul Golden, Chris Hayward, Jack Swanson, Karl Thomason, and Ileana Tibuleac.

(SH) waves that have traveled along the same path. This is not unexpected considering the highly- fractured nature of the rocks in the upper crust of central Texas and the total percentage of clays in the stratigraphic column. But the magnitude of this phenomenon is unexpected and raises doubts about the validity of the results. Further research will work to alleviate these doubts, as methods for inverting Love and Rayleigh waves simultaneously using code that considers transversely anisotropic media are employed. Further geophysical data from the basin will be sought to constrain the models more efficiently, and as a means of testing the final answer.

#### 1.2.1.2. 3 Part 3. A Preliminary Investigation Of The Use Of Acoustic And Seismo-Acoustic Observations To Identify Vented Explosive Seismic Sources

The results presented above demonstrate that short period acoustic signals with pressure amplitudes of a few  $\mu$ bars or less will generate seismo-acoustic signals that are detectable at a seismically "quiet" site. This observation implies that they will also be detectable at future IMS sites which are most likely to be located in quiet seismic environments. While the short period acoustic SNR will be higher at the outputs of the infrasonic monitoring system during periods of calm to light surface winds, it may be inferred from the results that the seismo-acoustic SNR will be higher during periods of moderate to high surface winds. The results shown also indicate that seismic beamforming may significantly enhance seismo-acoustic SNR's despite the fact that the seismic array is not optimally configured for short period acoustic observations. This result is attributed to the fact that unlike seismic signals, seismo-acoustic signals are not significantly affected by multi-pathing and remain spatially stable over the characteristic dimensions of a typical IMS seismic array. Thus, it may be inferred that the seismic monitoring systems installed at future IMS sites may be used as a backup infrasonic system during those periods when local atmospheric turbulence impairs the detection capability of the primary acoustic monitoring system.

The preliminary results of this study also demonstrate that the calculation of a running estimate of the normalized correlation coefficient between the outputs of collocated seismic and infrasonic sensors provides a simple but effective method for the detection of weak short period acoustic waves. The

success of this approach at TXAR is attributed to the fact that while short period acoustic and seismo-acoustic signals share a common waveform, short period seismic and infrasonic noise are, for all practical purposes, statistically uncorrelated under both calm and windy atmospheric conditions. Statistically uncorrelated short period seismic and infrasonic noise is expected to be a property of all "hard rock" geologic environments including those which are likely to be the sites of future IMS installations. However, while acoustic and seismo-acoustic signals are always linearly related, they will share a common waveform only in those environments where the seismic velocities of the formation containing the seismic observation point are uniform over a depth range that is large compared to the wavelengths of the acoustic signals. In other environments, it will be necessary to determine the frequency response characteristics of the seismo-acoustic transfer function in order to optimize the performance of the correlator code. In this regard, it has been shown that the existing model for the prediction of seismo-acoustic transfer functions suffered from serious defects when it was tested at TXAR. Until the discrepancies between the observed and predicted values of the seismo-acoustic scaling factors at TXAR can be explained, experimental measurements should be used to determine the frequency response characteristics of local seismo-acoustic transfer functions.

Finally, the results of this study infer that the detection of a short period acoustic signal and its association with an antecedent near regional seismic event is a promising method for the identification of vented explosive sources. If further research confirms this premise then it follows that the data that will be provided by the collocated seismic and infrasonic monitoring systems at future IMS sites may be used to significant advantage to eliminate the seismic signals generated by vented explosions from further consideration as possible indicators of a clandestine underground nuclear explosion.

### 1.2.1.3 Scientific Report No. 3

PL-TR-97-2064, dated March 1997 consisted of two parts. Part 1 by G. G. Sorrells, Eugene Herrin, and Jessie L. Bonner<sup>2</sup> described the construction of a

---

<sup>2</sup> With contributions from Jack Swanson, Sarah Deering, and Angela Maddox.

regional ground truth data base using seismic and infrasonic data recorded at TXAR. Part 2 by Jessie L. Bonner, Sarah Deering, Tao Liu, Jack Swanson, and Ileana Tibuleac described seismic and infrasonic data observations at TXAR recorded during the second Seismo-Acoustic Ground Truth (SAGII) tests.

#### 1.2.1.3.1 Part 1. Construction Of Regional Ground Truth Data Bases Using Seismic And Infrasonic Data

The results of the TXAR seismo-acoustic experiment illustrate that infrasonic signals generated by commercial explosions are detectable in the 0.5-5.0 hertz bandwidth and can be observed at distances up at least 680 kilometers from the source. Furthermore, it may be inferred from these results that the sources of the majority of commercial explosive seismic events will be identifiable by the detection of associated infrasonic signals when:

- the magnitudes of the seismic events are greater than about  $m_b = 2.5$
- their source to receiver distances exceed about 175-200 kilometers;
- the events occur during a time period and at locations such that the reception point is located stratospherically "downwind" from the sources.

It follows then that application of the seismo-acoustic source identification method to data acquired over a complete stratospheric zonal wind cycle at a particular site will provide the information required to construct a ground truth data base. This data base will accurately identify the sources of the seismic events that occur at regional distances to the site whose magnitudes are found in a range that is of significance to the verification of the CTBT.

#### 1.2.1.3.2 Part 2. Seismic And Infrasonic Data Observations At TXAR

The second seismic and acoustic ground truth test (SAGII) using the TXAR array was initiated on 1 February 1997. A goal of this test is to determine the percentage of seismic events recorded at TXAR between November 1-

December 15, 1996 that had associated acoustic signals. During this time period, stratospheric zonal winds blew from west to east, thus enhancing the opportunity to record infrasound signals from the west of TXAR. This temporal factor also decreased the chance of recording infrasound signals originating east of the array, an inference confirmed by the preliminary results of SAGTII. To date, infrasound signals have only been associated with regional events from the west of the array for a time period between 1 and 7 November 1996.

### 1.2.2 Other Deliverables

Software developed for the contract will be delivered in accordance with the Contract Data Requirements List (CDRL).

## 2. ACKNOWLEDGEMENTS

### 2.1 PREVIOUS CONTRACTS AND PUBLICATIONS

#### 2.1.1 Previous Contracts and Reports

##### 2.1.1.1. ARPA Contract # MDA 972-88-K-0001

Development of an Intelligent Seismic Facility and Preparation for Participation in the Conference on Disarmament Group of Scientific Experts Technical Tests (GSETT).

Quarterly R&D Status Report, 1 Nov. 1988 through 31 Jan 1989.

Quarterly R&D Status Report, 1 Feb. through 30 Apr. 1989.

Quarterly R&D Status Report, 1 May through 31 July 1989.

Quarterly R&D Status Report, 1 Aug. through 31 Oct. 1989.

Quarterly R&D Status Report, 1 Nov. 1989 through 31 Jan. 1990.

Quarterly R&D Status Report, 1 Feb. through 30 Apr. 1990.

Quarterly R&D Status Report, 1 May through 31 July 1990.

Quarterly R&D Status Report, 1 Aug. through 31 Oct. 1990.

Quarterly R&D Status Report, 1 Nov. 1990 through 31 Jan. 1991.

Quarterly R&D Status Report, 1 Feb through 30 April 1991.

Quarterly R & D Status Report, 1 May through 31 July 1991.

Quarterly R & D Status Report, 1 August through 31 October 1991.

Quarterly R & D Status Report, 1 October 1991 thru 31 January 1992.

Quarterly R & D Status Report, 31 January through 30 April 1992.

Quarterly R & D Status Report, 30 April through 31 July 1992.

Quarterly R & D Status Report, 31 July through 31 October 1992.

Semiannual Report, January 1991, SMU-R-89-226.

Semiannual Report, October 1991; SMU-R-91-252

Semiannual Report, December 1991; SMU-R-91-301

Semiannual Report, January 1992; SMU-R-92-337

Semiannual Report, November 1989; SMU-R-91-121

Semiannual Report, January 1992; SMU-R-92-373

Semiannual Report, August 1992; SMU-R-92-396

Final Report, December 1992; SMU-92-425.

2.1.1.2 ARPA Contract # MDA 972-89-C-0054

Complete and Deploy the GERESS Seismic Array in Southeast Germany, Establish Workstations Which Accept the Array Data at Bochum and at NORSAR, and Provide the Interface to the Intelligent Array System at NORSAR.

Quarterly R&D Status Report, 4 Jan. to 15 Apr. 1989.

Quarterly R&D Status Report, 15 Apr. to 15 July 1989.

Quarterly R&D Status Report, 15 July to 15 Oct. 1889.

Quarterly R&D Status Report, 15 Oct. 1889 to 15 Jan. 1990.

Quarterly R&D Status Report, 15 Jan. to 15 Apr. 1990.

Quarterly R&D Status Report, 15 Apr. to 15 July 1990.

Quarterly R&D Status Report, 15 July to 15 Oct. 1890.

Quarterly R&D Status Report, 15 Oct. 1890 to 15 Jan. 1991.

Quarterly R&D Status Report, 15 Jan. to 15 April 1991.

Quarterly R & D Status Report, 15 April to 15 July 1991.

Quarterly R & D Status Report, 15 July to 15 October 1991.

Quarterly R & D Status Report, 15 October 1991 to 15 January 1992.

Quarterly R & D Status Report, 15 January to 15 April 1992.

Quarterly R & D Status Report, 15 April to 15 July 1992.

Quarterly R & D Status Report, 15 July to 15 October 1992.

Quarterly R & D Status Report, 15 October 1992 to 15 January 1993.

Quarterly Technical Report, 4 January to 15 Apr. 1989..

Quarterly Technical Report, 15 Apr. to 15 July 1989..

Quarterly Technical Report, 15 July to 15 October 1989.

Quarterly Technical Report, 15 October 1989 to 15 Jan. 1990.

Quarterly Technical Report, 15 Jan. to 15 April 1990.

Quarterly Technical Report, 15 April to 15 July. 1990.

Quarterly Technical Report, 15 July to 15 October 1990.

Quarterly Technical Report, 15 October 1990 to 15 Jan. 1991.

Quarterly Technical Report, 15 Jan. to 15 April 1991.

Quarterly Technical Report, 15 April to 15 July 1991.

Quarterly Technical Report, 15 October 1991 to 15 January 1992.

Quarterly Technical Report, 15 January to 15 April 1992.

Quarterly Technical Report, 15 April to 15 July 1992.

Quarterly Technical Report, 15 July to 15 October 1992.

2.1.1.3 Contract # 19628-93-C-0057

Design, Evaluation, and Construction of TEXESS and LUXESS, and Research in Mini-Array Technology and Use of Data from Single Stations and Sparse Networks

Quarterly R & D Status Report, 30 April to 31 July 1993.

Quarterly R & D Status Report, 31 July to 31 October 1993.

Quarterly R & D Status Report, 31 October 1993 to 31 January 1994.

Quarterly R & D Status Report, 31 January to 30 April 1994.

Quarterly R & D Status Report, 30 April to 31 July 1994.

Quarterly R & D Status Report, 31 July to 31 October 1994.

Quarterly R & D Status Report, 31 October 1994 to 31 January 1995.

Quarterly R & D Status Report, 31 January to 30 April 1995.

Quarterly R & D Status Report, 30 April to 31 July 1995.

Quarterly R & D Status Report, 31 July to 31 October 1995.

Quarterly R & D Status Report, 31 October 1995 to 31 January 1996.

Scientific Report No. 1, October 1993, PL-TR-94-2106, ADA284580.

Scientific Report No. 2, April 1994, PL-TR-94-2258, ADA292546.

Scientific Report No. 3, October 1994, PL-TR-95-2023, ADA295787.

Scientific Report No. 4, April 1995, PL-TR-95-2091, ADA305417.

Scientific Report No. 5, October 1995, PL-TR-96-2022, ADA306407.

## 2.1.2 Publications

### 2.1.2.1 Special Reports, Papers, and Posters

- Arnett, Dick, 1992, German Experimental Seismic System (GERESS): Pamphlet, GERESS Symposium on Regional Seismic Arrays, 22-24 June 1992, Waldkirchen, Bavaria, Federal Republic of Germany.
- Bonner, Jessie, Eugene Herrin and Tom Goforth, 1995, Azimuthal variations in Rg energy in Central Texas: Appendix A, Scientific Report No. 5, 13-40, ARPA Contract # MDA 972-89-C-0054
- Golden, Paul, Eugene Herrin, and Wilbur Rinehart, 1991, The use of LTX data in preparing and compiling the final event bulletins: SMU-R-91-278, Contract # MDA 972-88-K-001
- Golden, Paul, 1992, Unconventional processing and visualization techniques: GERESS Symposium on Regional Seismic Arrays, 22-24 June 1992, Waldkirchen, Bavaria, Federal Republic of Germany.
- Hayward, Chris, Eugene Herrin, G. G. Sorrells, and Ileana Tibuleac, 1996, Regional discrimination studies: Scientific Report No. 1, PL-TR-96-2249.
- Herrin, Eugene, Chris Hayward, and Eugene Smart, 1991, Comparison of the Murdock and optimum seismic signal detectors: Appendix 3, SMU-R-90-121, 54-67.
- Herrin, Eugene, 1992, Construction of the GERESS array: GERESS Symposium on Regional Seismic Arrays, 22-24 June 1992, Waldkirchen, Bavaria, Federal Republic of Germany.
- Herrin, Eugene and Paul Golden, 1993, Design, evaluation and construction of two nine element experimental arrays TEXESS and LUXESS: Proceedings, 15 Annual Seismic Research Symposium 8-10 September

1993, Vail, Colorado, Sponsored by Phillips Laboratory, AFOSR & ARPA, PL-TR-93-2160, ADA271458.

Herrin, Eugene, Paul Golden, Karl Thomason, and Chris Hayward, 1993, Seismic array technology: Poster.

Herrin, Eugene, 1994a, Installation of posthole 54000 seismometer, Appendix 5, Scientific Report No. 2, 59-60, ARPA Contract # MDA 972-89-C-0054.

Herrin, Eugene, 1994b, Dealing with outliers and possible evasion scenarios: Appendic A, Scientific Report No. 3, 19-35, ARPA Contract # MDA 972-89-C-0054.

Herrin, Eugene, Paul Golden and J. Theodore Cherry, 1994, The ARPA Model 94 regional array concept: Scientific Report No. 3, 36-43, ARPA Contract # MDA 972-89-C-0054.

Herrin, Eugene, *et al.*, 1994, Research in regional event discrimination using Ms:m<sub>b</sub> and autoregressive modeling of Lg waves: Proceedings, 16 Annual Seismic Research Symposium, 7-9 September 1994, Thornwood, New York, Sponsored by Phillips Laboratory, AFOSR, PL-TR-94-2217, ADA284667.

Herrin, Eugene, *et al.*, 1995, Seismo-acoustic synergy: Appendix B, Scientific Report No. 5, 41-71, ARPA Contract # MDA 972-89-C-0054.

Herrin, Eugene, G. G. Sorrells, et al., 1996, Seismo-acoustic studies at TXAR: Proceedings, 18 Annual Seismic Research Symposium, Poster #39, 4-6 September 1996, Annapolis, MD, Sponsored by Phillips Laboratory, AFOSR, and AFTAC, PL-TR-96-2153, ADA313692

Sorrells, G. G. and Eugene Herrin, 1995, Seismic detection of acoustical waves: Appendix B, Scientific Report No. 4, 33-42, ARPA Contract # MDA 972-89-C-0054.

Sorrells, G. G., 1995, Seismo-acoustic methods for the detection of acoustic waves: Appendix C, Scientific Report No. 5, 72-86, ARPA Contract # MDA 972-89-C-0054.

Tibuleac, Ileana and Eugene Herrin, 1996, Calibration studies at TXAR: Scientific Report No. 1, PL-TR-96-2249.

Herrin, Eugene, 1997, Ground truth for regional seismic events recorded at TXAR: Proceedings, 19th Annual Seismic Research Symposium on Monitoring a Comprehensive Test Ban Treaty, Poster #, 23-25 September 1997, Orlando, FL, Sponsored by Phillips Laboratory, AFOSR, and AFTAC.

#### 2.1.2.2 Publications

Herrin, Eugene T. and Vigdor L. Teplitz, 1996, Seismic detection of nuclearites: *Physical Review D*, 53 (12), 6762-6770.

Bonner, J., Herrin, E., and Goforth, T., 1996, Azimuthal variations of Rg energy from quarry blasts in Central Texas: *Seismol. Res. Let.*, 67, 43-57.

Tibuleac, Ileana and Eugene Herrin, 1997, Calibration studies at TXAR: *Seismol. Res. Let.*, 68, 353-365.

Sorrells, G. G., E.T. Herrin, and J. L. Bonner, 1997, Construction of regional ground truth data base using seismic and infrasound data: *Seismol. Res. Let.*, 68, 743-752.

## APPENDIX 1. SEISMO-ACOUSTIC STUDIES AT TXAR<sup>1</sup>

Eugene Herrin and G. G. Sorrells

with contributions from

Jessie Bonner, Nancy Cunningham, Sarah Deering, Paul Golden, Chris Hayward, Tao Liu, Angela Maddox, Jack Swanson, Karl Thomason, and Ileana Tibuleac

### 1.1 INTRODUCTION

TXAR is located in far West Texas only a few miles north of the border with Mexico. The seismic sources for regional events recorded at TXAR are scattered mainly throughout northern Mexico, Texas, New Mexico, and Arizona. Early analysis indicated that at least 75% of these events were commercial explosions. Whereas the mine operators in the U.S. have been helpful in identifying their explosions, we have not been able to obtain similar information from mines in Mexico. We established a four element infrasonic array within TXAR so that infrasound signals from surface explosions could be associated with seismic data in order to identify mining explosions, particularly in Mexico (see Figure 1). This method has proved to be very useful during periods when stratospheric winds are in the source-receiver direction. Identification of a variety of seismic sources is possible using the seismo-acoustic data. These include mining and construction explosions, local explosions, shuttle quakes, and bolide quakes. This poster illustrates techniques used to construct a ground-truth database at TXAR for the Southwestern United States.

---

<sup>1</sup> Herrin, Eugene, 1997, Ground truth for regional seismic events recorded at TXAR: Abstracts [poster] of the 19th Annual Seismic Research Symposium on Monitoring a Comprehensive Test Ban Treaty, 30 August 1997, p. 37.

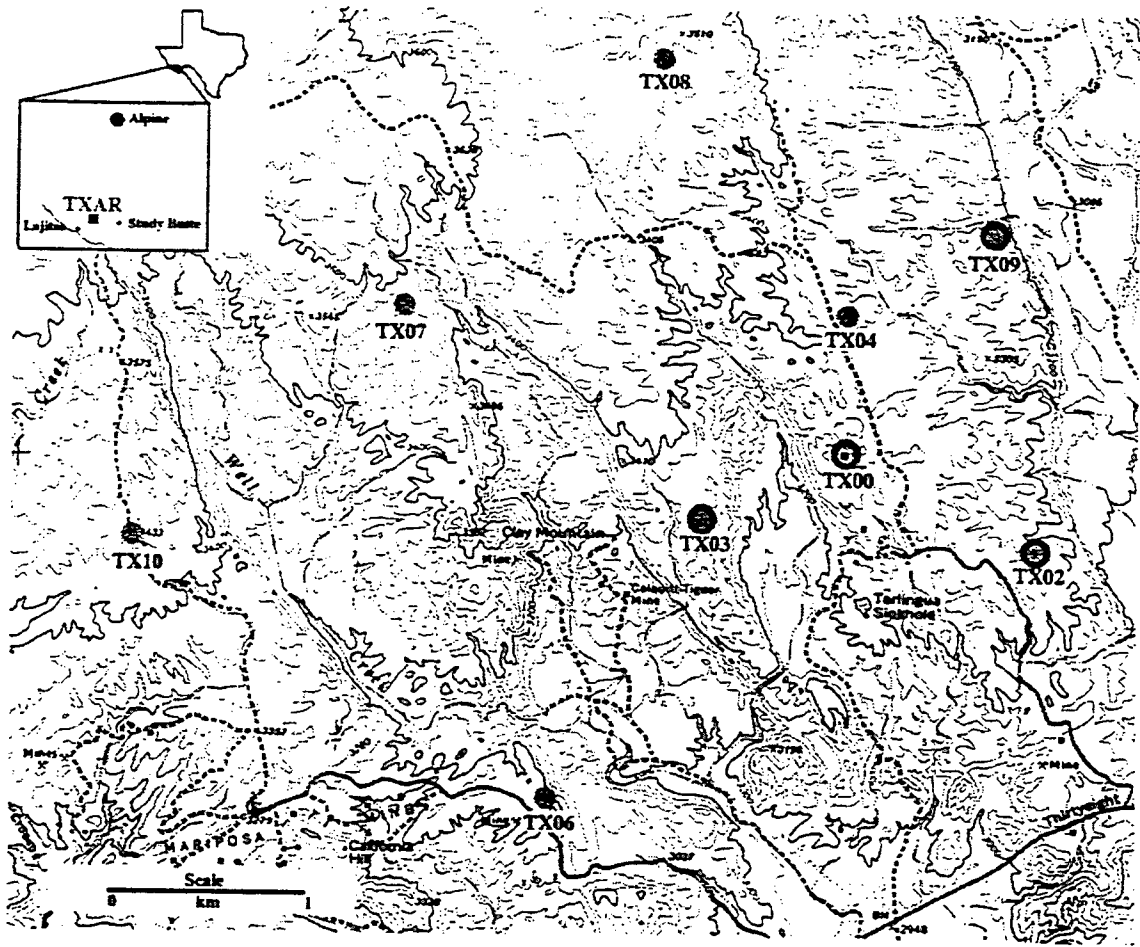


Figure 1-1. TXAR location map. Acoustic sensors are located at TX00, TX02, TX03, and TX09.

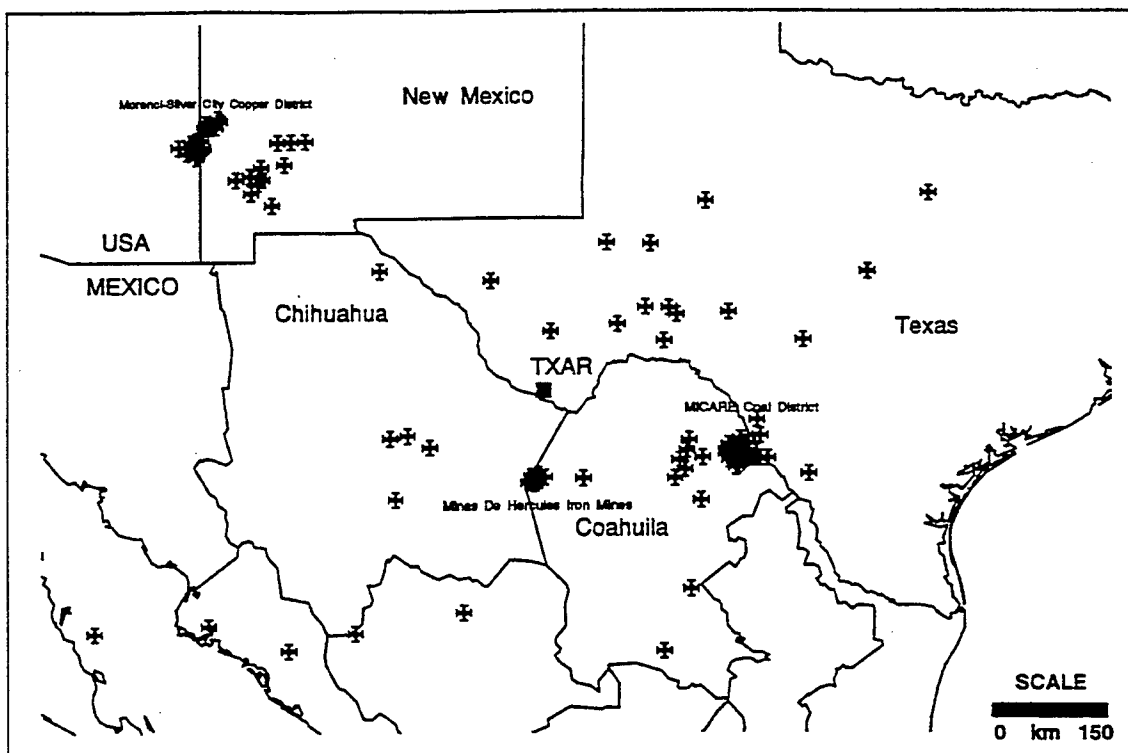
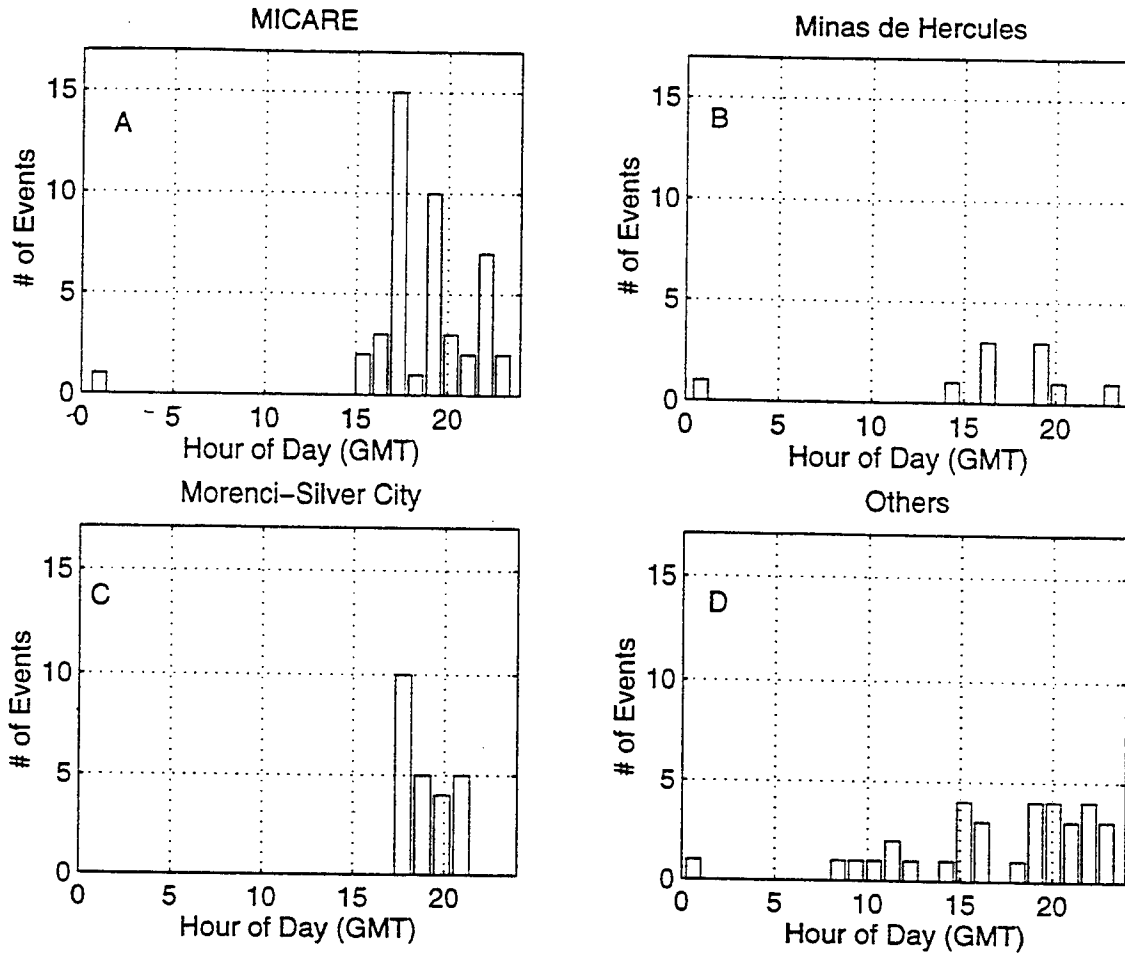


Figure 1-2. Locations for events recorded at TXAR between July 15, 1996 and August 10, 1996. The majority of the epicenters occur in four clusters within or near known mining complexes. The cluster found east-southeast of TXAR at a range of 300-320 km is approximately coincident with the MICARE (Minera de Carbonifera Rio Escondito) coal mining district located in Coahuila, Mexico near the border with the United States. The cluster found due South of TXAR at a range of about 140-160 km occurs near the Minas de Hercules iron mines. The two clusters found about 550-700 km northwest of TXAR coincide with the Morenci-Silver City Porphyry copper mining district in southeastern Arizona and southwestern New Mexico.



**Figure 1-3. Occurrence times for regional events recorded at TXAR. The majority of mining activity occurs between 15:00 and 23:00 hours UTC (10:00 AM to 8:00 PM, CDT), suggesting that the events in each of the clusters are commercial explosions.**

Local Explosion-- February 11, 1997

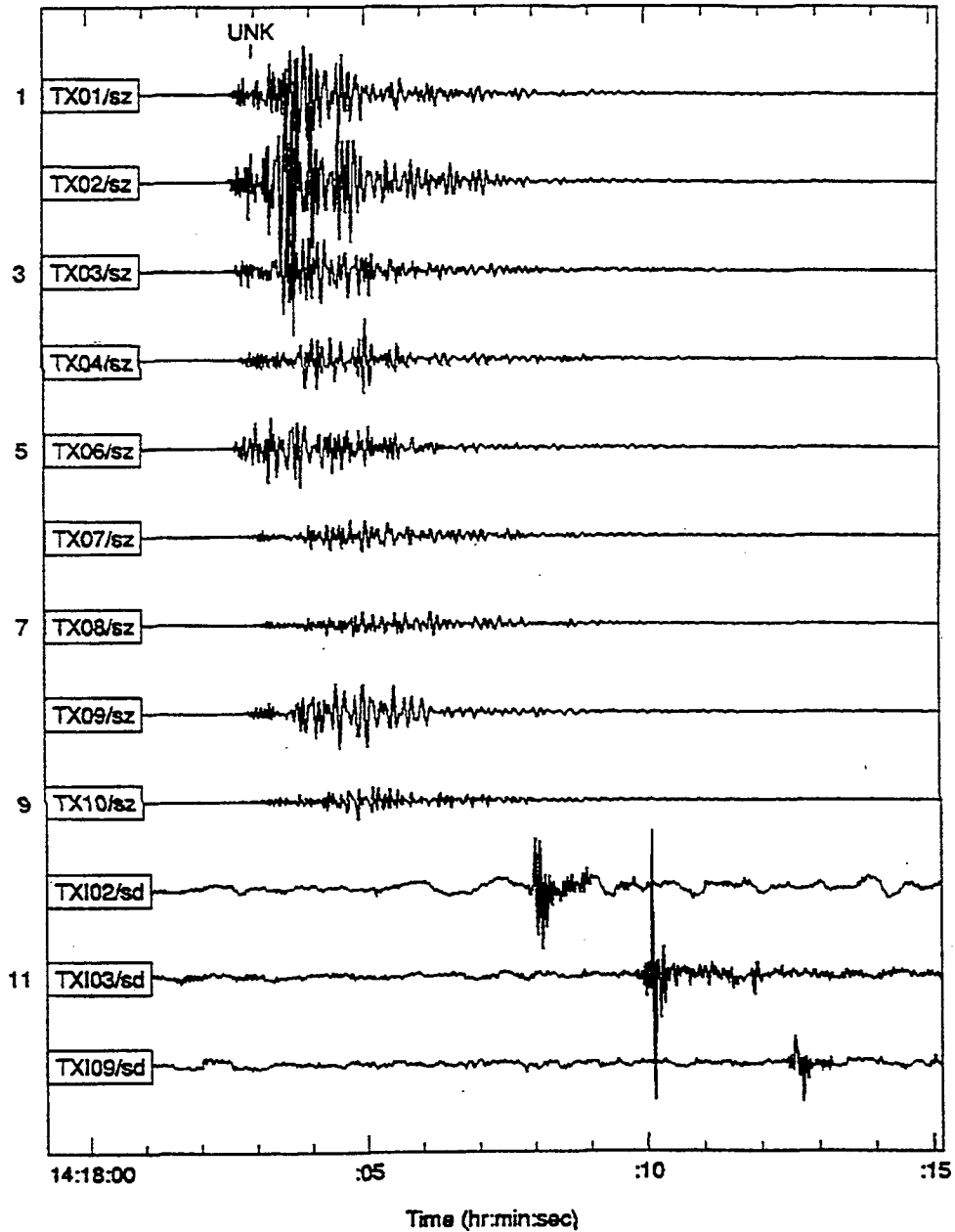


Figure 1-4. Seismic event on February 11, 1997 originating within 10 km of the TXAR array. For several years, similar events were thought to be microseismic activity along nearby faults. Implementation of the TXAR infrasound array in March, 1996, allowed us to determine the origin of these events, with duration magnitudes  $< -0.5$ , to be explosions southwest of Terlingua, Texas. The amplitudes are plotted at a uniform scale to show the attenuation of the signal across the array.

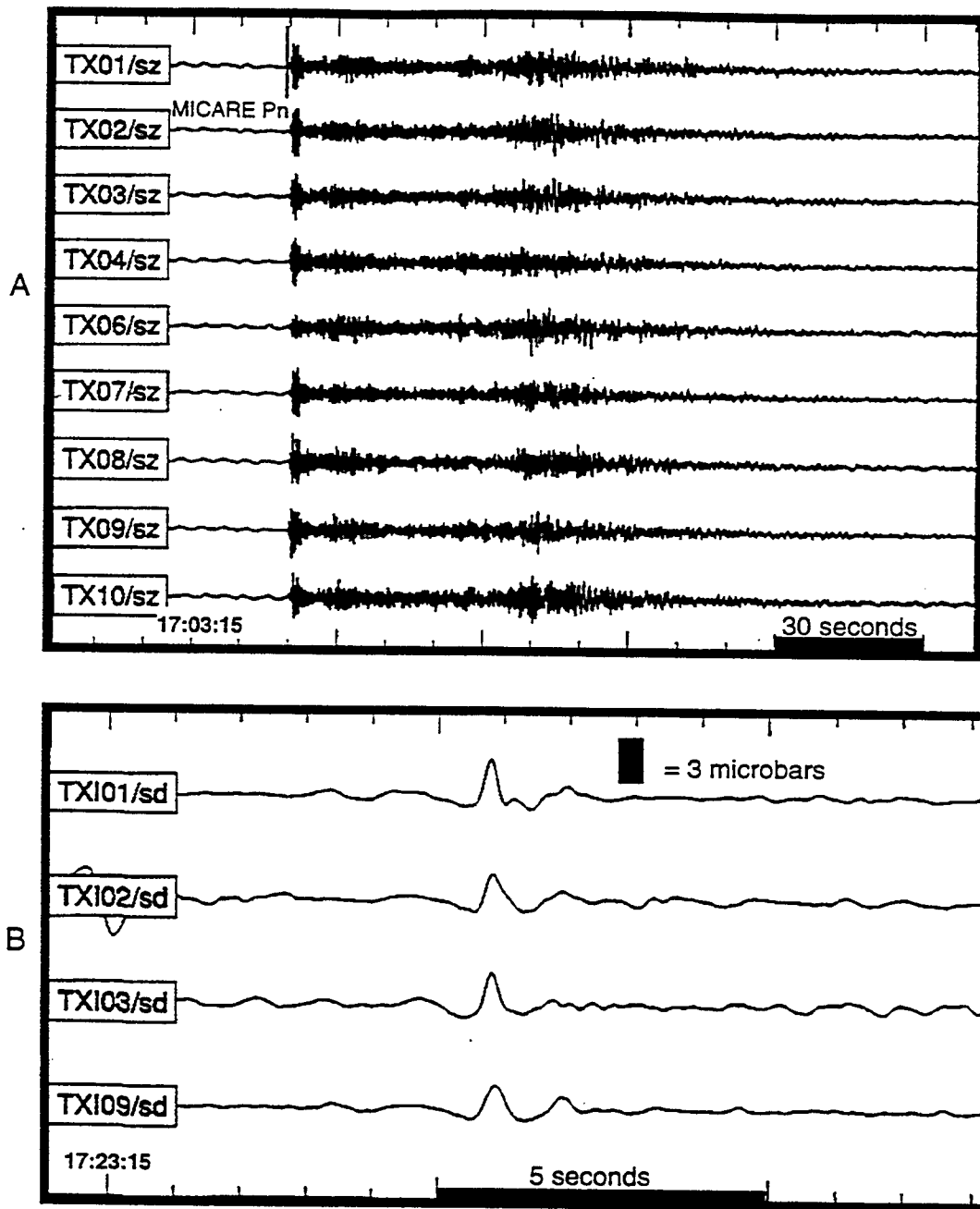


Figure 1-5. Seismograms (A) and microbarograms (B) from an explosion in the MICARE mining district of northern Mexico.

Balanced Zonal Wind (m/s)  
30 N 1979-1995

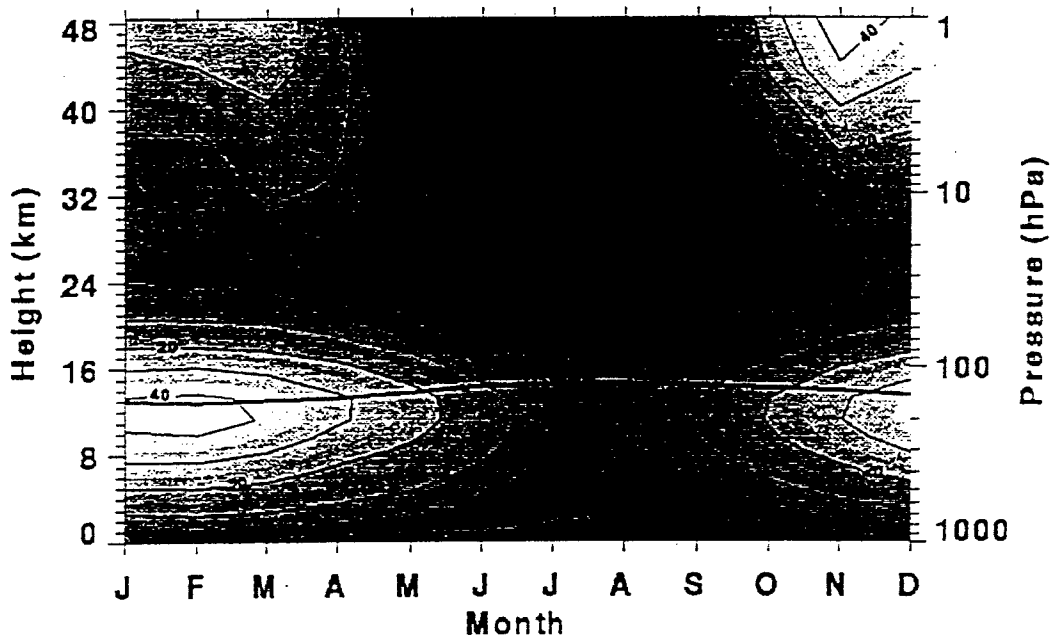


Figure 1-6. Balanced zonal winds at 30°N latitude. Wind from the west (positive) is indicated by light colors, while winds from the east (negative) are shown by dark colors.

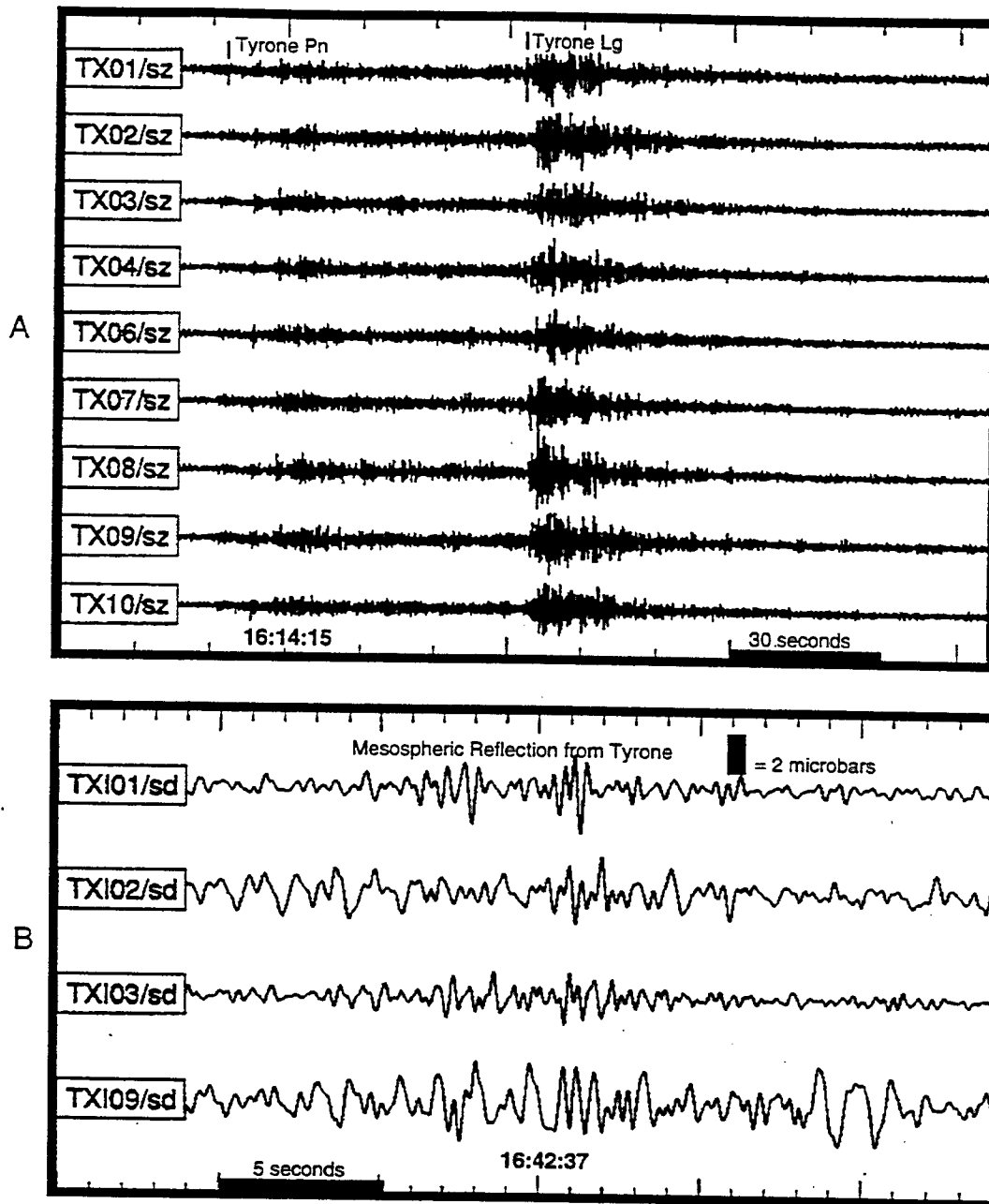


Figure 1-7. A) Seismograms generated by an explosion at the Tyrone open-pit copper mine in Silver City, New Mexico. B) Microbarograms of the infrasound signal associated with reflection from the upper atmosphere. The group velocity of this signal is 0.3 km/s referenced to the origin time and location of the explosion. The microbarograms have been time aligned for an horizontal phase velocity of 0.34 km/s and a back-azimuth of 306.

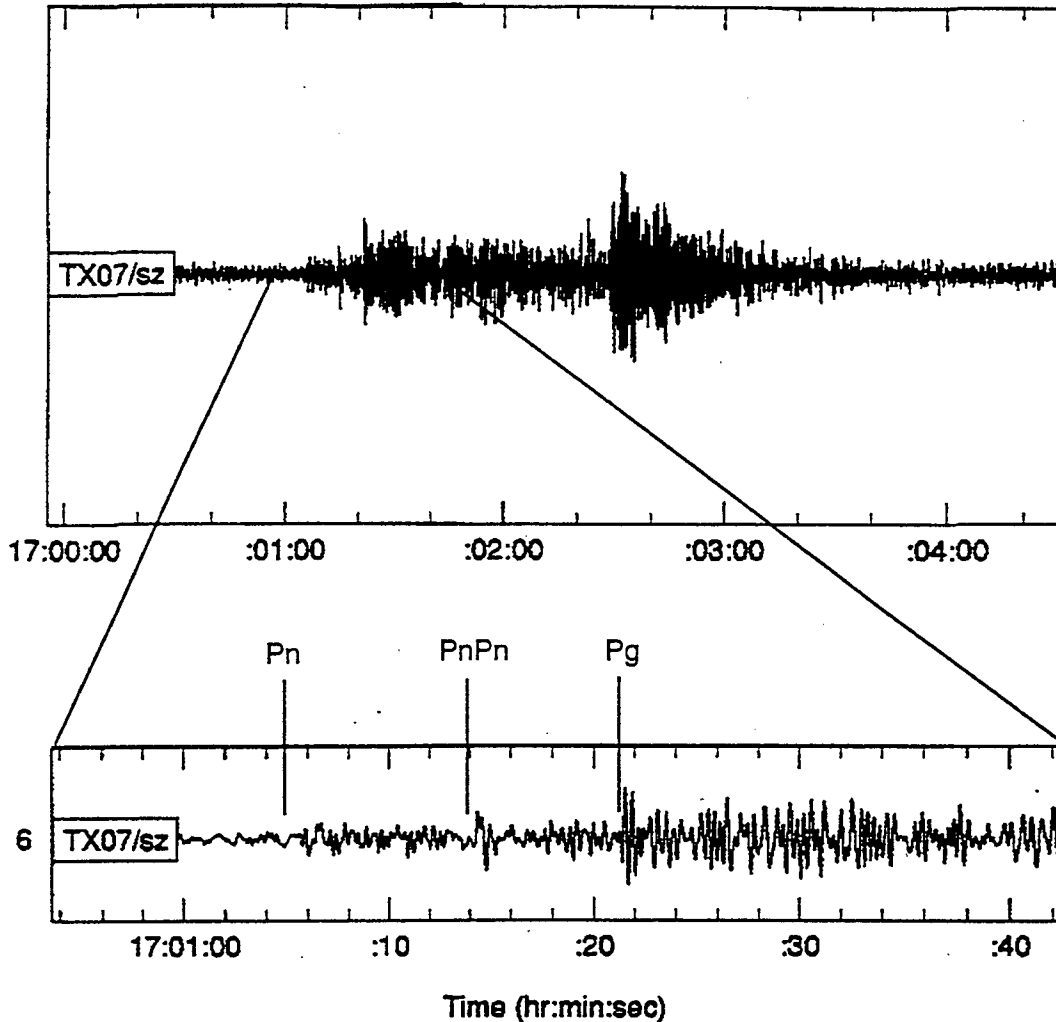
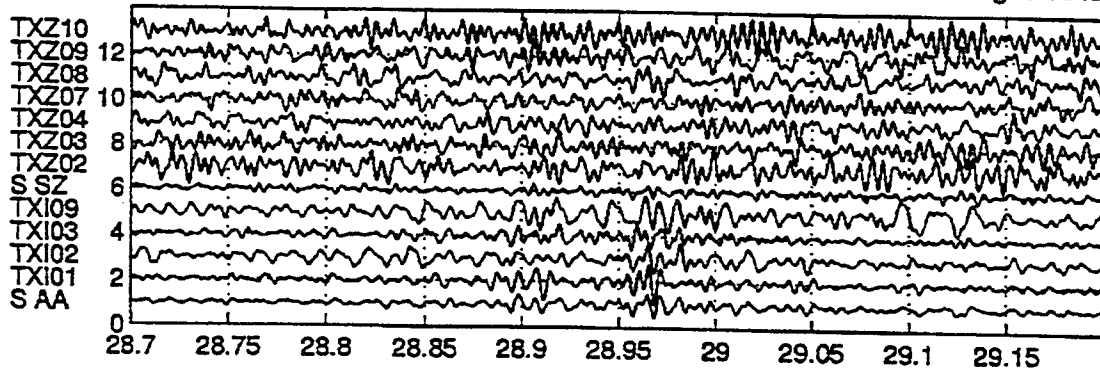


Figure 1-8. Vertical-component seismogram from a explosion (with no delays between rows or holes) at the Phelps-Dodge mine at Tyrone, New Mexico. The inset shows three distinct P wave arrivals. The second of these arrivals is thought to be the seldom observed phase, PnPn. This phase has not been observed on records from ripple-fired blasts originating at the Tyrone mine, suggesting that the PnPn arrival is obscured by the coda of Pn for these explosions. Arrival times for the phase are in agreement with those predicted by the IASPI model. These explosions are more likely to produce infrasound signals seen at regional distances than ripple-fired explosions from the same mine.

Tyrone AZ explosion 11 October 1996 546.0 km 0.75-5 Hz shifted: 325 deg 0.35 km/s



1.025 second semblance filtered signal Semblance power 3

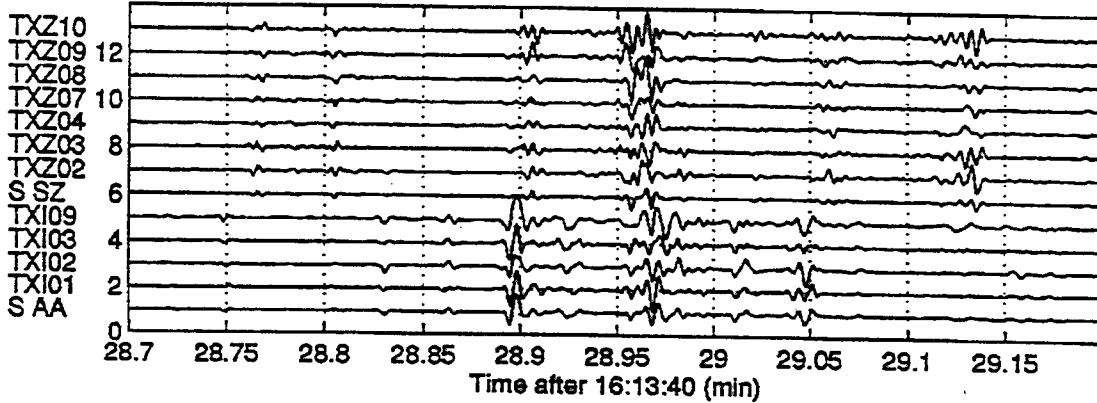


Figure 1-9. Results of semblance processing on seismo-acoustic data from the October 11, 1996 Tyrone explosion.

## 1.2 SHUTTLE QUAKE SUMMARY

The location of the TXAR array allows us to record the N waves produced as the space shuttle makes its landing approach to Kennedy Spaceflight Center. While the N waves recorded from the Shuttle are spectacular (~100 microbars), the unusual components of these signals were recorded on TXAR's seismic channels. Short-period seismic waves are seen prior to the N wave arrival that could easily be mistaken for surface explosions. Phases recognized in these signals include *Pg*, *Sg*, and *Rg*. FK processing of the phases showed appropriate phase velocities but different back-azimuths for each phase. We have termed these small seismic events "shuttle quakes", and the results of our initial study are presented in this section of the poster presentation.

STS82

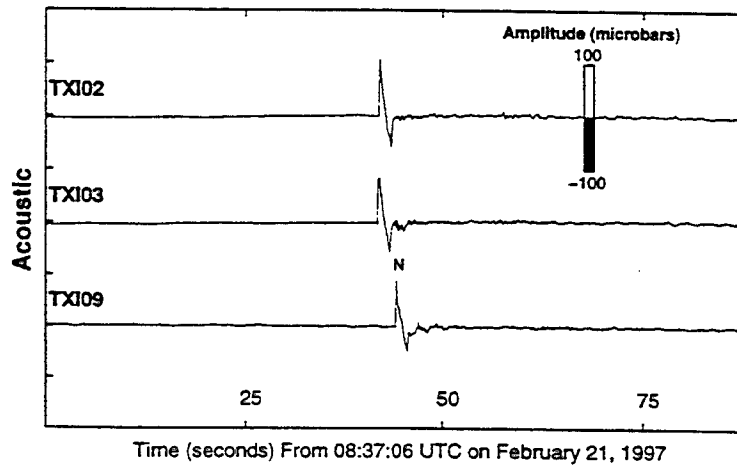
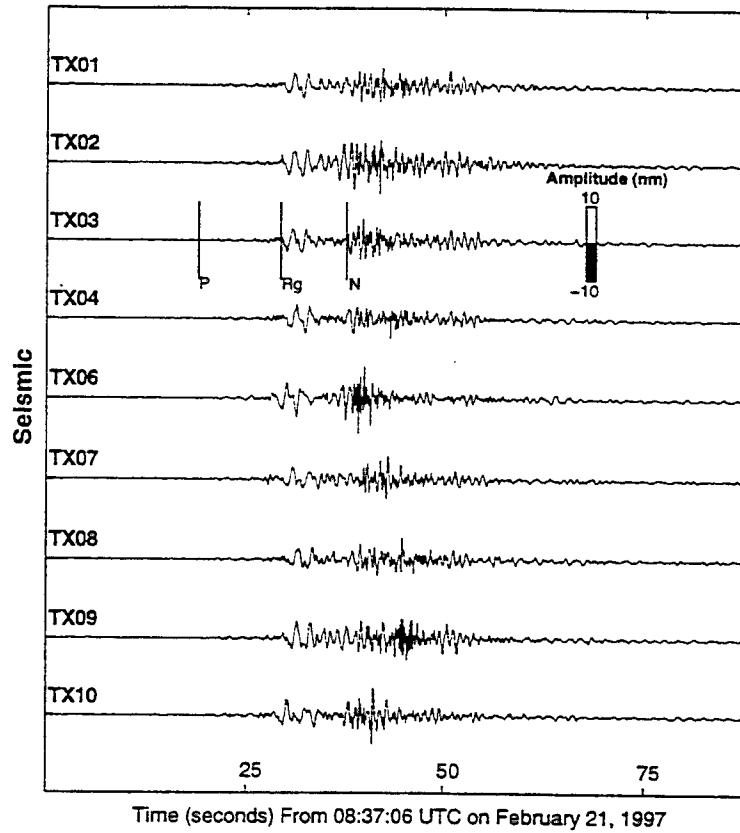
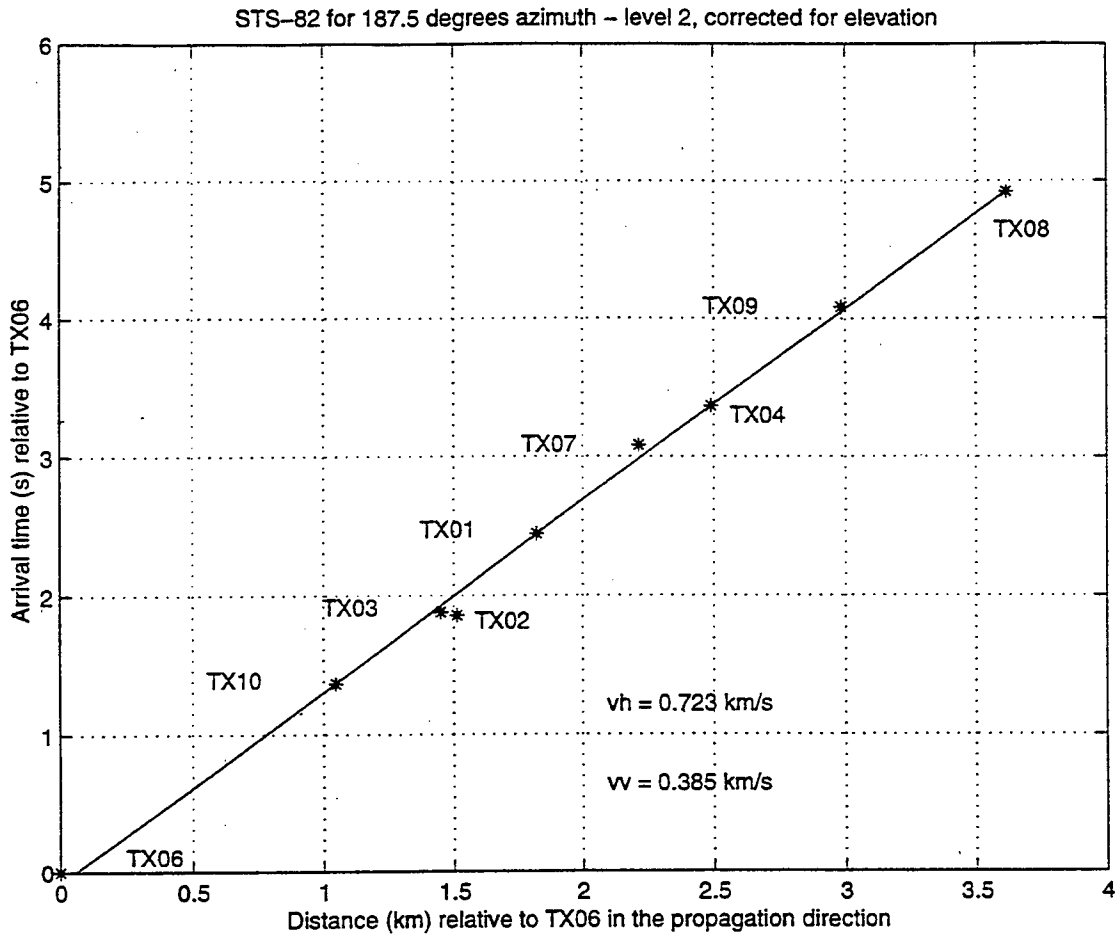


Figure 1-10. Seismograms and barograms from the STS-82 shuttle mission. Distinct phases include *Pg* and short-period Rayleigh (*Rg*). The infrasound sensors of the TXAR seismo-acoustic array recorded the supersonic pressure wave (*N* wave).



**Figure 1-11. Results of processing the N wave using wavelet decomposition. Horizontal phase velocity and back-azimuth were determined to be 0.72 km/s and 188.8, respectively. Frequency-wavenumber (F-K) analysis was used to determine the apparent phase velocities and back-azimuths for the seismic phases.**

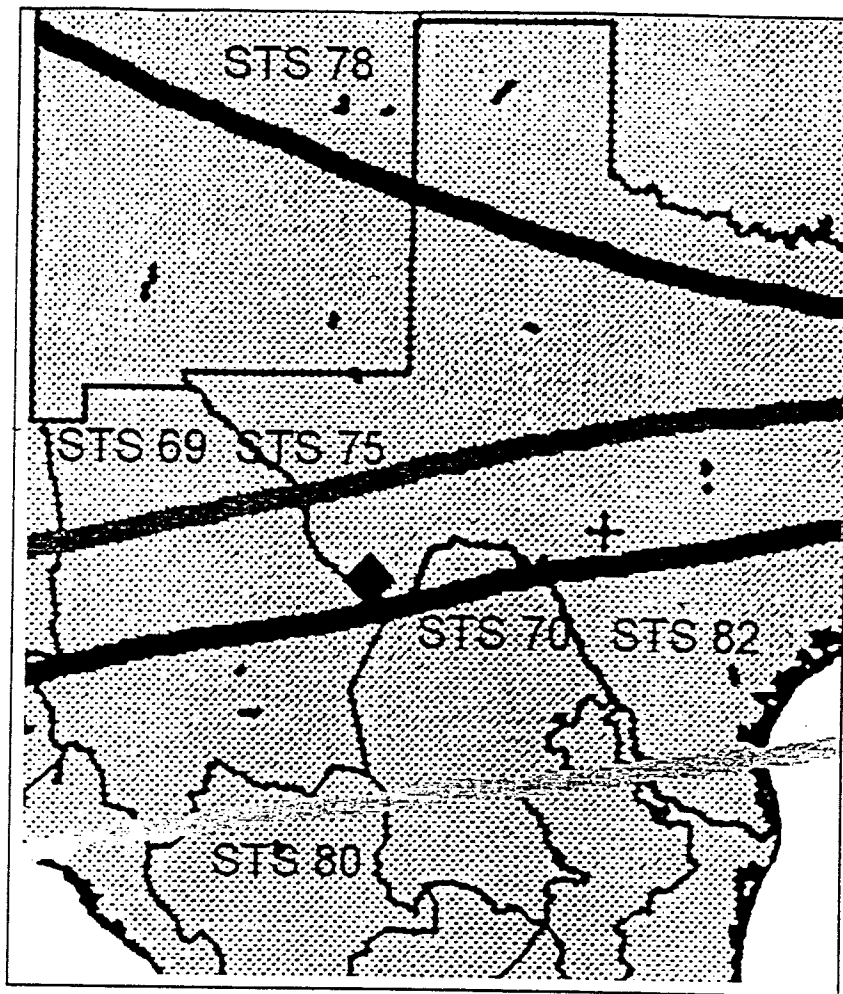
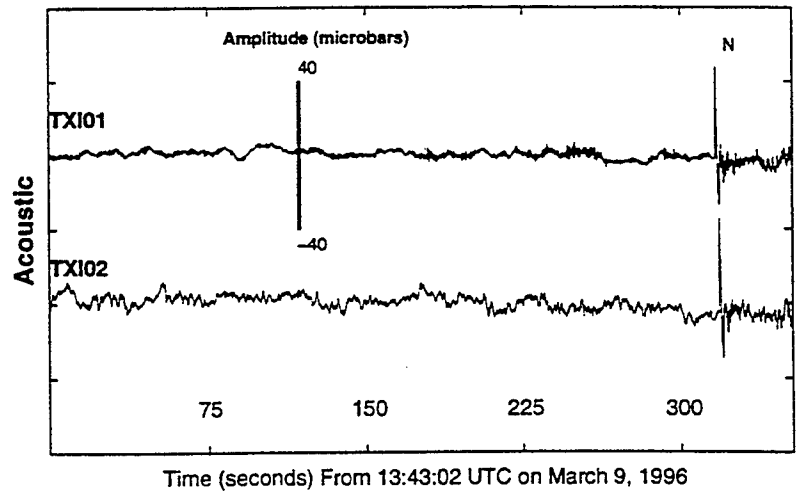
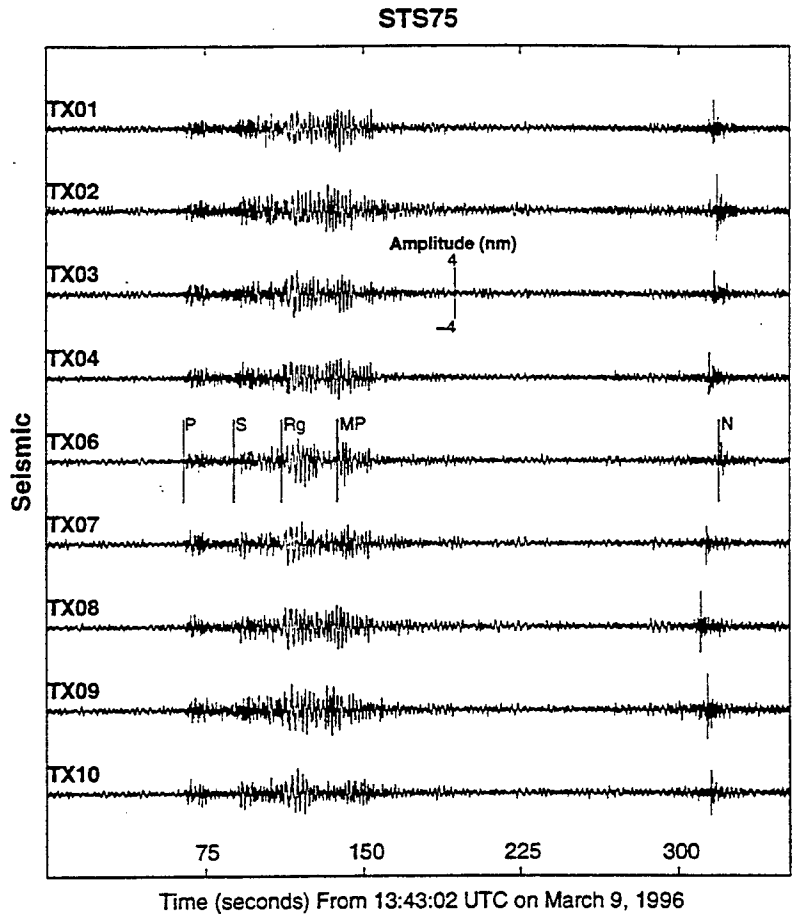
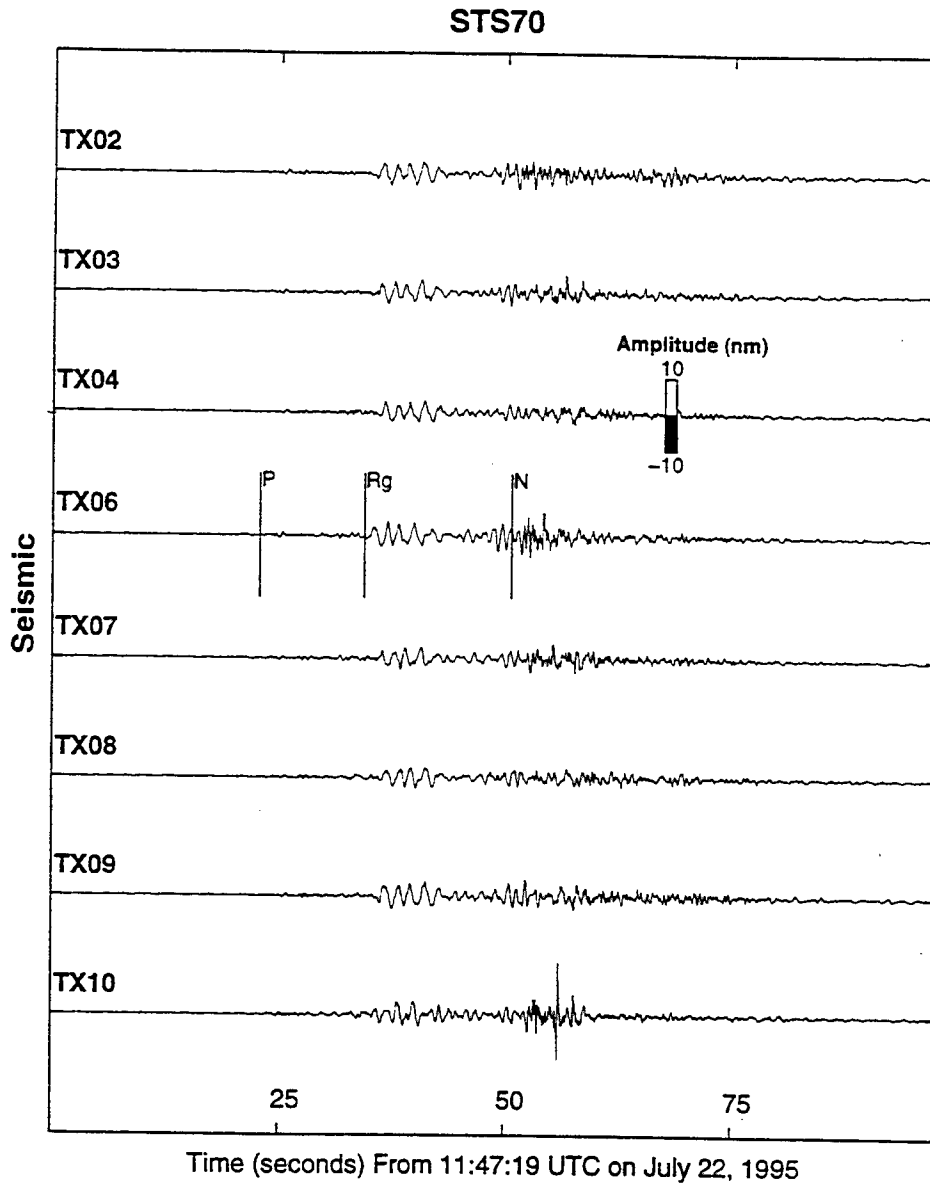


Figure 1-12. Landing groundtracks for several shuttle missions for which N waves, infrasound signals, and/or shuttle quakes were observed.



**Figure 1-13. Shuttle quake from the STS-75 mission which passed approximately 150 km north of the TXAR array.**



**Figure 1-14. Shuttle quake from the STS-70 mission which passed approximately 50 km south of the TXAR array.**

# STS69

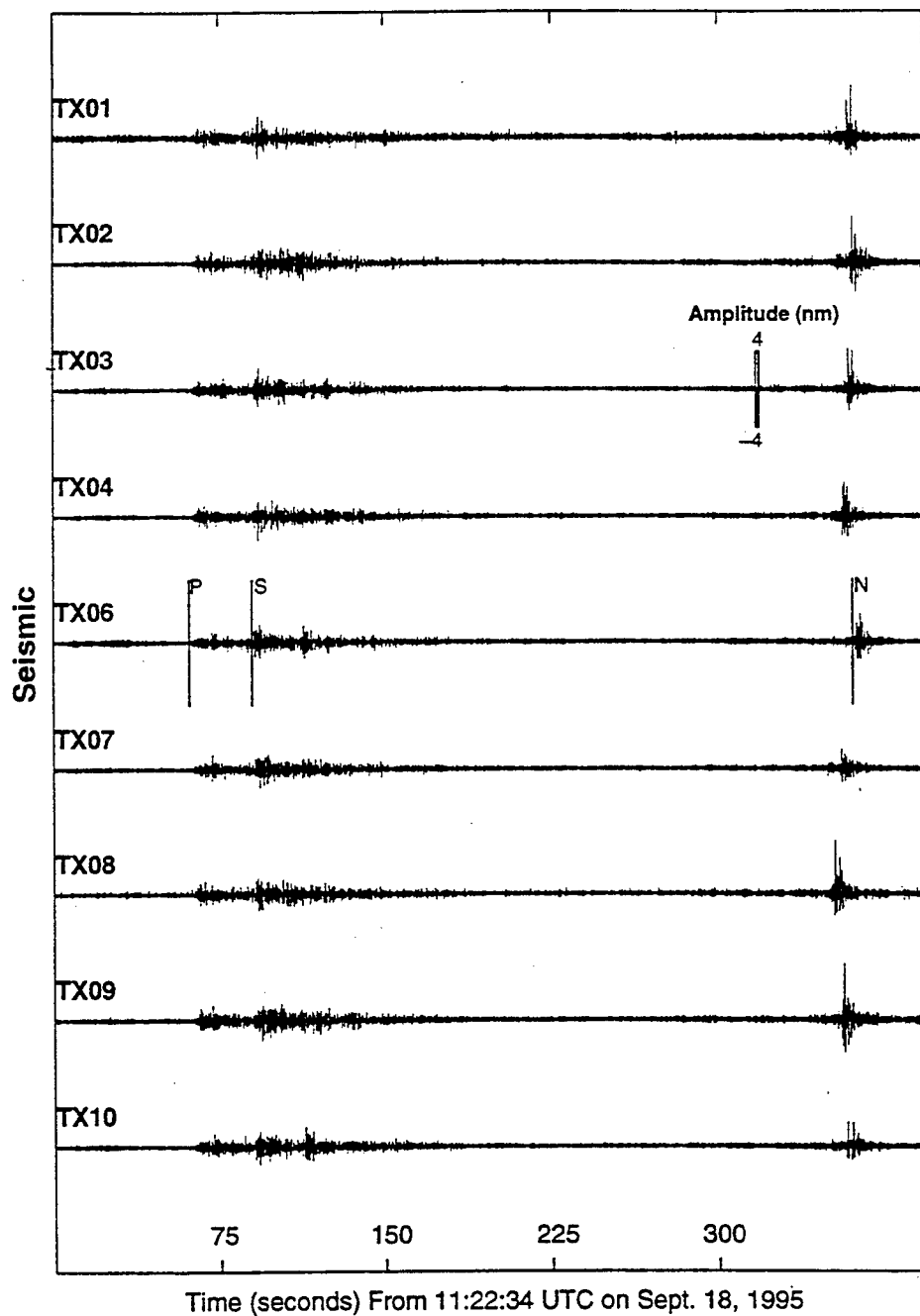
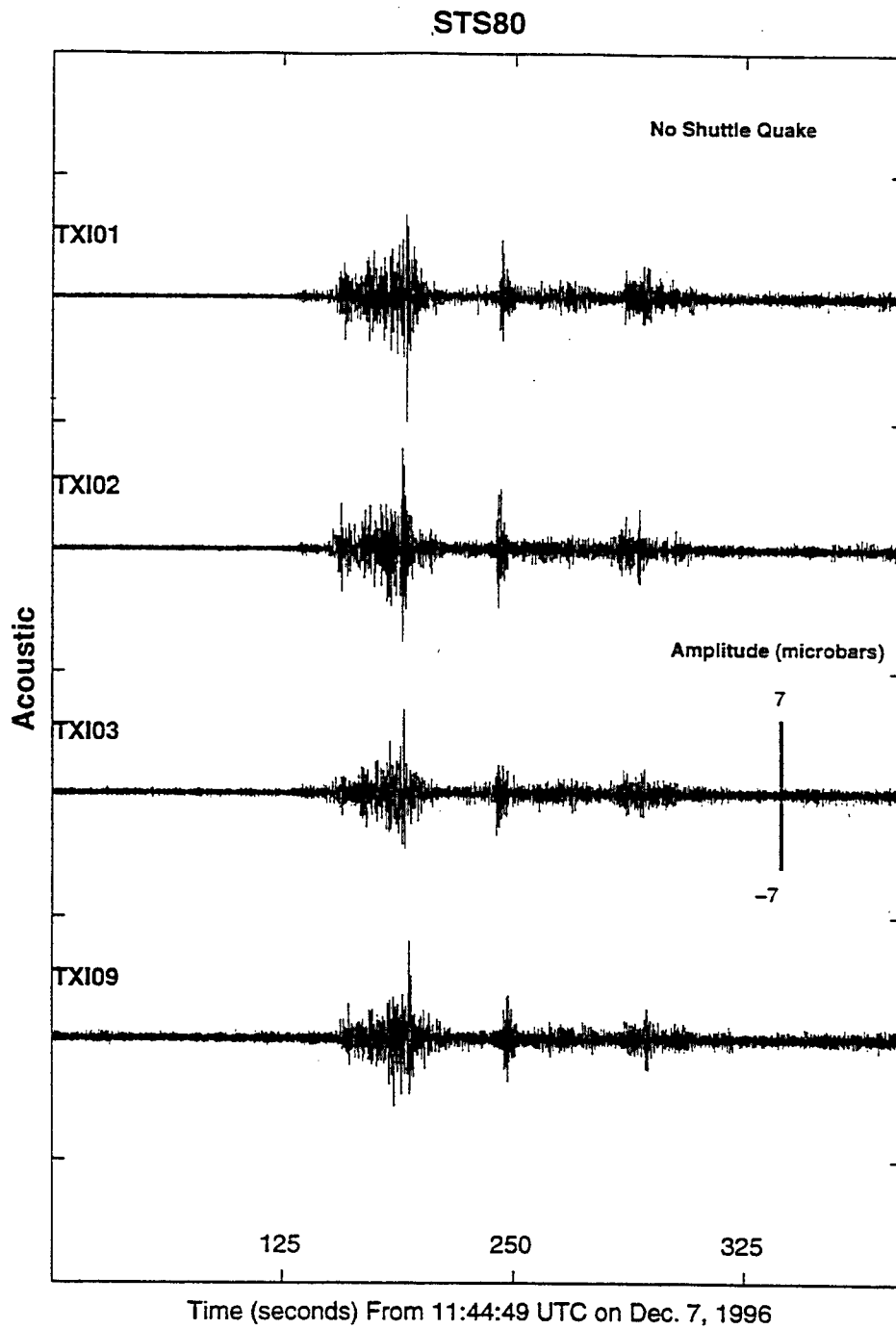


Figure 1-15. Shuttle quake and N wave from the STS-69 mission which passed approximately 150 km north of the TXAR array.



**Figure 1-16. Infrasonic from the STS-80 mission which passed far enough from TXAR that no N wave or shuttle quake was observed.**

# STS-82 SHUTTLE QUAKE

February 21, 1997 Landing Time: 8:32:26 UTC

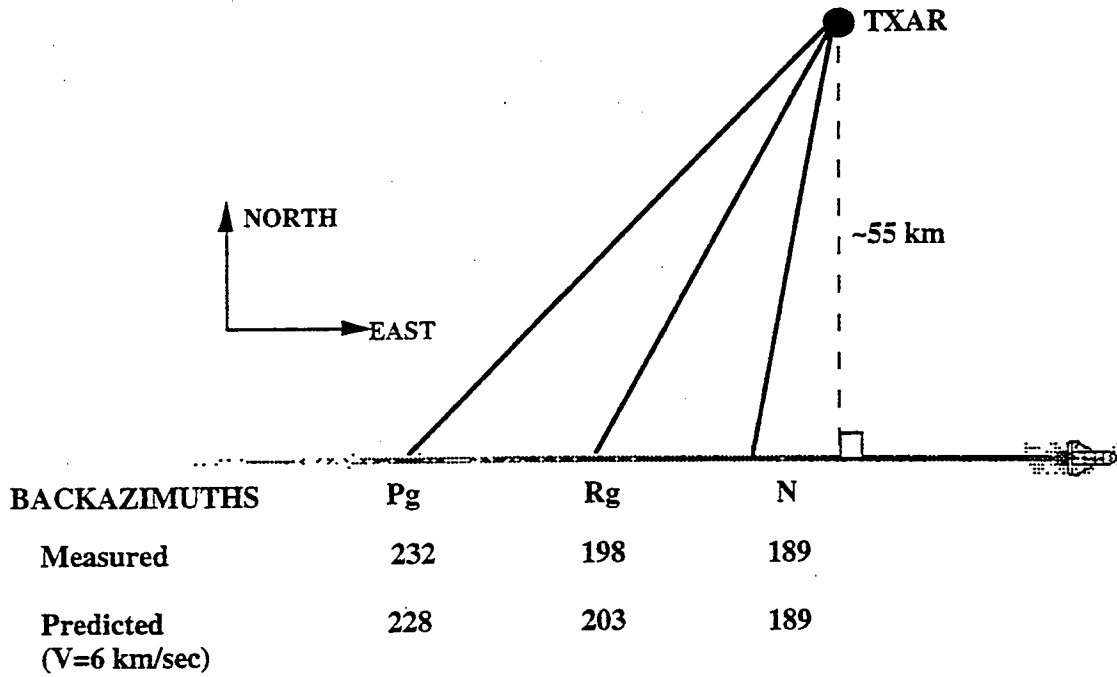


Figure 1-17. Initial results of the "Bow Wave" theory using phase velocity and back-azimuth data from STS-82. Results are promising, and additional shuttle quake data are now being used to further test the theory.

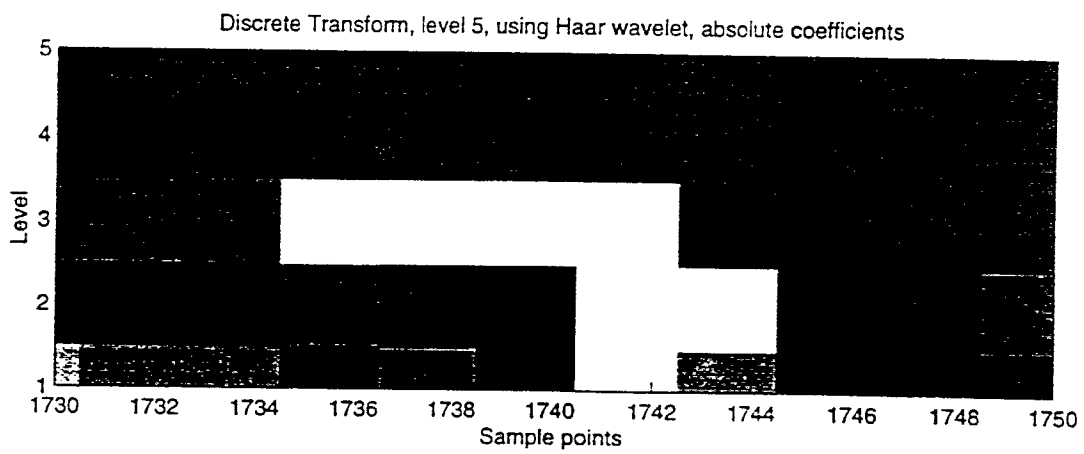
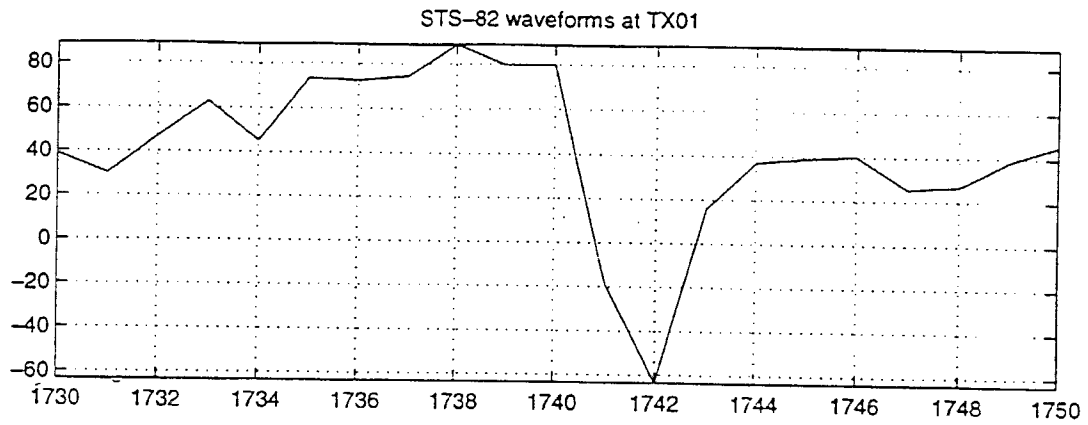
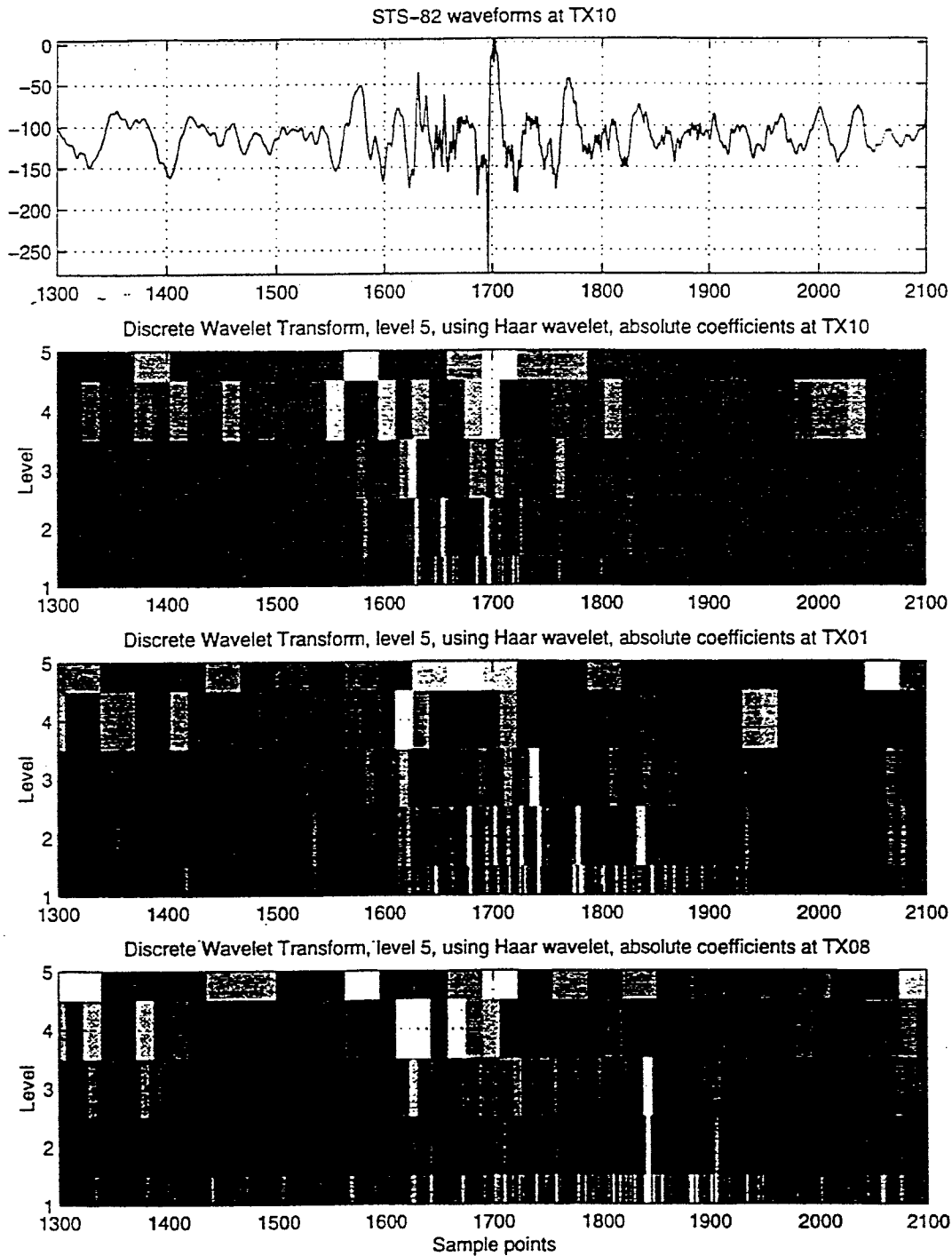


Figure 1-18. Wavelet transform of the N wave from STS-82. The arrival of the N wave on the seismic channels is seen as a sharp impulse on Levels 1-4 of the transform.



**Figure 1-19. Wavelet decomposition of the N wave at TX01. The arrival time for the phase is established to better than one sample point.**

### 1.3 BOLIDE SUMMARY

The Geminid meteor shower is active between December 6 and December 19, reaching peak activity on December 13. Unlike most meteor showers which are by-products of comets, the Geminid orbit does not match any known orbit for a comet. However, the Geminid orbit does match the Earth-crossing asteroid 3200 Phaethon, a four-mile wide object discovered in 1983. Thus the Geminids are the first meteor shower to be positively linked to asteroids. Rates during the peak observation time are 80 per hour. SMU personnel at TXAR between December 9 and December 13 reported sighting many meteors. On December 12, 1996, we recorded over 120 acoustic arrivals from the northwest of TXAR. Based upon the location of the radiant of the Geminids, we believe these signals were the result of the meteors entering the upper atmosphere. This final section of the poster presentation looks at suspected bolide signals at TXAR.

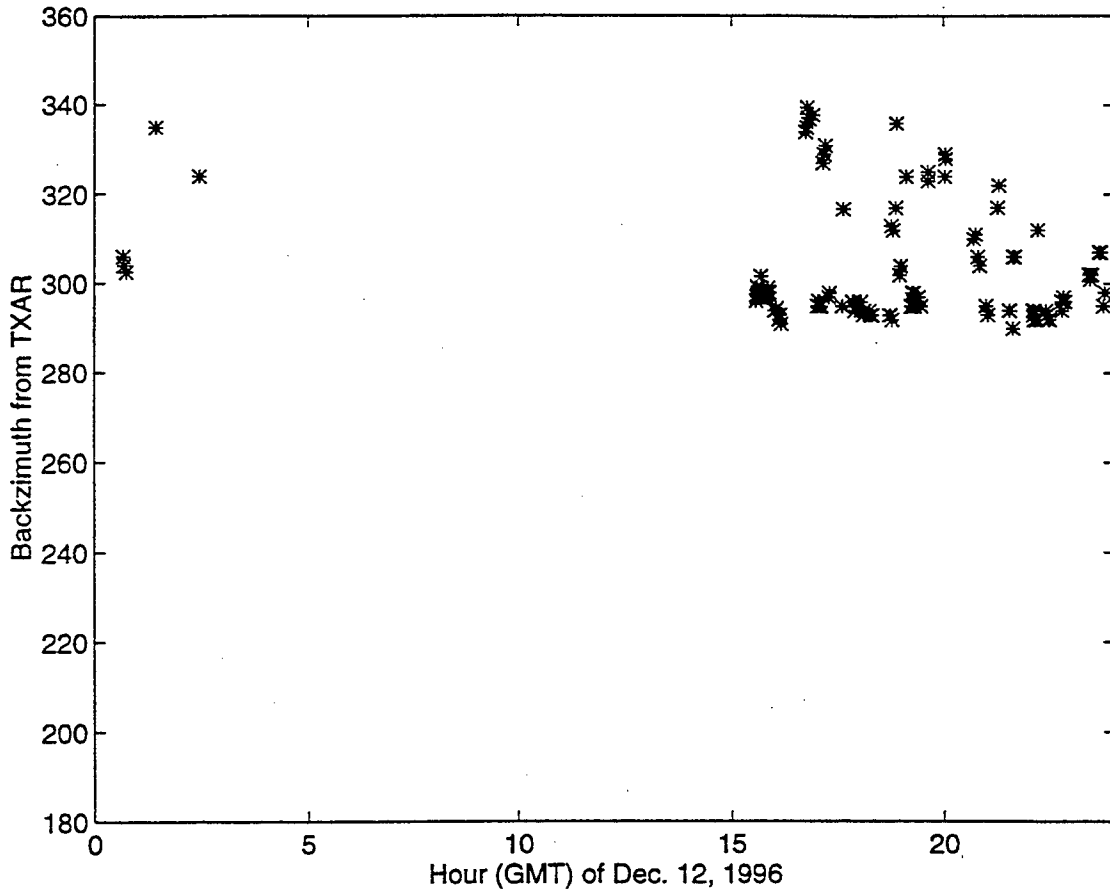


**Figure 1-20.** Arrival times for 127 infrasound signals recorded at TXAR on December 12, 1996 plotted against back-azimuth. These signals are suspected to be from meteors of the Geminid shower entering and causing acoustic disturbances in the upper atmosphere northwest of TXAR (290-340 degrees). The maximum amplitude of this signal is approximately 40 mbars, one of the largest infrasound events recorded at TXAR. The gap in the data between 2:00 and 14:00 GMT could be related to the zonal wind effect discussed earlier. Half of the day's events should be in the atmosphere northeast of TXAR, and thus would be attenuated by strong winds in the upper atmosphere.

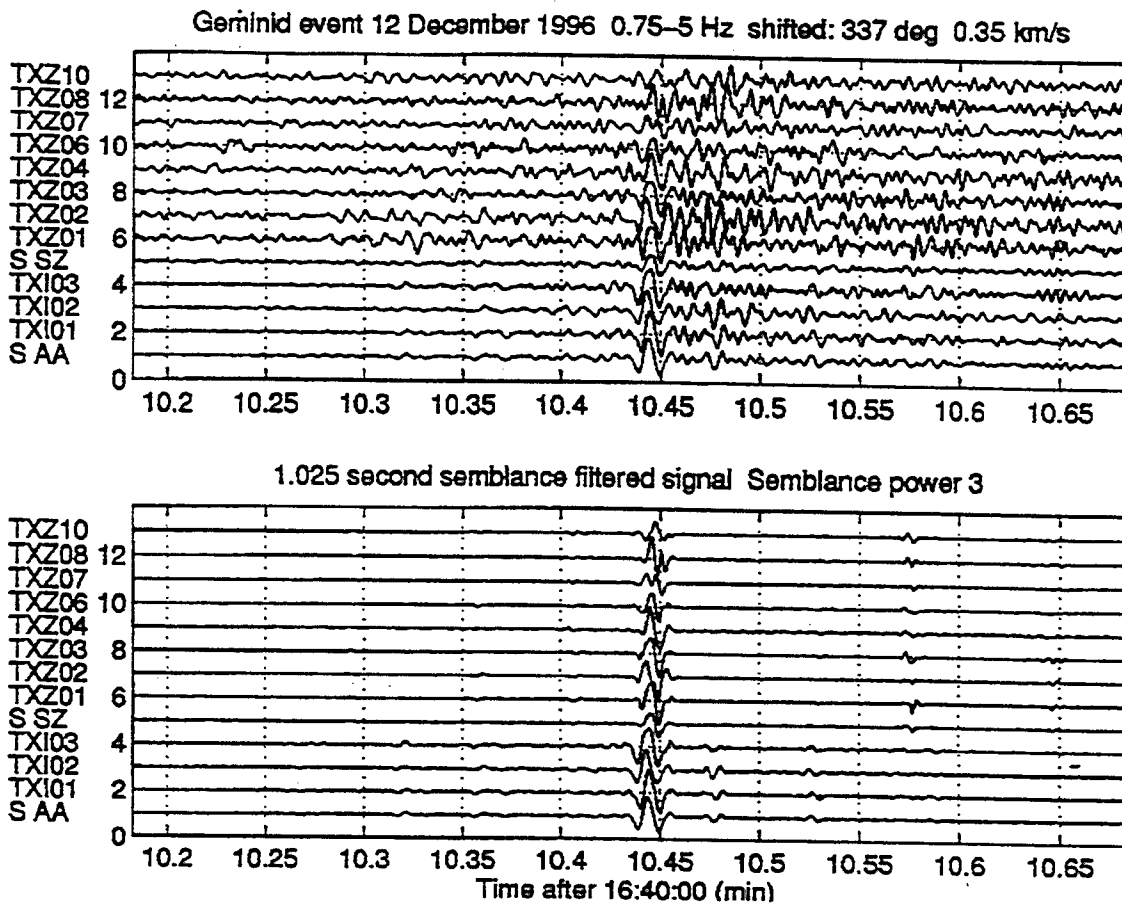


Figure 1-21. Semblance between traces for a Geminid acoustic event on December 12, 1996.

## APPENDIX 2. OBSERVATIONS OF SHUTTLE QUAKES AT TXAR

Jessie L. Bonner  
Eugene T. Herrin  
Gordon G. Sorrells  
Jack G. Swanson  
Ileana M. Tibuleac

### Introduction

People in the remote ghost town of Terlingua, Texas, were awakened early on February 21, 1997 by a "large explosion". SMU Geophysics operates a ten-element seismic and four-element acoustic array in this area and was contacted by a concerned citizen and asked to help identify the cause of the large acoustic event. After looking at the classic "N wave" on the acoustic channels, we concluded the residents had heard a sonic boom. The name "N wave" comes from the characteristic sharp pressure increase followed by a linear decrease in pressure until ambient pressure is restored by a sharp pressure rise (see Figure 1). After checking the NASA web-pages, we knew the sonic boom was produced from the space shuttle, which had landed at Kennedy Space Center some 15 minutes after the explosion had been heard. By looking at the landing groundtrack, we concluded that shuttle missions STS-82 had passed less than 55 km south of the TXAR array on its landing approach to the Kennedy Spaceflight Center.

While the N waves from STS-82 were spectacular (~100 microbars), the truly remarkable parts of these signals were recorded on the seismic channels of the TXAR array. By looking at Figure 1, one might conclude that the sonic wave arrived and was recorded at TXAR during another seismic event. The presence of short-period, fundamental mode Rayleigh waves,  $R_g$ , in this seismic signal suggests a very shallow source. However, initial FK processing of the  $P_g$  and  $R_g$  waves showed appropriate phase velocities but different back-azimuths (Table I) for each phase.

Gordon Sorrells and Eugene Herrin then proposed that these seismic signals were "bow waves" created as the supersonic N wave sweeps across the surface of the earth. Thus, work started on the theory, and results produced thus far have been promising. Predicted back-azimuths for different phases ( $P_g$  and  $R_g$ ) are within  $5^\circ$  of the true back-azimuths. We have termed these small seismic events created by the passage of the shuttle as "shuttle quakes".

This paper represents a compilation of the data recorded thus far at TXAR from passage of different shuttle missions. Appendix 3 shows work completed on the theory. So far, seven different shuttle missions have had landing groundtracks close enough to TXAR for recording of both shuttle quakes and N waves, or infrasound signals. For each mission, we show plots of the data as well as tables showing parameters for each mission (Figs. 1-18 and Tables I-IX). These observations will be combined with the "bow quake" theory, as well as the wavelet analysis results, and submitted to Seismological Research Letters within the upcoming months.

## Processing Seismo-Acoustic Data

Horizontal phase velocities and back-azimuths for each of the phases identified on the "shuttle quakes" were determined by frequency-wavenumber (F-K) analysis. This technique transforms the array data from a time-space domain into a frequency-wavenumber domain. We applied a 2-second window around each phase (*P*, *S*, and *R<sub>g</sub>* arrivals) and used the F-K technique to determine back-azimuth and phase velocity. For body wave arrivals, the data was filtered with a 3<sup>rd</sup> order bandpass filter between 0.6 and 4.5 Hz to optimize results. For surface waves, this was modified to a 3<sup>rd</sup> order bandpass filter between 0.1 and 2 Hz. Results from previous studies that used regional seismic events have shown the F-K technique to be very reliable at TXAR with standard deviations of approximately  $\pm 0.2$  km/sec and  $\pm 5$  degrees for phase velocity and back-azimuth, respectively. The results of the F-K processing are shown in Tables I, II, III, V, and VI. Notice how the back-azimuths change from phase to phase. The same technique was used to determine back-azimuth for the infrasound arrivals from STS-78 and STS-80 (Table VIII and IX), both missions being at great distances from TXAR.

A different technique was used to determine the back-azimuth and phase velocity for the supersonic "N waves". Since the TXAR infrasound array has only been in operation since March 1996, we could not determine azimuths for the N waves using the infrasound channels for missions prior to STS-78. Instead, we chose to use the seismic response to the N wave as recorded on the vertical-component seismometers. The seismic response is dominated by two pressure increases at the beginning and end of the boom which produce downward spikes on the seismograms. However, determining where these pressure increases began proved problematic as the "shuttle quakes" masked the N wave arrival for missions STS-82 and STS-70.

Thus, we decided to use wavelet analysis for the problem. The Haar wavelet, which is discontinuous and resembles a step function, was considered optimal for detection of sharp discontinuities in a signal otherwise masked by the simultaneous seismic arrivals. The arrival times of the N waves on the seismic channels were then obtained with a precision of a sample point by discrete wavelet decomposition, and then used to calculate the horizontal phase velocity and back-azimuth. With one exception, see Table IV, the second level of detail in the wavelet decomposition for each N wave was used to manually find the arrival times at each station in the TXAR array. Since a N wave has a spectral response at all frequencies, the distribution of energy in all the other levels were considered as well. Well defined N waves from events to the south of TXAR (STS-70 and STS-82) worked best in the decomposition routine. N-waves from shuttle passages North of TXAR (STS-69, STS-78, and STS-92) were less defined, but because of refraction and reflection of infrasound in the atmosphere, more than one arrival was processed (see Tables IV and VII).

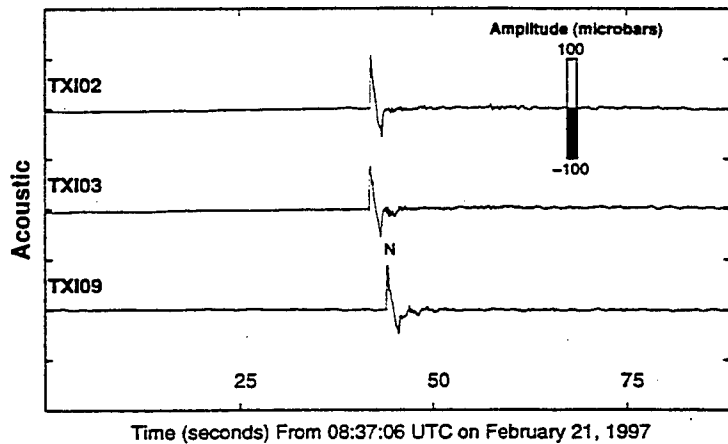
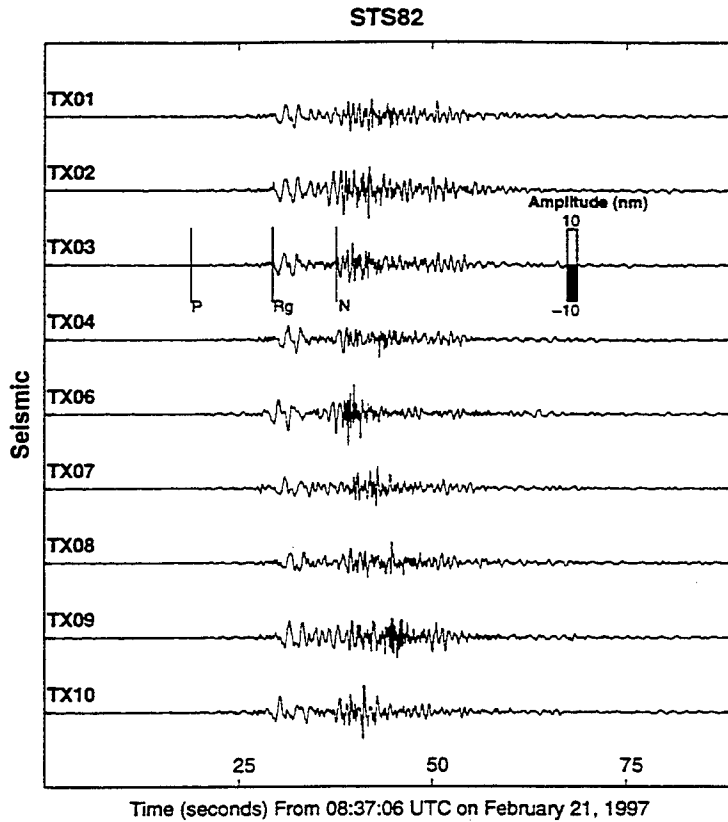


**Figure 2-1. Seismograms and barograms from the STS-82 shuttle mission. Distinct phases include  $P_g$  and short-period Rayleigh ( $R_g$ ) recorded on the vertical component of the seismometers of the TXAR array. The infrasound sensors of the TXAR seismo-acoustic array recorded the classic “N wave” from the passage of the supersonic pressure wave. This wave coupled into the ground and can be seen as a packet of different frequencies on the seismic channels (labeled as N on the upper plot).**

## STS-82 PARAMETERS

Shuttle: Discovery  
 Mission Dates: February 11-21, 1997  
 Landing: KSC at 08:32:26 UTC  
 Mission: Repair mission II for the Hubble space telescope  
 Landing Groundtrack: Approximately 55 km south of TXAR bearing 80°



Times do not correspond to STS-82 landing.

Phase	Arrival Time <sup>1</sup>	Back-azimuth	Velocity	Quality <sup>2</sup>
	08:17:55.6	252.3	6.1	
	08:18:04.25	21.9	2.5	
Ground-coupled Rayleigh	08:18:11.93	158.2	2.2	1
	08:18:15.38	157.5	0.723	

Table I. Mission information and results of processing seismic and acoustic signals from STS-82.

<sup>1</sup> Measured at station TX06

<sup>2</sup> Based upon convergence of FK results to a stable solution.

<sup>3</sup> Short-period Rayleigh waves caused by coupling of the N wave into the near-surface. Since this phase has a velocity greater than the N wave, the phase runs out in front of the N wave. However, determining the back-azimuth and phase velocity is problematic due to the lack of coherence in the phase across the array.

<sup>4</sup> Obtained using a wavelet 2 decomposition of the seismo-acoustic channels.

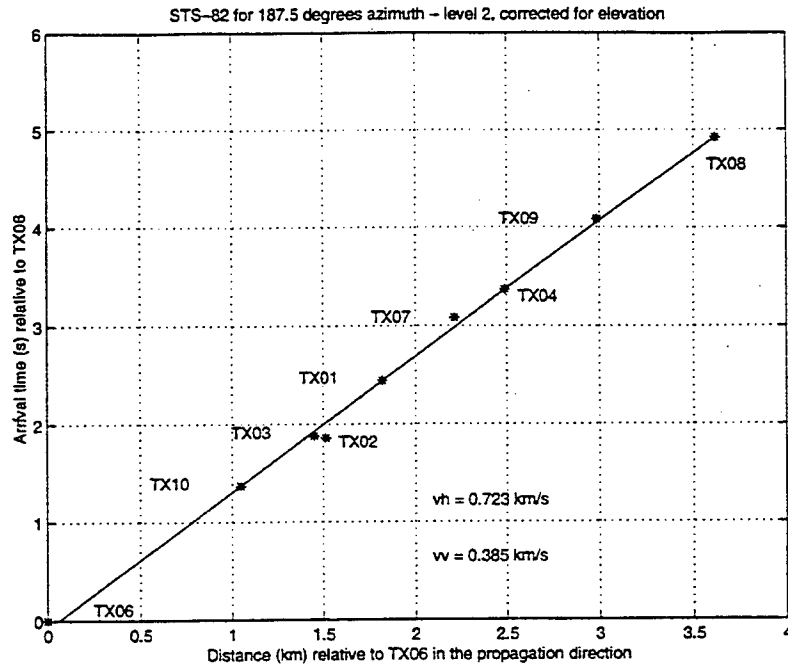


Figure 2-2. Results of processing the "N wave" for STS-82 using wavelet decomposition. These results are corrected for elevation differences of the stations at TXAR.

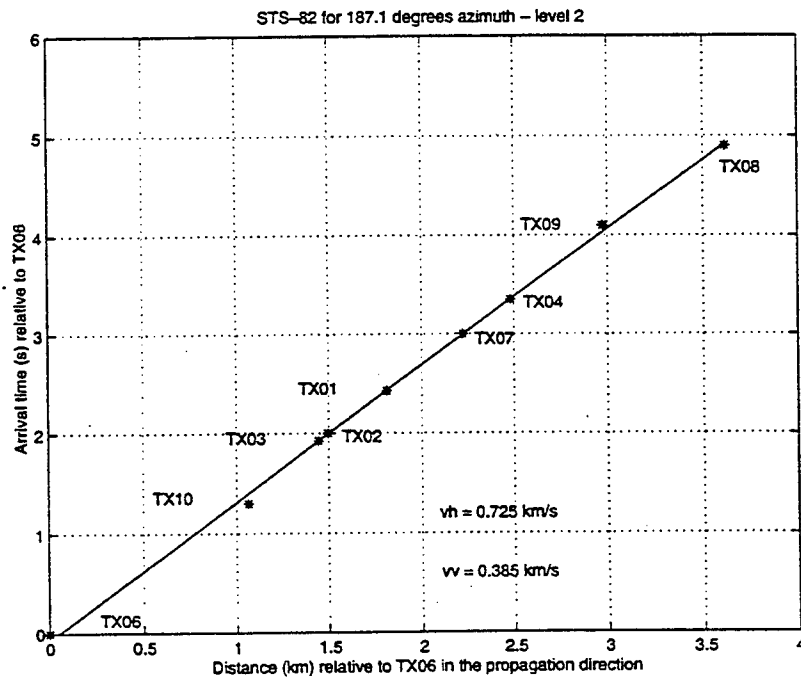
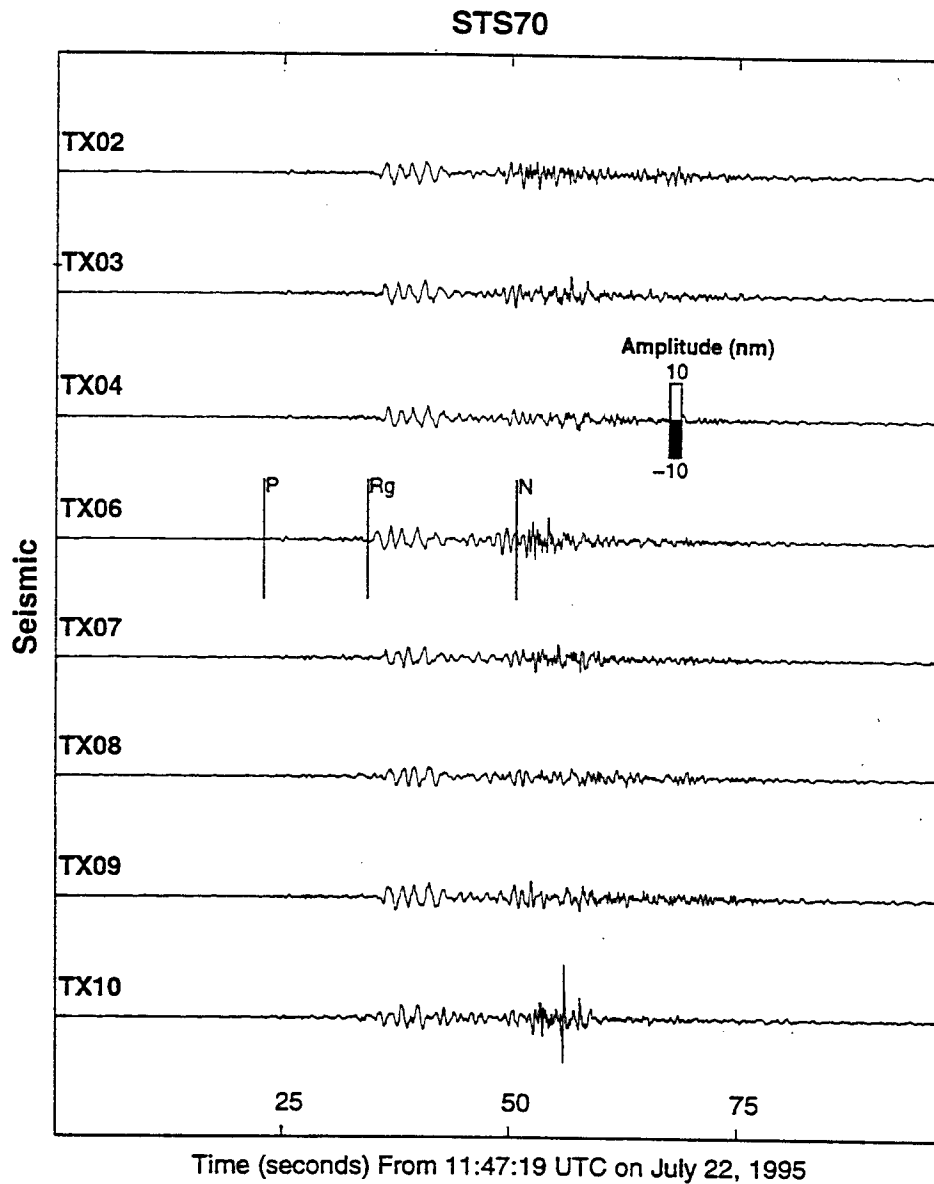


Figure 3-3. Results of processing the "N wave" for STS-82 using wavelet decomposition. These results are not corrected for elevation differences of the stations at TXAR.



**Figure 2-4.** Seismograms produced from the shuttle mission STS-70. We checked our archived array data for other shuttle events, and found seven separate missions which created either seismic or infrasound that was recorded at TXAR. STS-70 had a similar groundtrack to STS-82, thus back-azimuths and phase velocities (Table II) were similar. In fact, spectral comparisons show how similar the *Pg* and *Rg* signals are for STS-82 and STS-70 (Figs. 7-8).

## STS-70 PARAMETERS

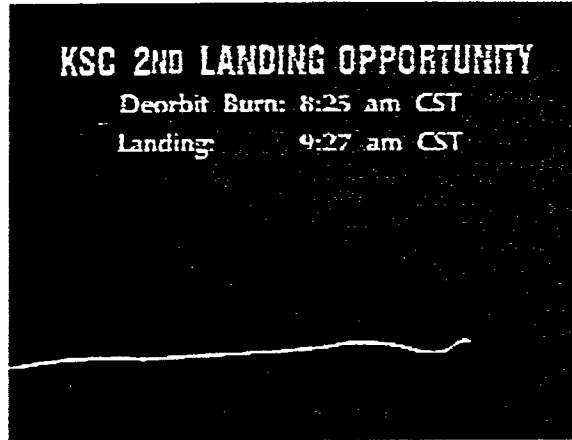
Shuttle: Discovery

Mission Dates: July 13-22, 1995

Landing: KSC at 12:02:11 UTC

Mission: Deployment of the 7<sup>th</sup> Tracking Data and Relay satellite

Landing Groundtrack: Approximately 55 km south of TXAR bearing 80°



Times do not correspond to STS-70 landing.

Phase	Arrival Time <sup>5</sup>	Back-azimuth	Velocity	Quality <sup>6</sup>
<i>P<sub>g</sub></i>	11:47:40.73	162.21	6.3	
<i>P<sub>2</sub></i>	11:47:53.18	166.2	2.5	
ground coupled	11:48:06.43	162.7	2.4	3
Rayleigh	11:48:11.2	165	0.621	

Table II. Mission information and results of processing seismic and acoustic signals from STS-70.

<sup>5</sup> Measured at station TX06

<sup>6</sup> Based upon FK convergence to a stable solution

<sup>7</sup> No acoustic channels, thus measurements obtained using seismo-acoustics and a level 2 wavelet decomposition.

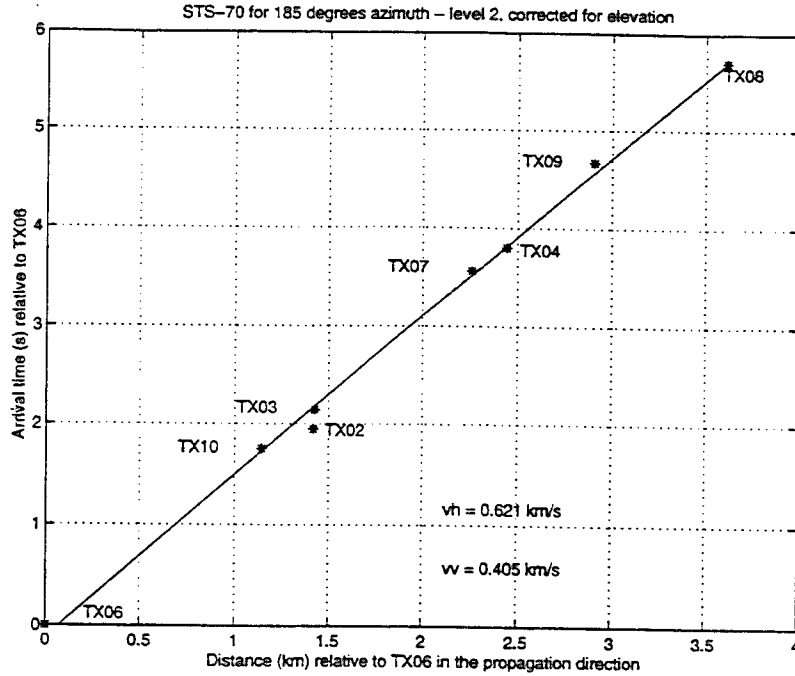


Figure 2-5. Results of processing the “N wave” for STS-70 using wavelet decomposition. These results are corrected for elevation differences of the stations at TXAR.

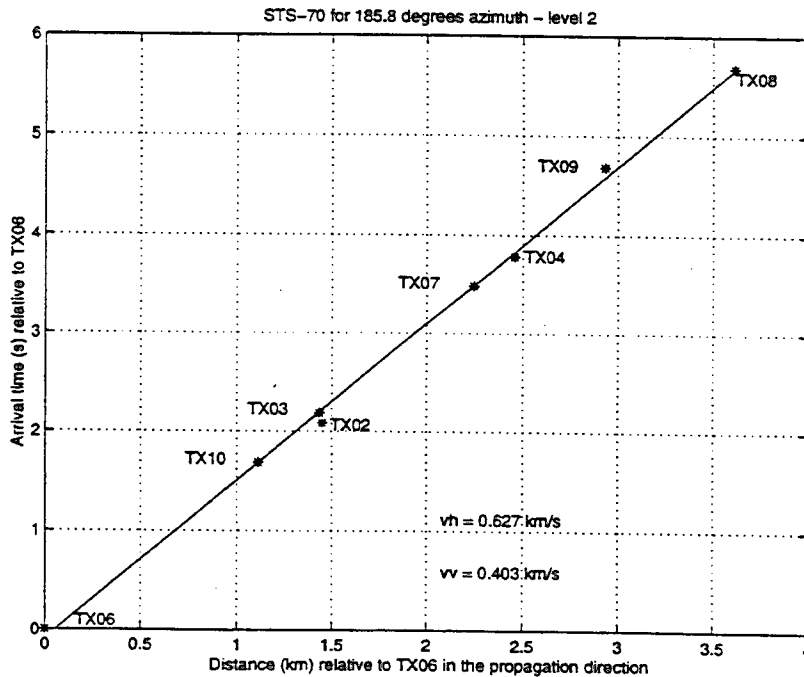
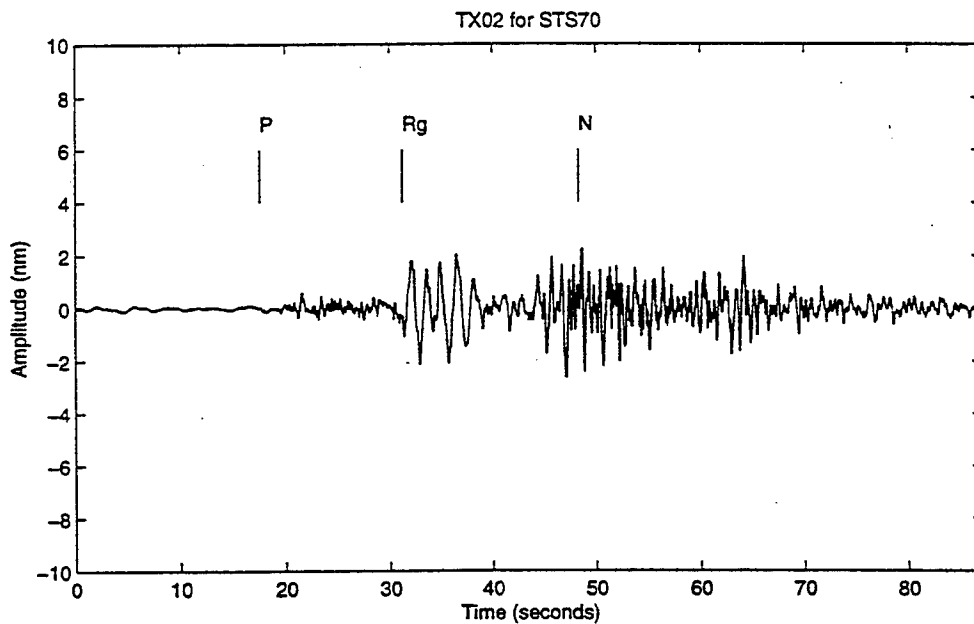
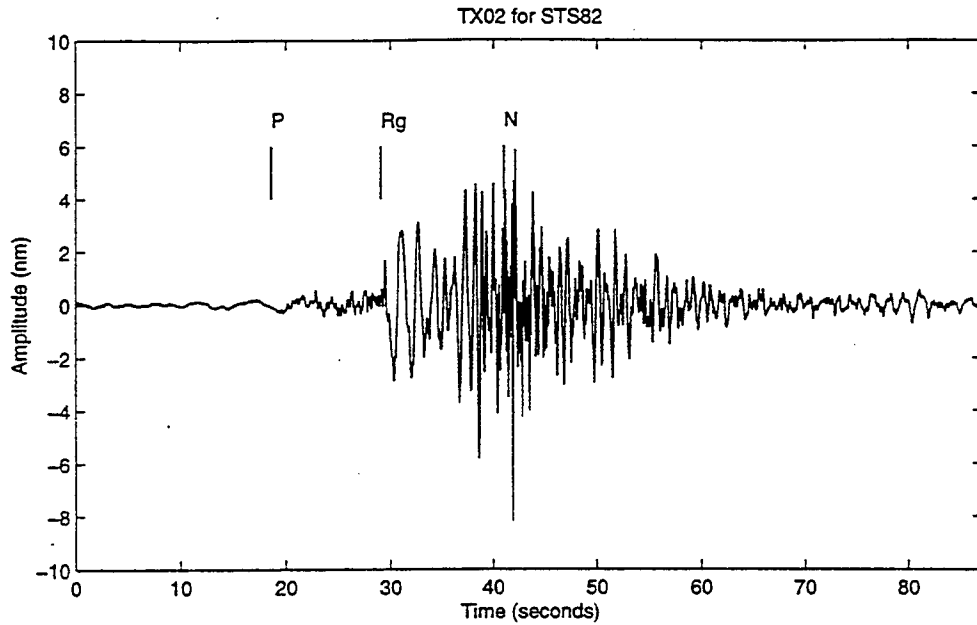


Figure 2-6. Results of processing the “N wave” for STS-70 using wavelet decomposition. These results are not corrected for elevation differences of the stations at TXAR.



**Figure 2-7. TX02 seismograms from the STS-82 and STS-70 missions show how similar the two shuttle quakes are. The increased separation in the phases in the lower plot suggests that STS-70 flew further south of TXAR than STS-82.**

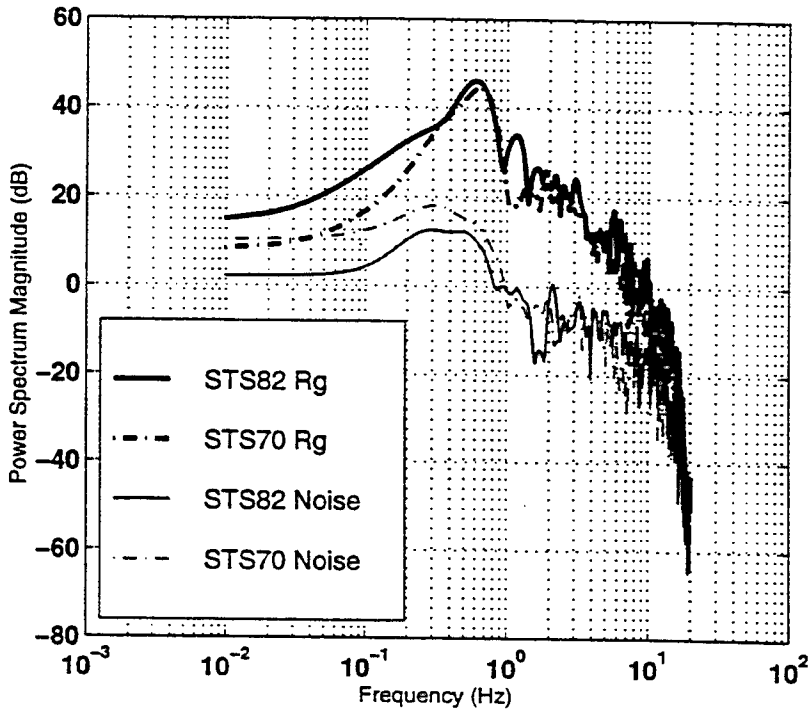
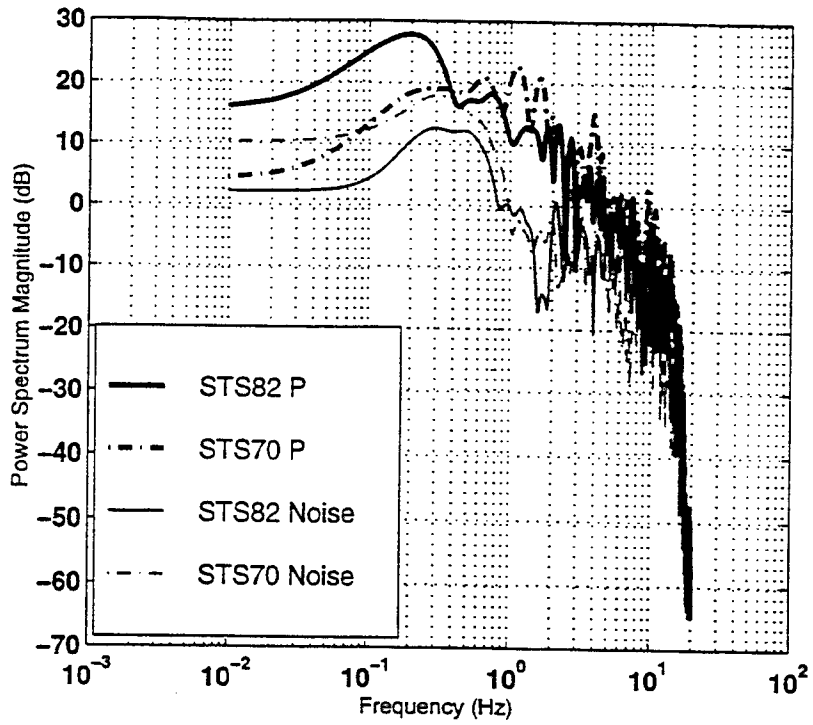


Figure 2-8.  $P_g$  and  $R_g$  spectra for STS-82 and STS-70.

STS69

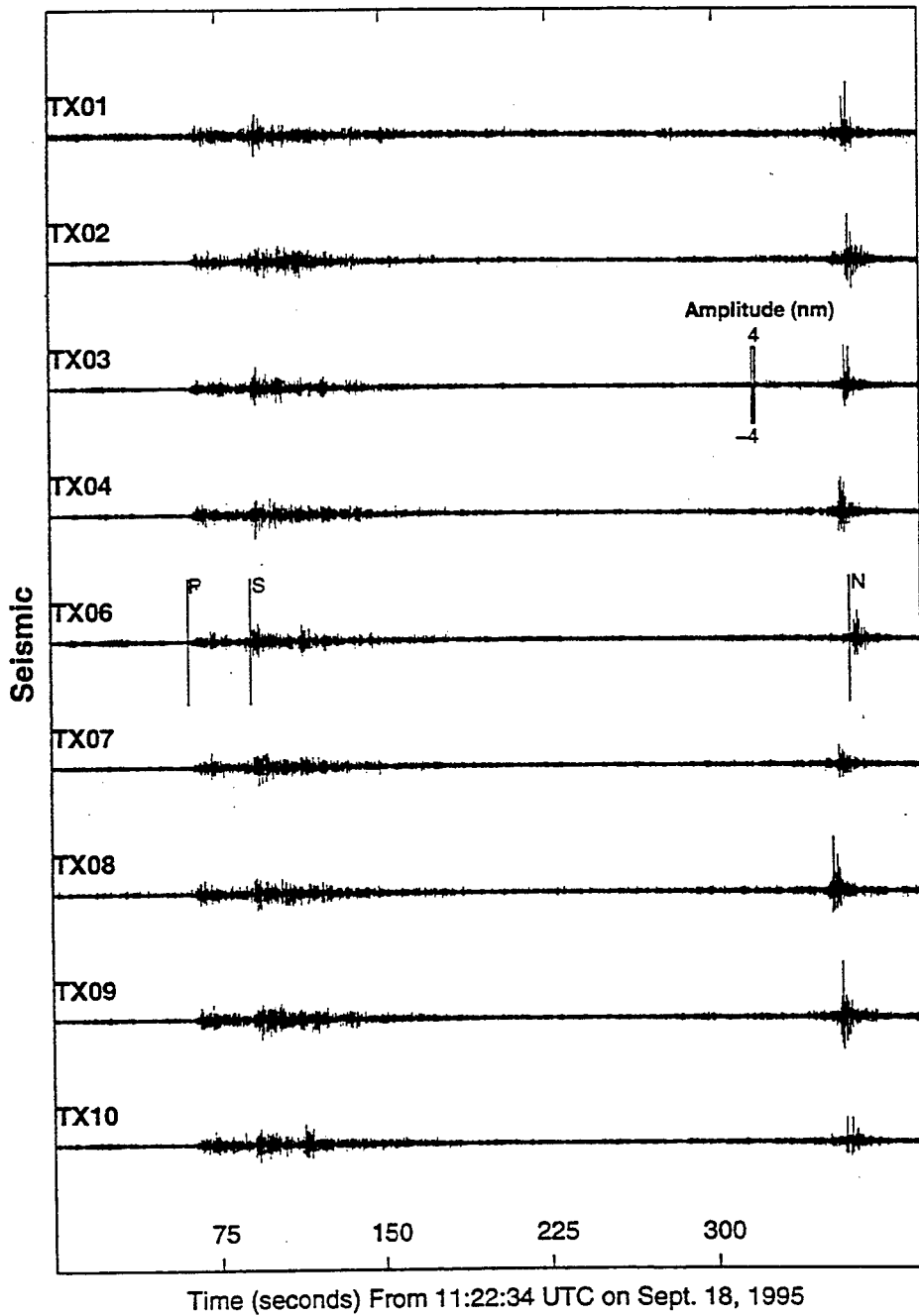


Figure 2-9. Shuttle quake from the STS-69 mission which passed approximately 150 km north of the TXAR array.

## STS-69 PARAMETERS

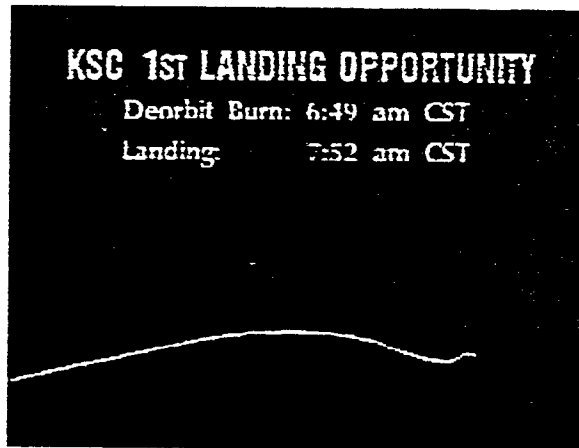
Shuttle: Endeavor

Mission Dates: September 7-18, 1995

Landing: KSC at 11:37:56 UTC

Mission: Experiments with the Wake Shield Facility and deployment of the Spartan 201 astronomy satellite

Landing Groundtrack: Approximately 150 km north of TXAR bearing 95°



Times do not correspond to STS-69 landing.

Phase	Arrival Time <sup>8</sup>	Back-Azimuth	Velocity	Quality
P	11:23:35.35	291.24	7.5	
P	11:23:45.53	354.57	8.5	B
S	11:24:05.03	322.21	3.8	B
482	11:24:25.85	338.88	2.1	B

Table III. Mission information and results of processing seismic signals from STS-69.

<sup>8</sup> Measured at TX06

Level of Decomposition	Arrival #	Vh	Back-azimuth
1	1	0.338	348.9
2	2	0.355	346.7
3	3	0.345	344.5

Table IV. Wavelet processing of infrasound arrivals from STS-69.

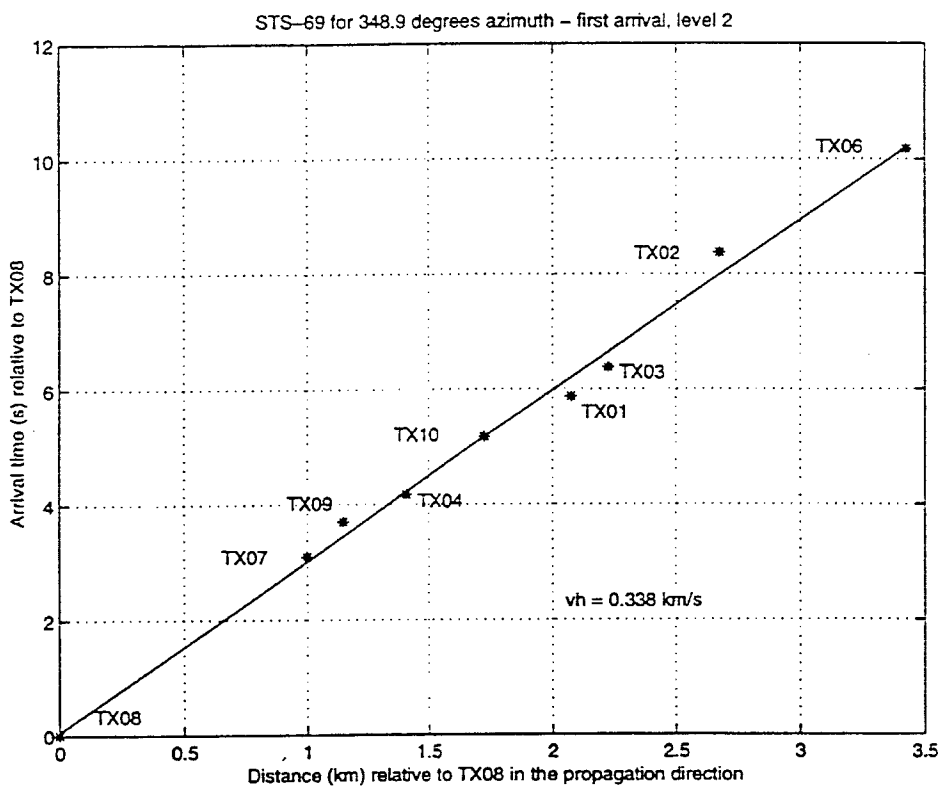


Figure 2-10. Results of processing the first infrasound arrival for STS-69 using wavelet decomposition.

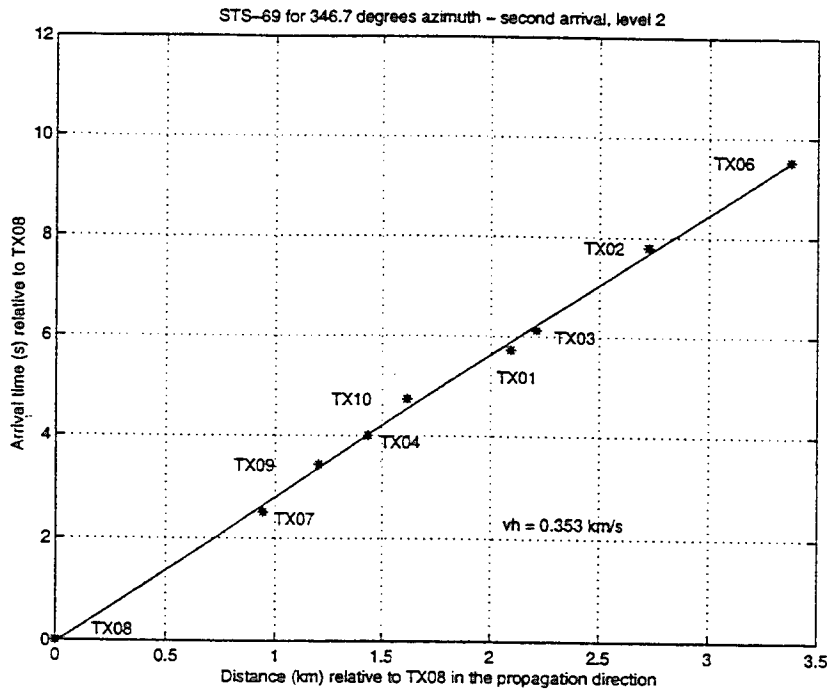


Figure 2-11. Results of processing the second infrasound arrival for STS-69 using wavelet decomposition.

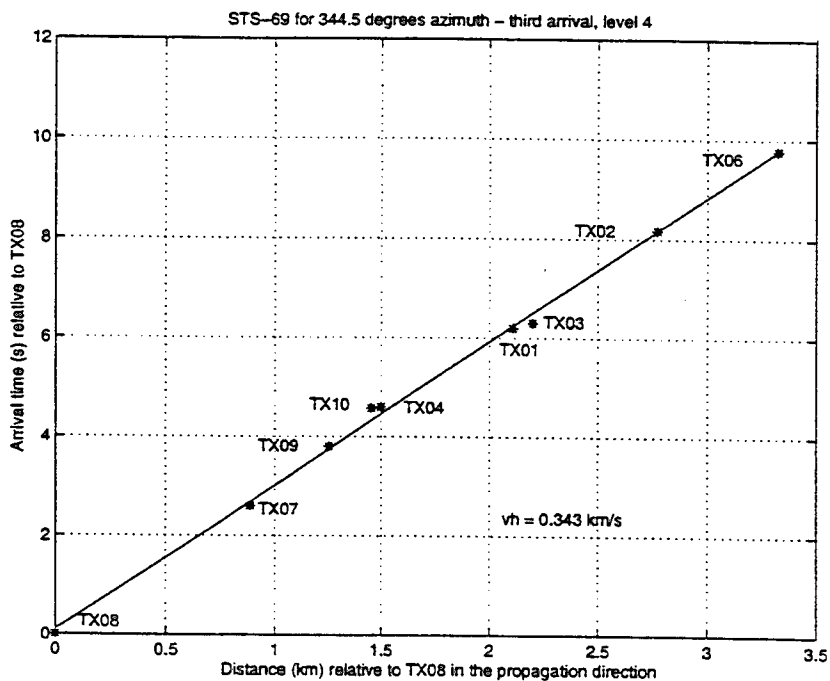
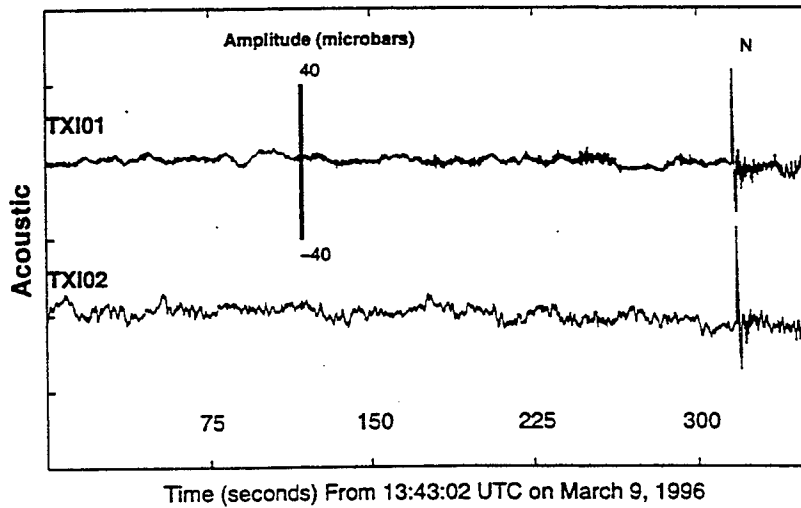
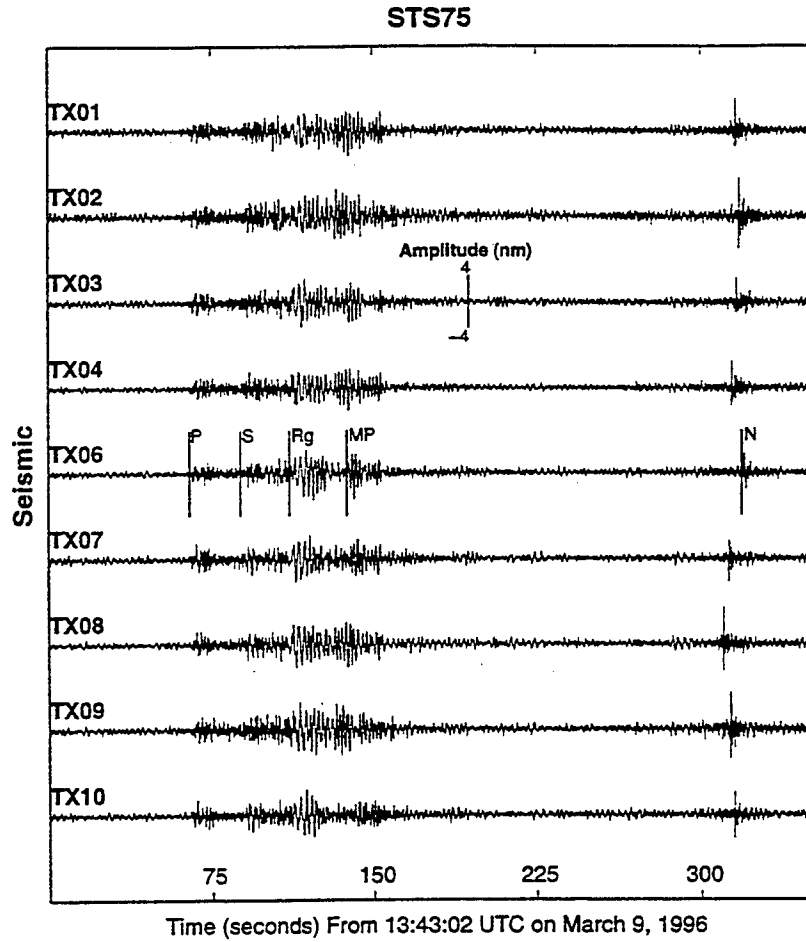


Figure 2-12. Results of processing the third infrasound arrival for STS-69 using wavelet decomposition.



**Figure 2-13. Shuttle quakes and N waves from STS-75.**

## STS-75 PARAMETERS

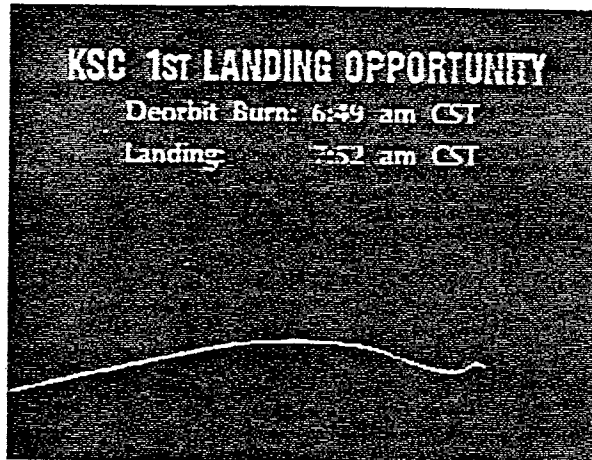
Shuttle: Columbia

Mission Dates: February 22-March 9, 1996

Landing: KSC at 13:58:38 UTC

Mission: Deployment of the Tethered Satellite System Reflight

Landing Groundtrack: Approximately 150 km north of TXAR bearing 95°



Phase	Arrival Time <sup>9</sup>	Back-azimuth	Velocity	Quality
P <sub>1</sub>	13:44:06.95	289.7	7.2	A
P <sub>2</sub>	13:44:15.1	328.7	7.8	B
S	13:44:32.7	318.9	4.1	B
R <sub>1</sub>	13:44:54.7	343	2.9	A
Re-multipath	13:45:19.6	352	2.7	B
R <sub>2</sub>	13:48:27.3	349.9	0.356	A

Table V. Mission information and results of processing seismic and acoustic signals from STS-75.

<sup>9</sup> Measured at TX06

<sup>10</sup> Only two acoustic channels available, thus measurements obtained using level 2 wavelet decomposition of the seismo-acoustics channels.

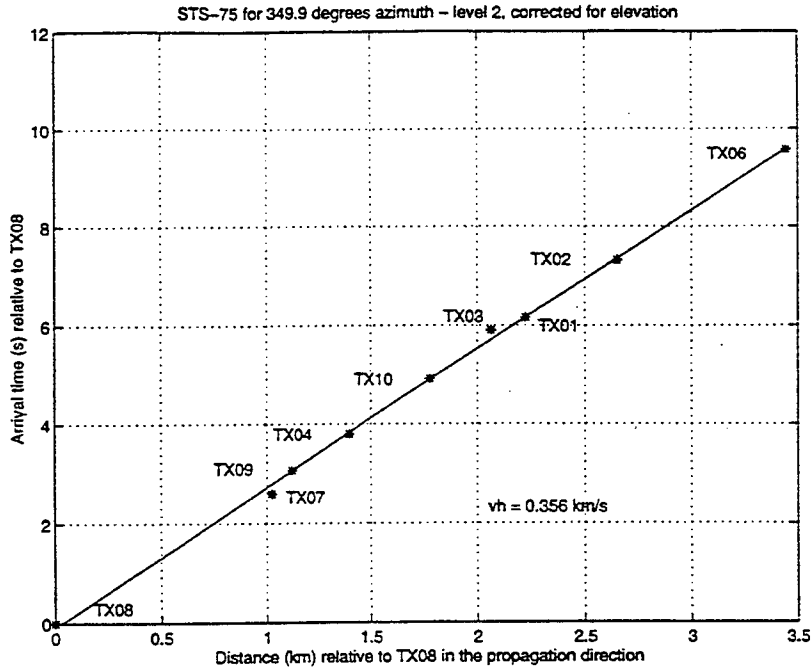


Figure 2-14. Results of processing the infrasound arrival for STS-75 using wavelet decomposition. The results are corrected for elevation differences of stations at TXAR.

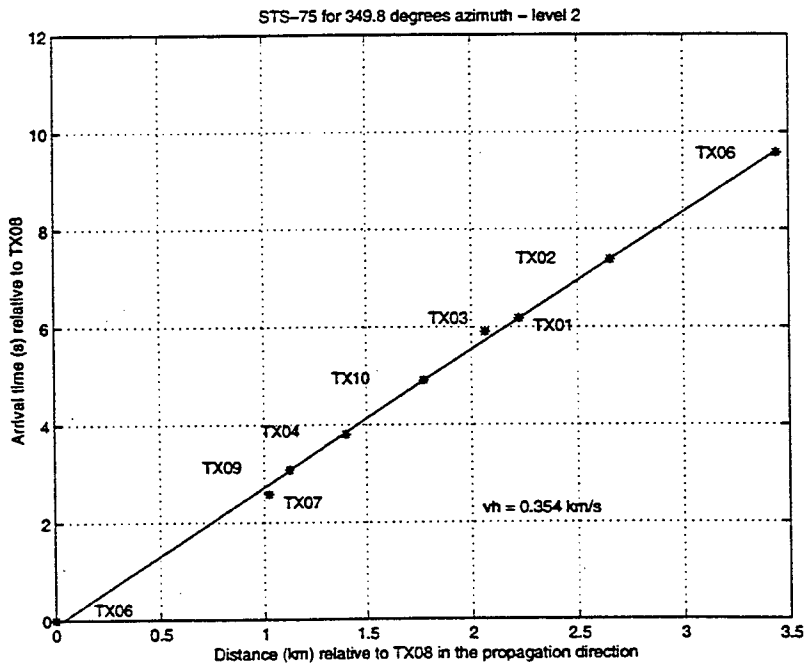


Figure 2-15. Results of processing the infrasound arrival for STS-75 using wavelet decomposition. The results are not corrected for elevation differences of stations at TXAR.

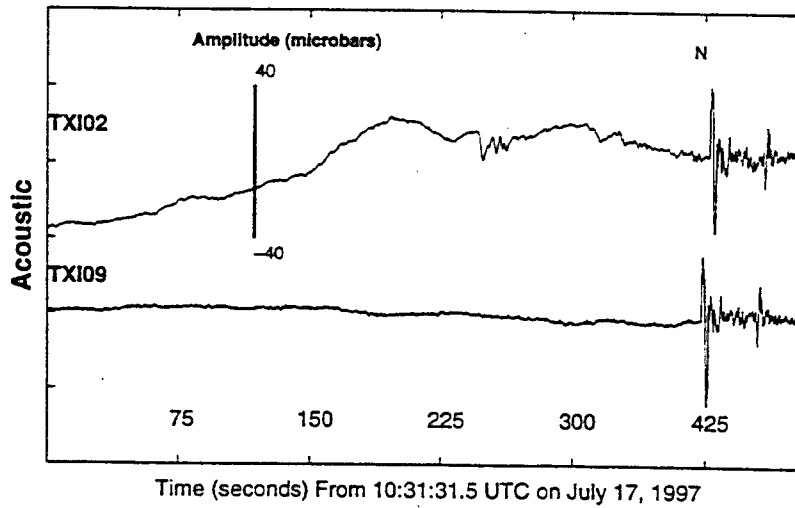
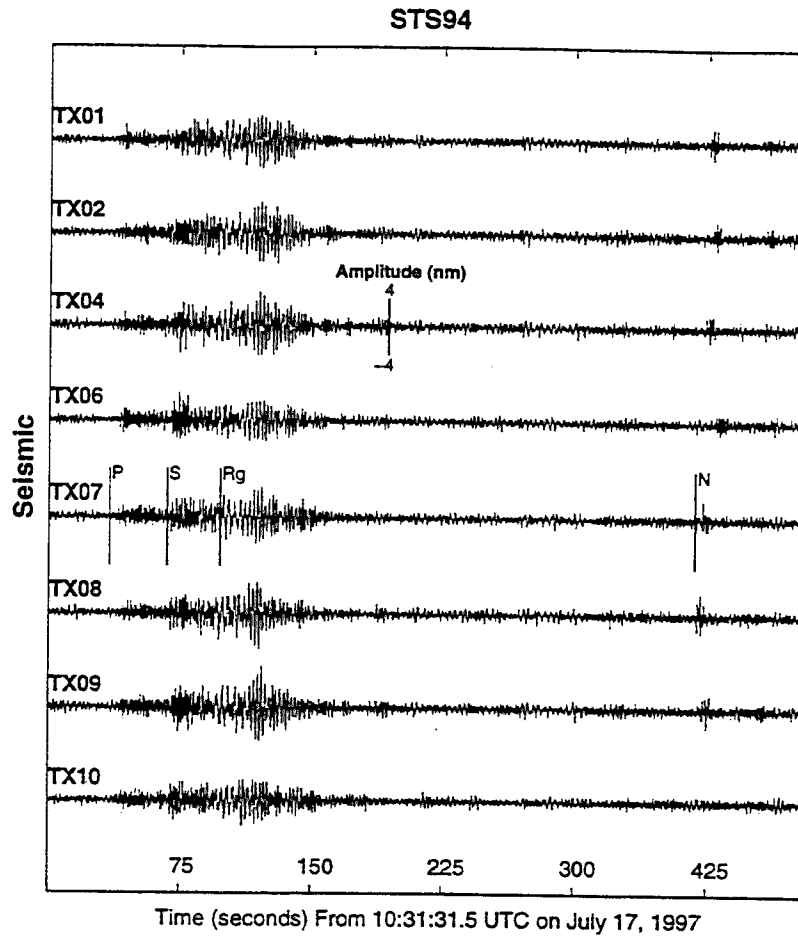


Figure 2-16. Shuttle quakes and N waves from STS-94.

## STS-94 PARAMETERS

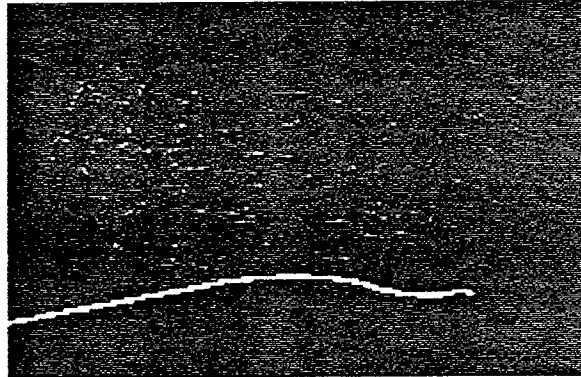
Shuttle: Columbia

Mission Dates: July 1-17, 1997

Landing: KSC at 10:46:34 UTC

Mission: Reflight of Microgravity Science Laboratory

Landing Groundtrack: Approximately 150 km north of TXAR bearing 80°.



Phase	Arrival Time <sup>11</sup>	Back-azimuth	Velocity	Quality
P	10:32:09.65	283	7.2	
P	10:32:13.3	286	7.1	
S	10:32:41.13	317	3.9	
R <sub>h</sub>	10:33:03.9	315	2.7	

Table VI. Mission information and results of processing seismic signals from STS-94.

Level of Decomposition	Arrival #	V <sub>h</sub>	Back-azimuth
1	1	0.341	348.7
2	2	0.325	348.6
3	3	0.328	345.3

Table VII. Wavelet processing of infrasound arrivals from STS-94.

<sup>11</sup> Measured at TX06

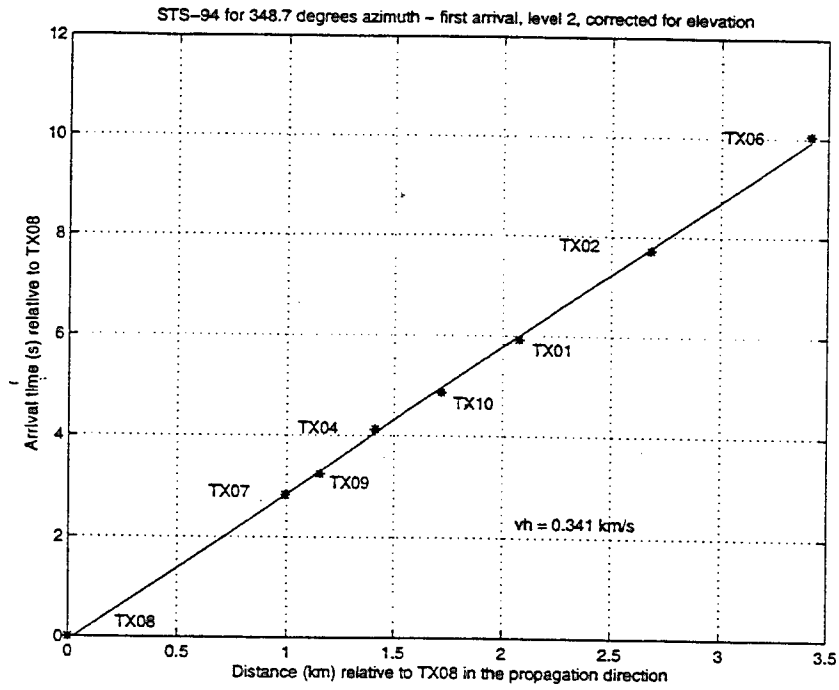


Figure 2-17. Wavelet processing of the first infrasound arrival from STS-94.

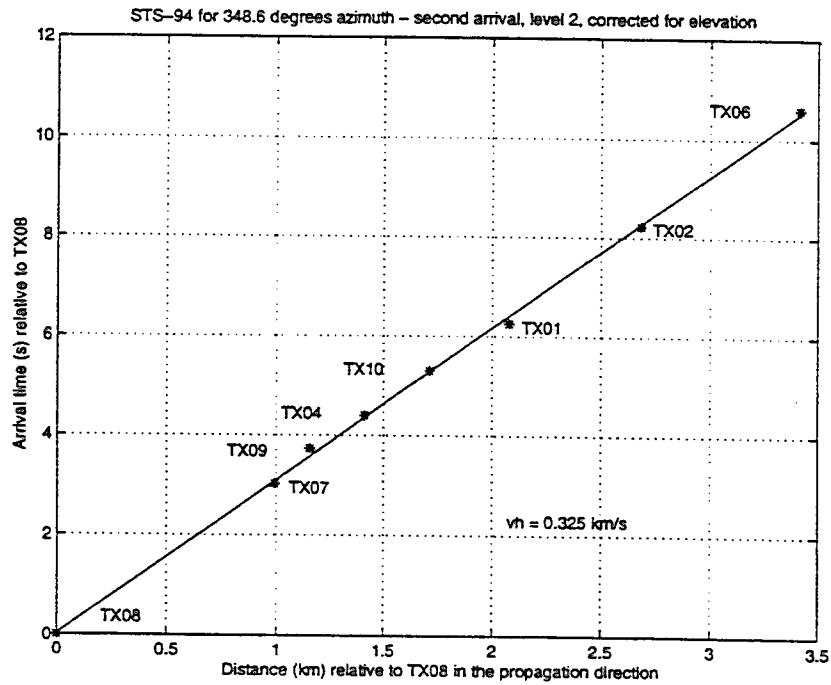


Figure 2-18. Wavelet processing of the second infrasound arrival from STS-94.

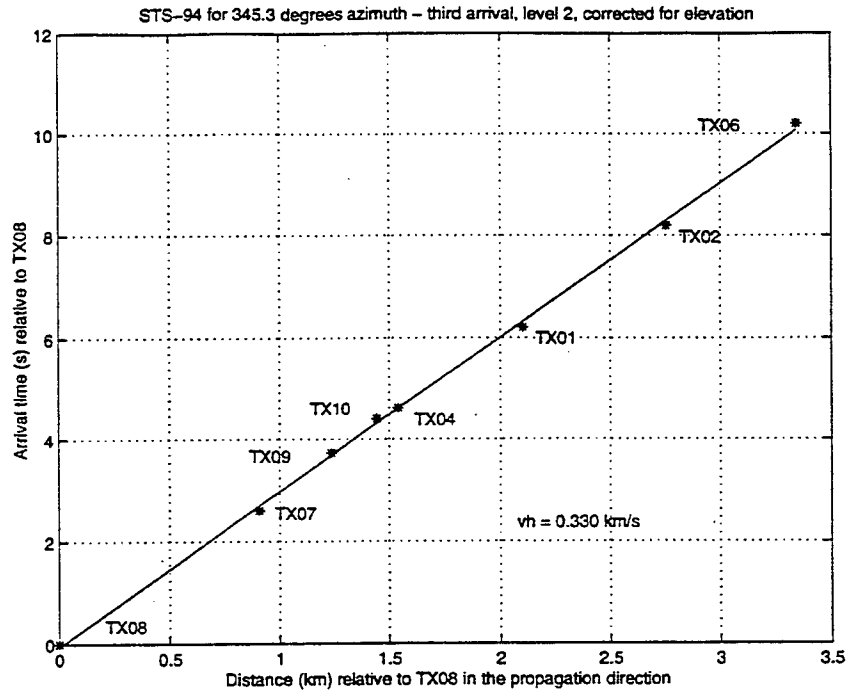
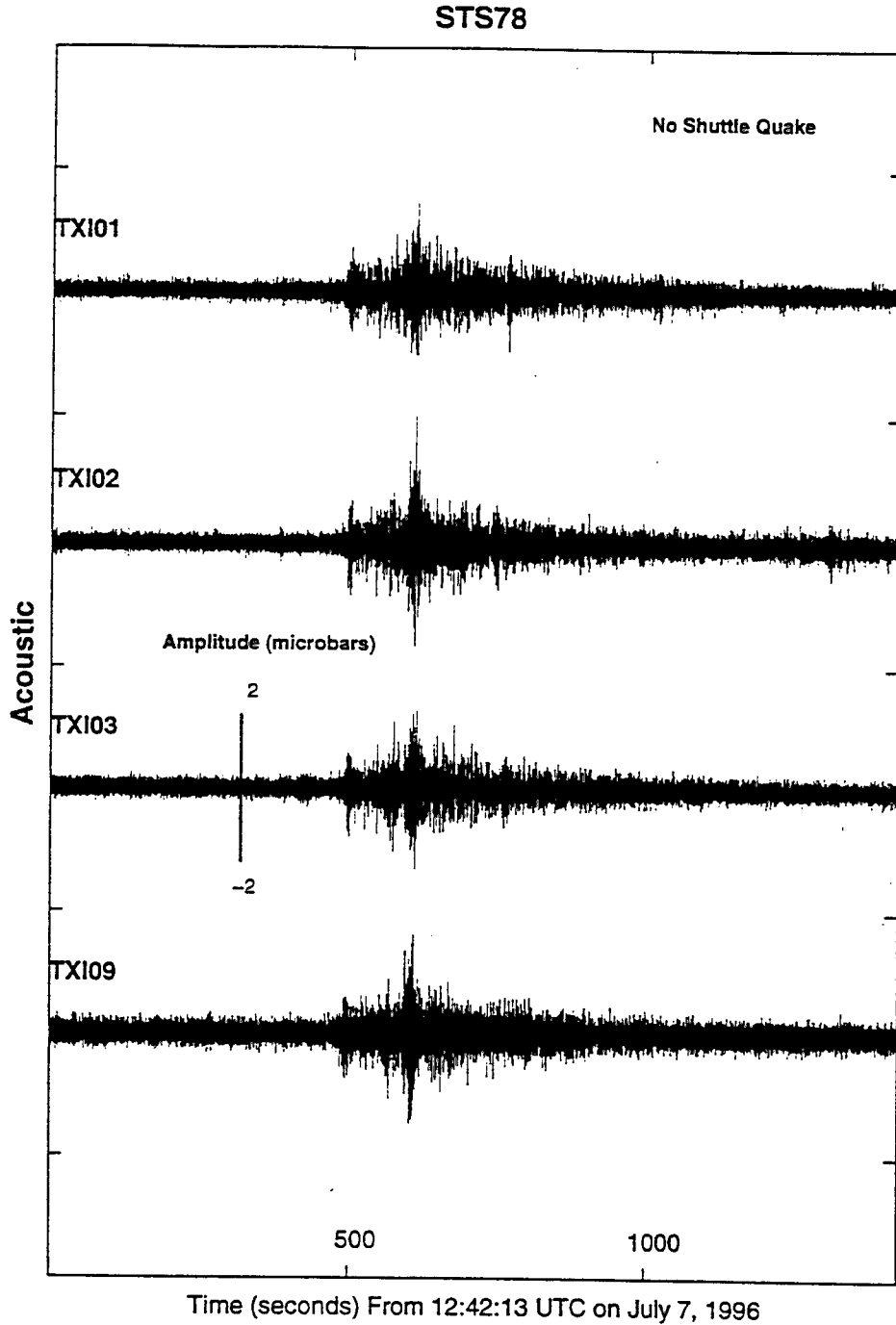


Figure 2-19. Wavelet processing of the third infrasound arrival from STS-94.



**Figure 2-20. Infrasonic from the shuttle mission STS-78 recorded at TXAR. The shuttle passed far enough from TXAR that no N wave or shuttle quake was observed.**

## STS-78

Shuttle: Columbia

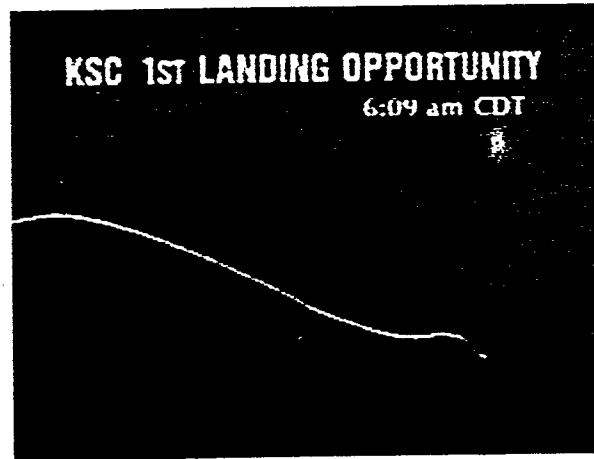
Mission Dates: June 20-July 7, 1996

Landing: KSC at 12:37:30 UTC

Mission: Experimenting with the Life and Microgravity Spacelab

Note: No shuttle quake

Landing Groundtrack:



Times do not correspond to STS-78 landing.

Phase	Arrival Time <sup>12</sup>	Azimuth	Velocity	Quality
	12:50:26.4	153	0.36	
	12:50:51.3	151	0.35	
	12:51:09.8	154	0.35	
	12:51:26.6	157	0.35	
	12:52:08.3	15	0.34	

Table VIII. Mission information and results of processing acoustic signals from STS-78. Five different acoustic signals were processed.

<sup>12</sup> Measured from TXI03

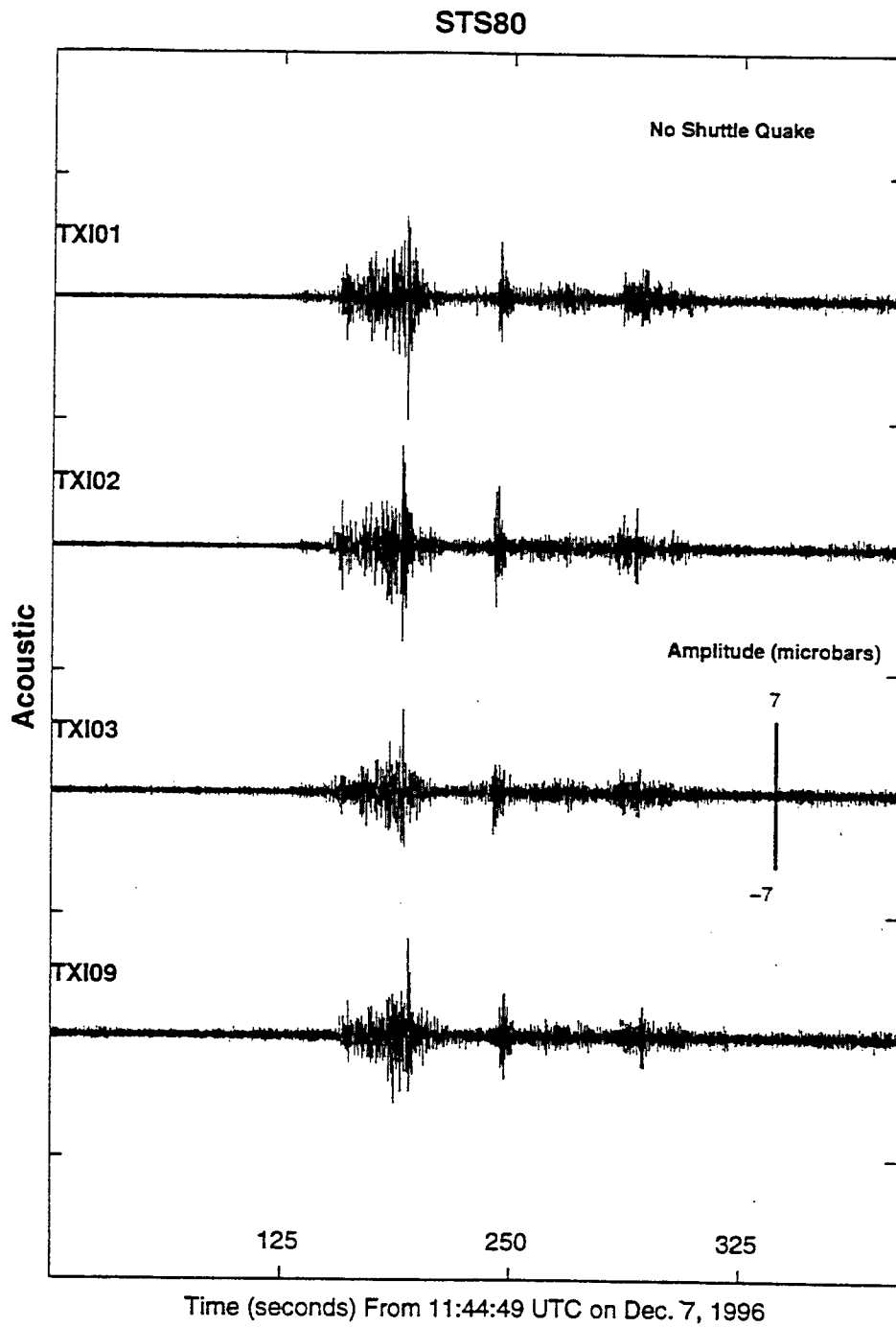
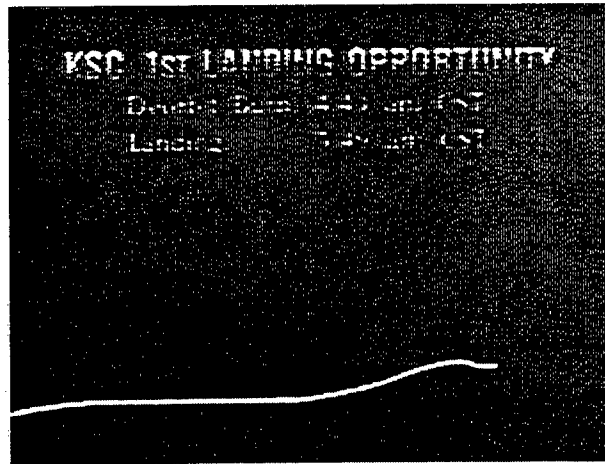


**Figure 2-21. Infrasonic from the shuttle mission STS-80.**

## STS-80

Shuttle: Columbia  
 Mission Dates: November 19-December 7, 1996  
 Landing: KSC at 11:49:05 UTC  
 Mission: 3<sup>rd</sup> Flight of the Wake Shield Facility  
 Note: No shuttle quake  
 Landing Groundtrack:



Phase	Arrival Time <sup>13</sup>	Azimuth	Velocity	Quality
1	11:46:57.6	135.2	0.34	
2	11:47:15.7	134.4	0.34	
3	11:47:44.6	169.7	0.35	
4	11:48:45.2	136.1	0.34	
5	11:50:00.9	163.9	0.36	

Table IX. Mission information and results of processing acoustic signals from STS-80.  
 Five separate acoustic signals were processed.

<sup>13</sup> Measured from TXI03

### APPENDIX 3. SEISMIC "BOW" WAVES

G. G. Sorrells

#### PART I. FORMULATION OF THE PROBLEM

Objects such as meteorites and space shuttle craft can travel at speeds in excess of mach 10. Since maximum shock overpressures scale as the square of the mach number, a significant shock front will be developed and sustained by the movement of these objects through the atmosphere. The intersection of the shock front with the surface of the earth will generate elastic disturbances which, depending upon the ground speed of the shock front relative to the local horizontal seismic phase velocities will be seen by observers near the ground path of the object as either propagating seismic waves, or as inhomogeneous waves. These waves are referred to in this paper as seismic "bow" waves because of their resemblance to the fluid waves generated by the movement of a ship's bow through water. An approximate theory which explains the generation of seismic "bow" waves by a hypersonic shock front is developed in the following paragraphs.

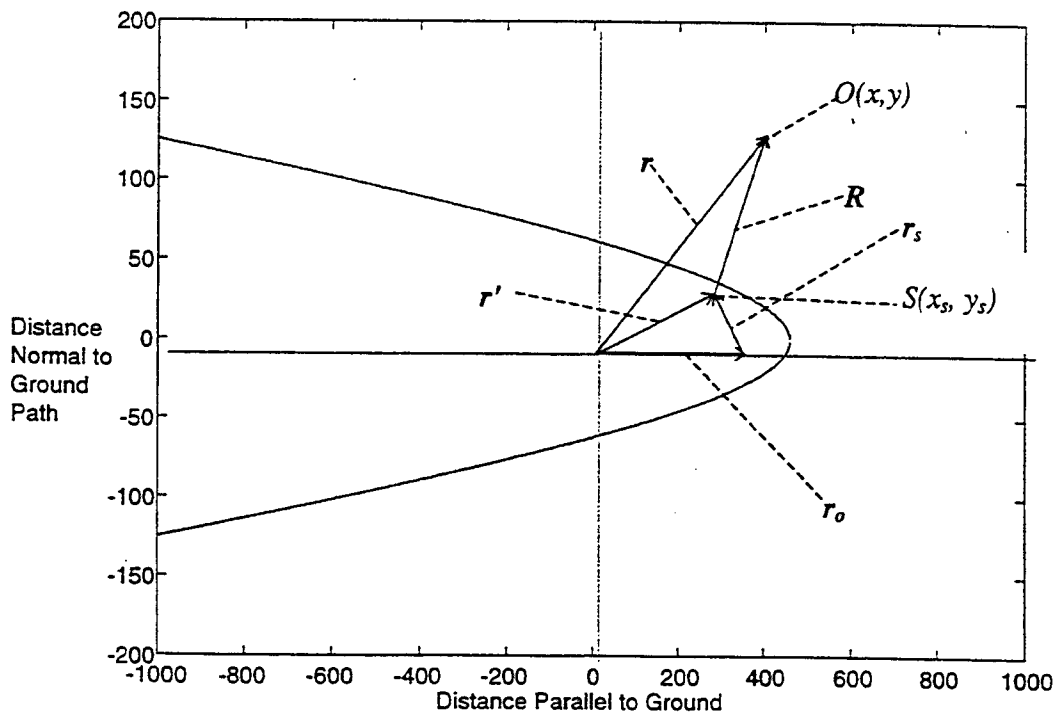


Figure 3-1. Trace of an idealized shock front in the X-Y plane at time  $t'$ . Position vectors necessary to describe the seismic response to the shock front are shown as arrows (See text for additional details)

### Definitions

The surface of the earth is approximated by the X-Y plane seen in Figure 3-1. The X axis is chosen to coincide with the ground path of the hypersonic object which is assumed to be moving at ground speed,  $v$ , in the positive X direction. Let  $\hat{e}_x$  and  $\hat{e}_y$  be unit vectors in the positive X and Y directions, respectively. Then,  $\bar{V}$ , the horizontal phase velocity of the shock front is given by;

$$\bar{V} = v\hat{e}_x \quad 1$$

Now let  $t'$  be the time after the initial contact of the shock front with the surface of the earth and suppose that  $\bar{r}_o$  identifies a point which moves at velocity,  $\bar{V}$ , along the X axis. i.e.;

$$\bar{r}_o = vt' \hat{e}_x \quad 2$$

Assume that  $\bar{r}_s$  locates the point  $S(x_s, y_s)$  with respect to a moving origin at  $\bar{r}_o$ . Then

$$\bar{r}_s = x_s \hat{e}_x + y_s \hat{e}_y \quad 3$$

Now let  $\bar{r}'$  locate the same point with respect to the fixed origin. Then

$$\bar{r}' = \bar{r}_o + \bar{r}_s = (x_s + vt')\hat{e}_x + y_s \hat{e}_y \quad 4$$

Let  $\bar{r}$  locate the observation point,  $O(x, y)$  with respect to the fixed origin. Then

$$\bar{r} = x\hat{e}_x + y\hat{e}_y \quad 5$$

Let  $\bar{R}$  locate the  $O$  with respect to  $S$ . Then,

$$\bar{R} = \bar{r} - \bar{r}' = (x - x_s - vt')\hat{e}_x + (y - y_s)\hat{e}_y \quad 6$$

Now suppose  $\bar{k}_c$  is a horizontal wave number vector for a seismic wave which propagates in the direction  $\phi$  with horizontal phase speed,  $c$ . Then,

$$\bar{k}_c = \frac{\omega}{c} (\cos \phi \hat{e}_x + \sin \phi \hat{e}_y) \quad 7$$

where  $\phi$  is measured counterclockwise with respect to the positive X axis;  $\omega = 2\pi f$  and  $f$  is the frequency.

### The Bow Wave Solution

Let  $P(\omega, \bar{r}_s)$  be the spectrum of the overpressure load instantaneously applied at the point  $S$  at time  $t'$ . The seismic disturbance created by this load,  $\delta u(\bar{R}, t - t')$ , as seen at the point  $O$  at some later time,  $t$  is given by

$$\delta u(\bar{R}, t - t') = A \frac{P(\omega, \bar{r}_s)}{|\bar{R}|^q} \exp[-i\omega(t - t')] \int_{k_c} \exp(i\bar{k}_c \cdot \bar{R}) dk_c \quad 8$$

where  $A$  is a constant dependent upon the elastic properties of the medium and  $q$  is the geometrical spreading coefficient. Let  $\Delta u(\bar{R}, t; T)$  be the sum of all the contributions

from this load from the time of the initial contact of the shock front with the surface of the earth to some time,  $T$ . Then

$$\Delta u(\bar{R}, t; T) = \int_0^T A \frac{P(\omega, \bar{r}_s)}{|\bar{R}|^q} \exp[-i\omega(t-t')] \int_{k_c} \exp(i\bar{k}_c \cdot \bar{R}) dk_c dt' \quad 9$$

Changing the order of integration and using equations. 1-7 to express the arguments in equation 9 in terms of their component, results in

$$\Delta u(x - x_s, y - y_s, t; vT) = AP(\omega, x_s, y_s) \exp\left\{-i\frac{\omega}{v}[vt - (x - x_s)]\right\} H(x - x_s, y - y_s; vT) \quad 10$$

where

$$H(x - x_s, y - y_s; vT) = \int_0^{2\pi} e^{i\frac{\omega}{c} \sin\phi(y - y_s)} \int_{x - x_s - vT}^{x - x_s} \frac{e^{i\frac{\omega}{c}(\cos\phi - \frac{c}{v})x}}{\left[\chi^2 + (y - y_s)^2\right]^{\frac{q}{2}}} d\chi d\phi \quad 11$$

It is shown in Part II that for large  $vT$  and  $|\bar{r} - \bar{r}_s| < vT$ ;

$$H(x - x_s, y - y_s; vT, q) \approx B(x - x_s - vT, y - y_s; q) \exp\left[\pm \frac{\omega}{c} \sqrt{1 - \frac{c^2}{v^2}} (y - y_s)\right] \quad 12$$

$\therefore$

$$\Delta u(x - x_s, y - y_s, t; vT) = APB \exp[-i\omega t] \exp[i\kappa_x(x - x_s) \pm i\kappa_y(y - y_s)] \quad 13$$

where

$$\kappa_x = \frac{\omega}{c} \left(\frac{c}{v}\right) \quad 14$$

$$\kappa_y = \pm \frac{\omega}{c} \sqrt{1 - \frac{c^2}{v^2}}$$

It is seen from equation 14 that  $\Delta u$  can take one of two different forms depending on the value of  $\frac{c}{v}$ . When  $\frac{c}{v} > 1$ ,  $\kappa_y$  is imaginary. Consequently, as illustrated by the dashed

line in Figure 3-2,  $\Delta u$  becomes an elementary inhomogeneous wave which is attached to the shock front at point  $(x_s, y_s)$ . It propagates with speed,  $v$ , along the path  $y = y_s$ , and its amplitude decays exponentially in directions normal to this path. On the other hand, if

$\frac{c}{v} \leq 1$ ,  $\kappa_y$  is real. Therefore, as illustrated by the solid lines in Figure 3-2,  $\Delta u$  describes

two elementary plane waves which are attached to the shock front at point  $(x_s, y_s)$ . The elementary plane wavefronts propagate at horizontal speed,  $c$ , in the directions  $\pm\phi_x$ , where

$$\phi_x = \cos^{-1}\left(\frac{c}{v}\right) \quad 15$$

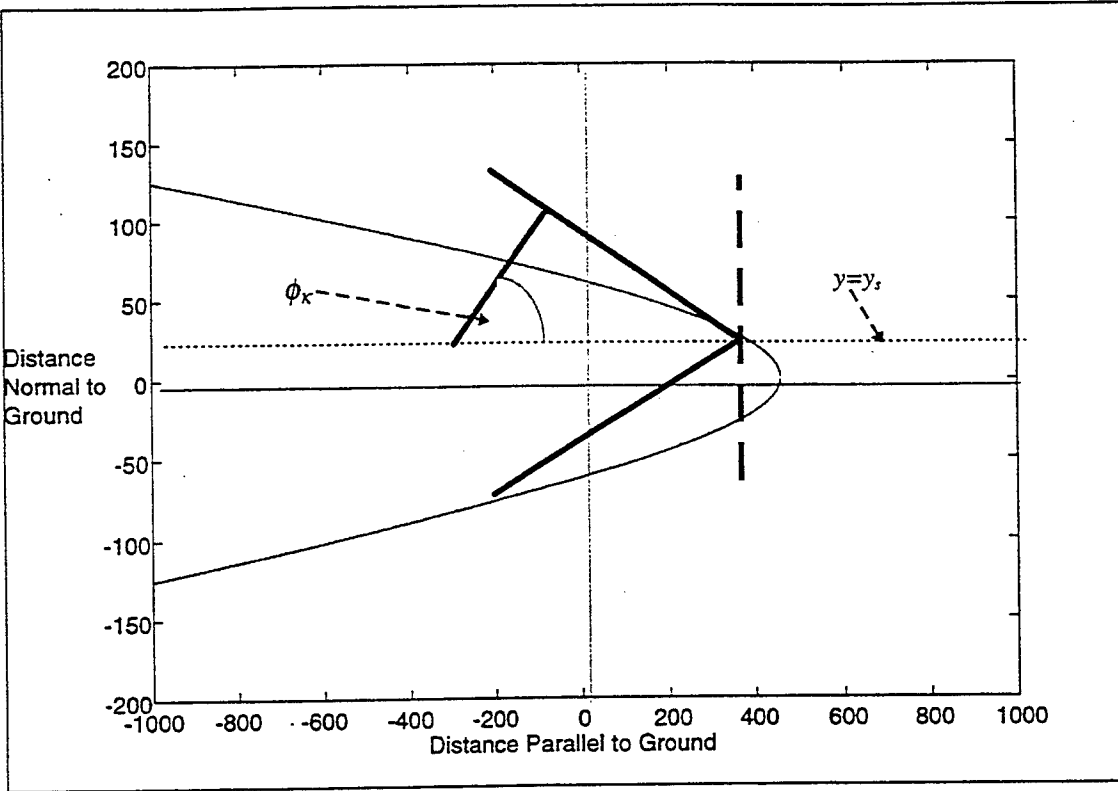


**Figure 3-2. Diagram of the elementary seismic bow wavefronts generated at the point  $(x_s, y_s)$  by a moving shock front. Elementary inhomogeneous bow waves (heavy dashed line) are generated when  $c > v$ . Elementary propagating plane bow waves (heavy solid lines) are generated when  $c \leq v$ .**

The waves generated by the moving point pressure load are referred to in this text as elementary seismic "bow" waves. Now let  $u$  be the resultant of the elementary "bow" waves generated at all the of the points on the shock front trace. Now, if  $g(x_s)$  describes the shock front trace with reference to an origin at  $\bar{r}_s$  and  $ds$  is an element of length along the shock front trace, then;

$$u(x, y, \kappa_x, \kappa_y; vT, q) = AN(x, y, \kappa_x, \kappa_y; vT, q, g) \exp(-i\omega t) \exp[i(\kappa_x x + \kappa_y y)] \quad 16$$

where

$$N(x, y, \kappa_x, \kappa_y; vT, q) = \int_{s=g(x_s)} F(x-x_s, y-g(x_s); vT, q) \exp[-i(\kappa_x x_s + \kappa_y g(x_s))] ds \quad 17$$

and

$$F = P(\omega, x_s, g(x_s)) B(x-x_s, y-g(x_s); vT, q) \quad 18$$

Equation 16 is the formal solution for the seismic response to a moving shock front imposed upon the surface of the earth. It is important to note that  $u$  retains the phase behavior of  $\Delta u$ , that is;  $u$  describes two propagating plane bow waves when  $c \leq v$  and an inhomogeneous bow wave when  $c > v$ . The essential difference between  $u$  and  $\Delta u$  is the

occurrence of the complex amplitude factor,  $N$  on the right hand side of equation 16. It can be seen from equation 18 that  $F$  is a complex, non-linear function of  $x_s$ . Consequently, it would be difficult to obtain closed form solution for  $N$  given reasonable assumptions about the behavior of  $P$  and  $g$ . Fortunately, much can be inferred about the behavior of  $N$  by the examination of the simple model of the shock front trace which is identified below.

As shown in Figure 3-3, let

$$g(x_s) = \pm \cot(\theta)(x_s - d)$$

19

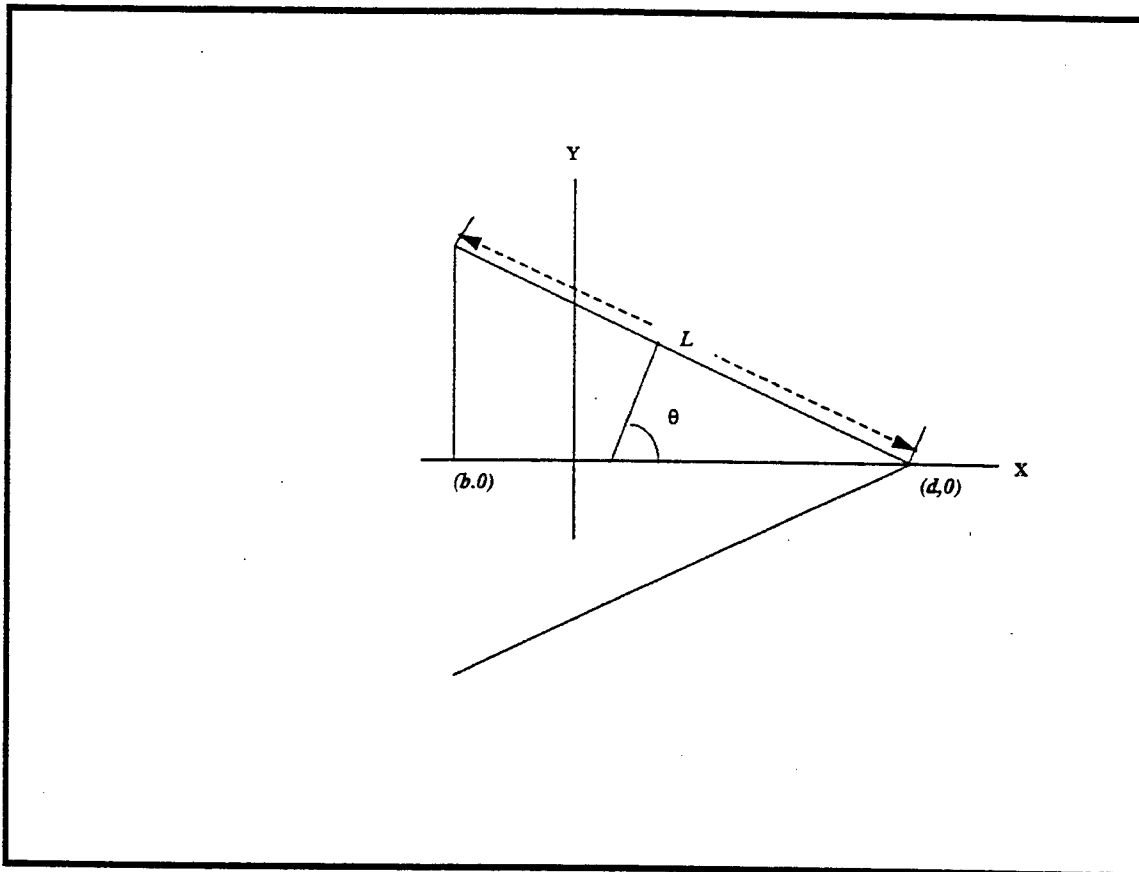


Figure 3-3. A diagram of a simplified model of the shock front trace.

where  $g(x_s)$  is defined only in the interval,  $b \leq x_s \leq d$ ,  $\theta$  is the orientation of the normal to the shock front trace, and the point,  $(d, 0)$  is the intersection point of the two wings of the shock front trace. Now assume that  $c \leq v$  so that  $\kappa_y$  is real. Moreover, for the sake of simplicity assume that  $P$  is independent of  $x_s$  and that as shown in Figure 3-3, the shock front trace wings are of length,  $L$ . Then, neglecting the effects of geometric spreading,  $N$  for this particular case is given by;

$$N = \frac{P}{\sin(\theta)} \int_b^d \exp - [i(\kappa_x x_s - \kappa_y \cot(\theta)(x_s - d))] dx_s, \quad 20$$

By making the substitution  $\zeta = x_s - d$  and recognizing that  $b - d = -L \sin(\theta)$  it may be readily deduced that;

$$N = 2P \exp\left(-i \frac{\omega}{c} \cos(\phi_x) d\right) \exp\left(i \frac{\omega L}{2c} \sin(\theta - \phi_x)\right) \frac{\sin\left(\frac{\omega L}{2c} \sin(\theta - \phi_x)\right)}{\frac{\omega}{c} \sin(\theta - \phi_x)} \quad 21$$

It can be seen by inspection of equation 21 that

$$\frac{|N|}{PL} = \left| \frac{\sin(\xi)}{\xi} \right| \quad 22$$

where

$$\xi = \left( \frac{\omega L}{2c} \sin(\theta - \phi_x) \right) \quad 23$$

which illustrates that the normalized modulus of  $N$  for this simple model of the shock front trace is equal to the modulus of a sinc or aperture function. The normalized modulus of  $N$  is plotted in Figure 3-4 with  $\theta - \phi_x$  as the independent variable.

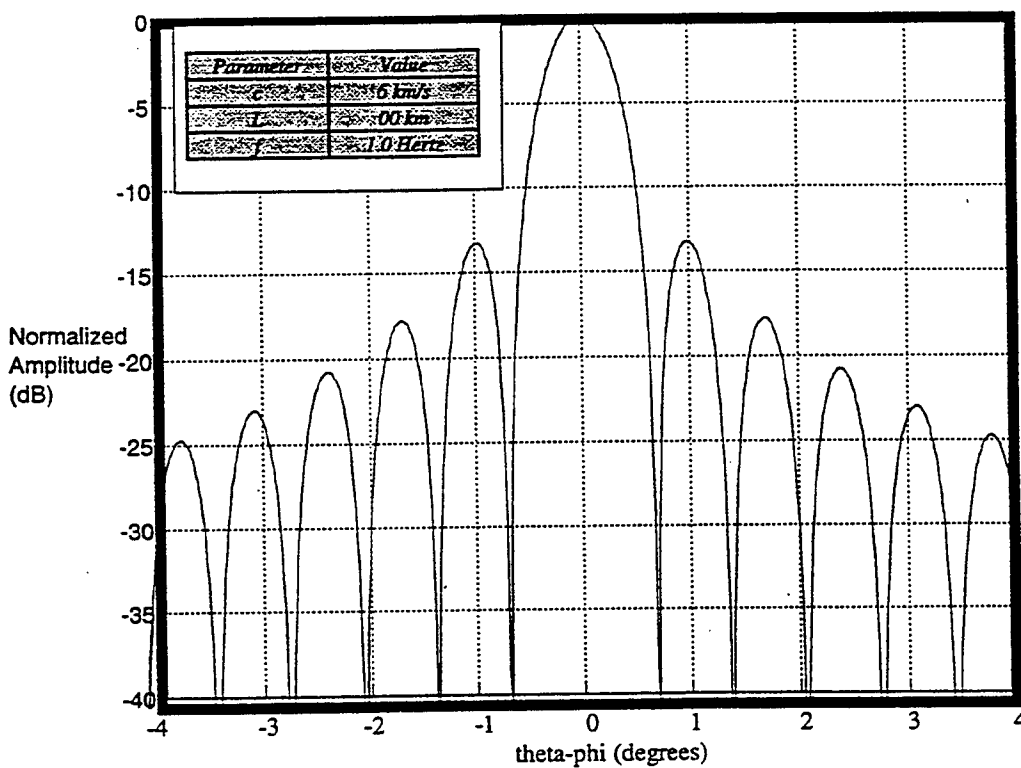


**Figure 3-4. Normalized Modulus of  $N$  for the simplified model of the shock front trace (see text for details).**

The parameters used for these calculation are shown in the panel in the upper left corner of the figure. They are appropriate for a high frequency Pg bow wave generated by a

shock front with a relatively long ground path. The results seen in Figure 3-4 demonstrate that  $N$  is maximized when the normal to the trace of the shock wave front is closely aligned with  $\bar{\kappa}$  and diminishes rapidly as the misalignment increases. In particular, it should be noted that for this set of model parameters, that if the misalignment is greater than about  $\pm 4^\circ$ , then the normalized value of  $|N|$  is down more than 25 dB with respect to its peak value. These results indicate that the elementary bow waves generated by the point sources distributed along the shock front trace will be strongly attenuated by destructive interference unless the normal to the shock front traces happens to be approximately parallel to  $\bar{\kappa}$ .

A similar behavior can be reasonably anticipated that for actual shock front traces. However, in this case  $\theta$  is not a constant, but rather it is a continuous variable defined in the range:

$$-\cos^{-1}\left(\frac{c_a}{v}\right) \leq \theta \leq \cos^{-1}\left(\frac{c_a}{v}\right) \quad 23$$

where  $c_a$  is the local sound speed. Consequently, it is argued that for actual shock fronts with relatively long ground paths, destructive interference will strongly attenuate the elementary bow waves generated everywhere along the trace except at those points where  $\theta \equiv \phi_x$ . The spatial relationship between the shock front and its associated bow wave implied by this argument are conceptually illustrated in Figure 3-5.

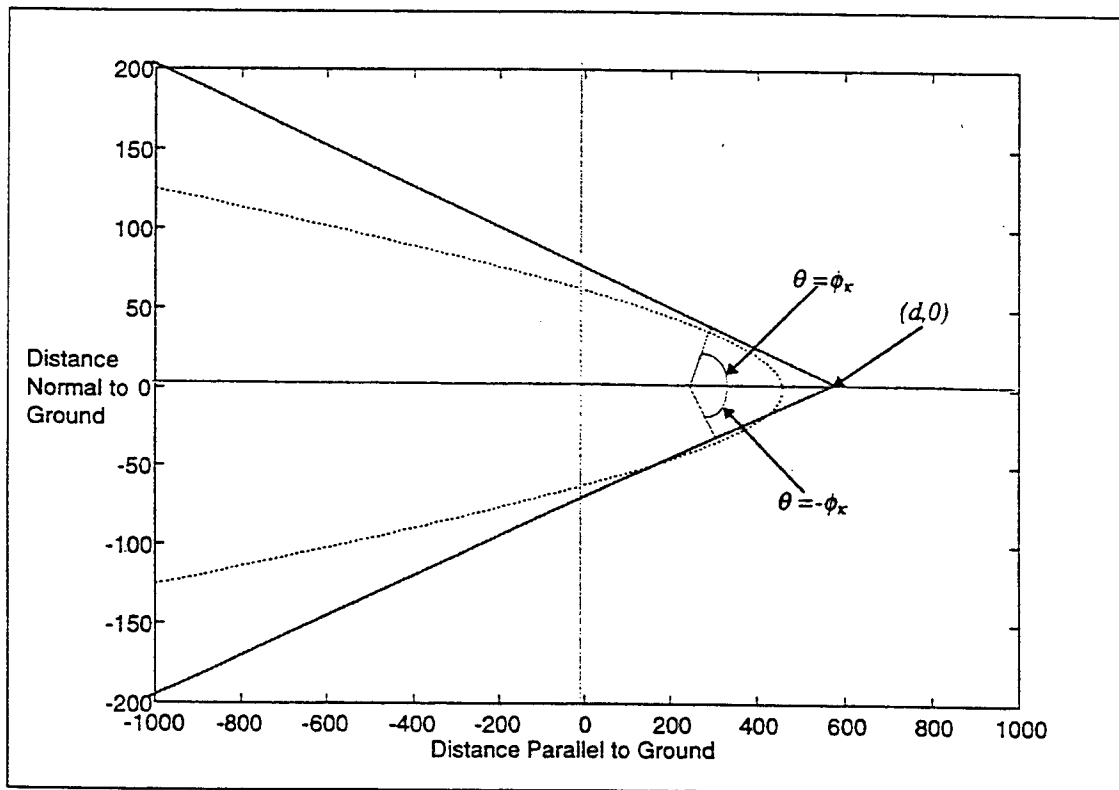


Figure 3-5. Spatial relationship between the shock front trace (dashed) and its associated bow wave (solid).

It can be seen from this figure that the bow wave front is tangent to the shock front at the points where the  $\theta = \pm\phi_x$  and intersects the X axis at the point  $(d,0)$ . It is also important to note that if  $c(\theta)$  denotes the speed of the shock front in the direction  $\theta$ , then

$$c(\theta) = v \cos(\theta) \quad 24$$

and at the points where  $\theta = \pm\phi_x$

$$c(\theta) = v \cos(\pm\phi_x) = c \quad 25$$

In other words, when  $c \leq v$ , bow waves will "couple" to the shock front at those points where its horizontal phase speed is equal to the horizontal speed of seismic waves in the underlying medium. Finally, based upon this argument, it follows that

$$u \approx AW \exp[i\kappa_x(x-d)] \exp[i\kappa_y y] \quad 26$$

where W is a function which accounts for the overpressure distribution along the shock front trace as well as the effects of geometrical spreading.

**PART II. SEISMIC "BOW" WAVES GENERATED BY MOVING POINT  
PRESSURE LOADS APPLIED AT THE SURFACE OF THE EARTH**

It is shown in the accompanying paper that the earth motion observed at time,  $t$ , and at the point  $(x, y)$  due to a point pressure load which has moved at speed  $v$  on the line  $y=y_s$  parallel to the  $X$  axis over a period of time  $T$  may be expressed as

$$\Delta u = AP(\omega) \exp\left\{-i\omega\left[t - \frac{x - x_s}{v}\right]\right\} H \quad 1$$

where

$$H = \int_0^{2\pi} e^{i\frac{\omega}{c}\sin\phi(y-y_s)} \int_{x-x_s-vT}^{x-x_s} \frac{e^{i\frac{\omega}{c}(\cos\phi-\frac{c}{v})x}}{\left[\chi^2 + (y - y_s)^2\right]^{\frac{3}{2}}} d\chi d\phi \quad 2$$

In order to simplify the notation, let

$$x_s = y_s = 0$$

$$k_x = \frac{\omega}{c} \cos \phi$$

$$k_y = \frac{\omega}{c} \sin \phi$$

$$L = vT$$

Now let  $W$  be defined by;

$$W\left(\frac{\omega}{v} - k_x; x, y, L\right) = \int_{x-L}^x \frac{\exp\left[-i\left(\frac{\omega}{v} - k_x\right)\chi\right]}{\left(\chi^2 + y^2\right)^{\frac{3}{2}}} d\chi \quad 3$$

then

$$H = \int_0^{\omega} \exp\left[\pm i\sqrt{\left(\frac{\omega^2}{c^2} - k_x^2\right)}y\right] W\left(\frac{\omega}{v} - k_x; x, y, L\right) dk_x \quad 4$$

It can be seen from equation 4 that  $H$  may be identified as a convolution in the wave number domain between a plane wave and the function,  $W$ . Moreover, it may be seen from equation 3 that  $W$  may be viewed as the wave number spectrum of the output of a phased linear source array of length,  $L$ , whose individual inputs are amplitude weighted by the geometrical spreading factor. An expression for  $W$  is derived in the following section.

**Evaluation of  $W$  for Body Wave Inputs**

Let

$$\eta = \frac{\omega}{v} - k_x \quad 5$$

Then, it follows directly from equation 3 that

$$W = \frac{1}{2\pi} \int_{-\infty}^{\infty} f_1(\lambda) f_2(\eta - \lambda) d\lambda \quad 6$$

where

$$f_1 = \int_{x-L}^x \exp(-i\eta\chi) d\chi \quad 7$$

is the wave number spectrum of a linear source array, and

$$f_2 = \int_{-\infty}^{\infty} \frac{\exp(-i\eta\chi)}{(\chi^2 + y^2)^{\frac{q}{2}}} d\chi \quad 8$$

is the one dimensional wave number spectrum of the geometrical spreading factor. It is straightforward to show that:

$$f_1 = 2 \exp\left[-i\eta\left(x - \frac{L}{2}\right)\right] \frac{\sin\left(\frac{\eta L}{2}\right)}{\eta} \quad 9$$

and assuming

$$q=2$$

which is valid for far field body waves generated by a surface point source, the calculus of residues may be used to show that:

$$f_2 = \pi \frac{\exp(-|\eta|y)}{y} \quad 10$$

$\therefore$

$$W = \frac{1}{y} \int_{-\infty}^{\infty} \exp\left[-i\eta\left(x - \frac{L}{2}\right)\right] \sin\left(\frac{\lambda L}{2}\right) \exp(-|\eta - \lambda|y) \frac{d\lambda}{\lambda} \quad 11$$

By replacing  $\sin\left(\frac{\lambda L}{2}\right)$  in equation 11 with its exponential representation, it can be shown that;

$$W = \frac{i}{2y} \left\{ \exp(\eta y) [E_1(z_1^* \eta) - E_1(z_2^* \eta)] - \exp(-\eta y) [E_1(-z_1 \eta) - E_1(-z_2 \eta)] \right\} \quad 12$$

where

$$E_1(\zeta) = \int_{\zeta}^{\infty} \frac{\exp(-u)}{u} du \quad 13$$

is the exponential integral; and

$$z_1 = y - ix \quad 14$$

$$z_2 = y - i(x - L)$$

and the \* indicates the complex conjugate.

For small values of  $\eta$ ,  $E_1$  may be safely represented by a Maclaurin series of the form

$$E_1(\zeta) = -D - \log_e(\zeta) - \sum_{n=1}^{\infty} \frac{\zeta^n}{n \cdot n!} \quad 15$$

where  $D$  is the Euler-Mascheroni constant. Substitution of this series into equation 12 yields;

$$\text{Re } W = \frac{1}{y} \left\{ \cosh(\eta y) \beta + \sinh(\eta y) \sum_{n=1}^{\infty} \frac{imz_{2n-1} \eta^{2n-1}}{(2n-1) \cdot (2n-1)!} - \cosh(\eta y) \sum_{n=1}^{\infty} \frac{imz_{2n} \eta^{2n}}{2n \cdot 2n!} \right\} \quad 16$$

$$\text{Im } W = \frac{1}{y} \left\{ \sinh(\eta y) \alpha - \cosh(\eta y) \sum_{n=1}^{\infty} \frac{rez_{2n-1} \eta^{2n-1}}{(2n-1) \cdot (2n-1)!} - \sinh(\eta y) \sum_{n=1}^{\infty} \frac{rez_{2n} \eta^{2n}}{2n \cdot 2n!} \right\}$$

where

$$\alpha = \operatorname{Re} \left[ \log_e \left( \frac{z_2}{z_1} \right) \right] \quad 17\text{-a}$$

$$\beta = \operatorname{Im} \left[ \log_e \left( \frac{z_2}{z_1} \right) \right] \quad 17\text{-b}$$

$$\operatorname{Re} z_n = \operatorname{Re} [z_1^n] - \operatorname{Re} [z_2^n] \quad 17\text{-c}$$

$$\operatorname{Im} z_n = \operatorname{Im} [z_1^n] - \operatorname{Im} [z_2^n] \quad 17\text{-d}$$

It can be seen from these equations that

$$W(-\eta) = W^*(\eta) \quad 18$$

For larger values of  $\eta$ ,  $E_1$  should be represented by its asymptotic expansion

$$E_1(\zeta) \approx \exp(-\zeta) \left[ \frac{1}{\zeta} - \frac{1}{\zeta^2} + \frac{2!}{\zeta^3} - \frac{3!}{\zeta^4} + \dots (-1)^{n-1} \frac{(n-1)!}{\zeta^n} \right] \quad 19$$

In this case substitution of the asymptotic expansion into equation 12 yields

$$\operatorname{Re} W \approx \frac{1}{y} \left\{ \frac{\sigma_1(\eta)}{\eta} - \frac{\sigma_2(\eta)}{\eta^2} + 2 \frac{\sigma_3(\eta)}{\eta^3} + \dots (-1)^{n-1} \frac{(n-1)! \sigma_n(\eta)}{\eta^n} \right\} \quad 20$$

$$\operatorname{Im} W \approx \frac{1}{y} \left\{ \frac{\xi_1(\eta)}{\eta} - \frac{\xi_2(\eta)}{\eta^2} + 2 \frac{\xi_3(\eta)}{\eta^3} + \dots (-1)^{n-1} \frac{(n-1)! \xi_n(\eta)}{\eta^n} \right\}$$

where

$$\sigma_n(\eta) = \sin(\eta x) \operatorname{Re}(z_1^{-n}) - \sin[\eta(x-L)] \operatorname{Re}(z_2^{-n}); \quad n \text{ odd} \quad 21\text{-a}$$

$$\sigma_n(\eta) = \cos(\eta x) \operatorname{Im}(z_1^{-n}) - \cos[\eta(x-L)] \operatorname{Im}(z_2^{-n}); \quad n \text{ even} \quad 21\text{-b}$$

$$\xi_n(\eta) = \cos(\eta x) \operatorname{Re}(z_1^{-n}) - \cos[\eta(x-L)] \operatorname{Re}(z_2^{-n}); \quad n \text{ odd} \quad 21\text{-c}$$

$$\xi_n(\eta) = \sin(\eta y) \operatorname{Im}(z_1^{-n}) - \sin[\eta(x-L)] \operatorname{Im}(z_2^{-n}); \quad n \text{ even} \quad 21\text{-d}$$

**The behavior of  $W$  for large  $L$**

For  $L > r$  and for  $\eta$  near zero, it is found from equations 16 that

$$\operatorname{Re} W \approx \frac{\beta}{r \sin \theta} - \frac{L}{2} \eta^2 - O(L^3 \eta^4) - \dots \quad 22\text{-a}$$

$$\operatorname{Im} W \approx \alpha \eta - O(L^2 \eta^3) - \dots \quad 22\text{-b}$$

where

$$\theta = \tan^{-1} \left( \frac{y}{x} \right) \quad 23$$

$$r = (x^2 + y^2)^{\frac{1}{2}}$$

For larger values of  $\eta$ , it is found from equations 20 and 21 that

$$\operatorname{Re} W \approx \frac{1}{r \sin \theta} \left[ \frac{\sin(\eta r \cos \theta) \sin \theta}{r \eta} - \frac{\cos(\eta r \cos \theta) \sin 2\theta}{r^2 \eta^2} - 2 \frac{\sin(\eta r \cos \theta) \sin 3\theta}{r^3 \eta^3} + \dots O\left(\frac{r^2}{L^2}\right) \right] \quad 24-a$$

$$\operatorname{Im} W \approx \frac{1}{r \sin \theta} \left[ \frac{\cos(\eta r \cos \theta) \sin \theta}{r \eta} - \frac{\sin(\eta r \cos \theta) \sin 2\theta}{r^2 \eta^2} - 2 \frac{\cos(\eta r \cos \theta) \sin 3\theta}{r^3 \eta^3} + \dots O\left(\frac{r^2}{L^2}\right) \right] \quad 24-b$$

It can be seen from these equations that  $|W(\eta)|$  will have an absolute maximum at  $\eta = 0$  and will diminish as  $-L\eta^2$  for  $\eta$  near zero, and at least as rapidly as  $(r^2\eta)^{-1}$  for larger values of  $\eta$ . Thus for large  $L$  and  $L > r$ ,  $W$  may be identified as a beam function whose half width,  $\eta_w$  is dependent on  $L$  and  $r$ .

According to convention,  $\eta_w$  is the smallest real root of :

$$|W|^2 = \frac{1}{2} \max(|W|^2) \quad 25$$

Let  $\delta\phi_w$  be the beam width expressed in degrees. Then

$$\delta\phi_w = \frac{360}{\pi} (\phi(0) - \phi(\eta_w)) \quad 26$$

and

$$\cos[\phi(\eta)] = c \left( \frac{1}{v} - \frac{\eta}{\omega} \right) \quad 27$$

Thus at  $\eta = 0$

$$\cos[\phi(0)] = \frac{c}{v} \quad 28$$

while at  $\eta = \eta_w$

$$\cos[\phi(\eta_w)] = c \left( \frac{1}{v} - \frac{\eta_w}{\omega} \right) \quad 29$$

$$\text{Therefore, } \delta\phi_w = \frac{360}{\pi} \left[ \cos^{-1}\left(\frac{c}{v}\right) - \cos^{-1}\left(c \left( \frac{1}{v} - \frac{\eta_w}{\omega} \right)\right) \right] \quad 30$$

Equations 28, 29 and 30 may be used to derive approximate values for  $\delta\phi_w$ . An example of these derivations is shown in Figure 3-6. The curves shown in this figure illustrate the influence of increasing values of  $r$  and  $L$  on  $\delta\phi_w$  for a model which is appropriate for a high speed source path near a station located at the surface of a medium with a P or S wave velocity of 4.5 km/sec.

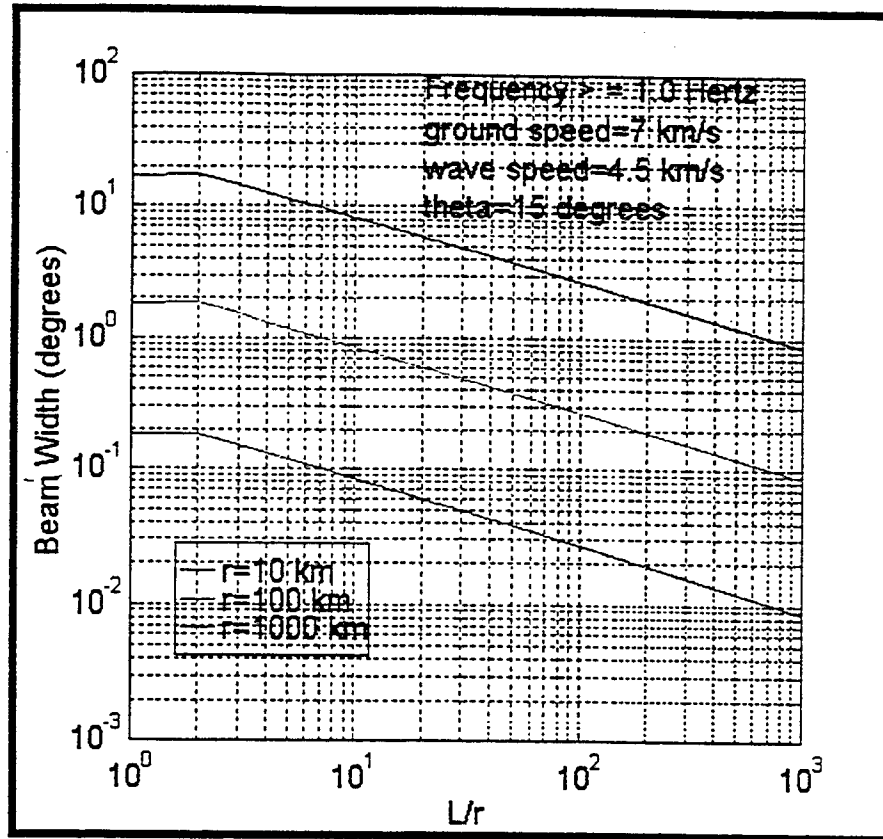


Figure 3-6. The beam width of  $W$  as function of  $r$  and  $L$ .

Notice that  $\delta\phi_w$  decreases as  $\frac{1}{r}$  for  $L < r$  and as  $\left(\frac{1}{r^2 L}\right)^{0.5}$  for  $L > r$ . It is especially significant to note that for  $r > 1000$  km.,  $\delta\phi_w$  is less than about 0.2 degree. Clearly then, for large  $r$  and  $L > r$ ,  $W$  will define a sharply tuned beam focused at  $\eta = 0$ . This behavior is illustrated in greater detail by the results shown in Figure 3-7. The upper panel of this figure portrays the modulus of  $W(\eta)$  calculated for a model with the parameters listed in the left hand side of the panel. The phase of  $W(\eta)$  is plotted in the lower panel. In order to rapidly evaluate  $W$  for a wide range of  $\eta$ , the Fast Fourier Transform (FFT) algorithm was applied equation 12 to produce the data shown in this figure. To facilitate comparisons between different wave types, the modulus has normalized by dividing by through by its maximum value. It is seen from equation 22-a that for a body wave this factor is  $\frac{\beta}{r \sin \theta}$ . As noted earlier, a spreading coefficient of 2 is appropriate for a far field body wave from a surface point source.

Observe that for this case

$$|W(\eta)| < 0.1 \max(|W(\eta)|); \quad |\eta| \geq 0.005$$

which indicates that it is a very sharply tuned beam function.

### Example of $W$ for a Surface Wave Input

The beam function for a far field surface wave from a surface point source is shown in Figure 3-8. It was generated by changing the spreading coefficient,  $q$ , from 2 to 0.5 and reapplying the FFT algorithm to equation 3, using the same model parameters.

Notice that the width of the modulus of the surface wave beam function is significantly smaller than the body wave beam width. This reflects the fact that surface wave geometrical spreading is substantially less severe than body wave geometrical spreading.

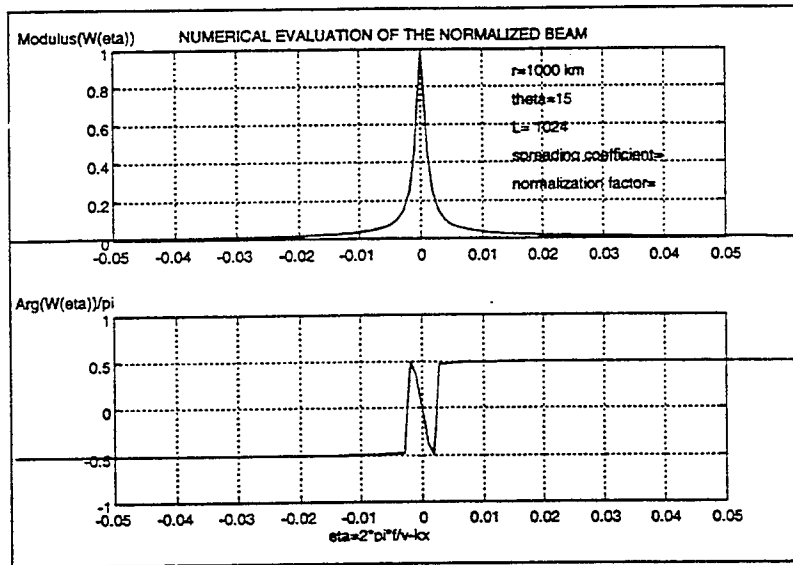


Figure 3-7. An example of the Beam Function for body waves generated by a moving surface point pressure load.

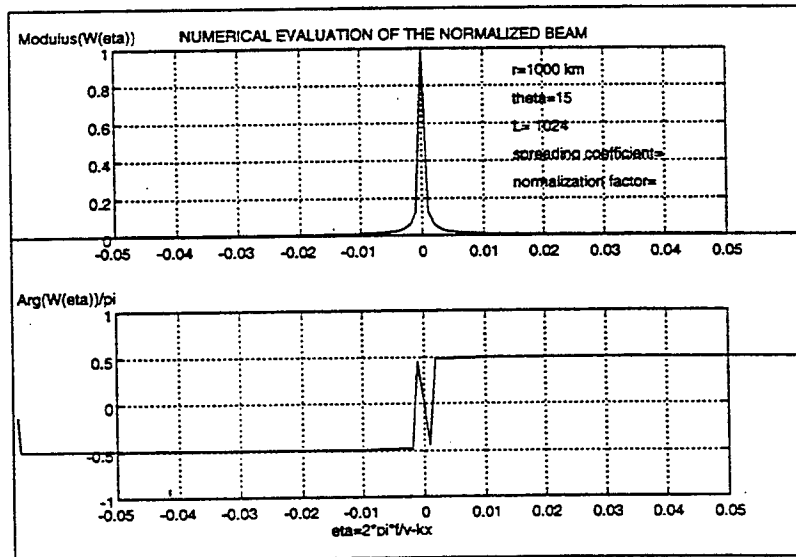


Figure 3-8. An example of the Beam Function for surface waves generated by a moving surface point pressure load.

### An Approximate Expression for $H$ for Body Wave Inputs

Based upon the evidence and arguments presented previously, it may be concluded that for large  $r$  and  $L > r$ , both body and surface wave beam functions may be approximated by functions of the form;

$$W(\eta) = B(x, y; L, q) \quad \eta \equiv 0 \quad 32$$

$$\approx 0 \quad \eta \neq 0$$

where in each case  $B$  is the value of  $|W|$  at  $\eta=0$ . From equations 23, it can be seen that for body waves,  $B$  is given by

$$B = \frac{\tan^{-1}\left(\frac{L-x}{y}\right) - \tan^{-1}\left(\frac{-x}{y}\right)}{y} \quad 33$$

Consequently, substitution of equations 32 and 33 into equation 4 and performing the indicated convolution results in the following expression for  $U$  created by body waves

$$H \approx \frac{\tan^{-1}\left(\frac{L-x}{y}\right) - \tan^{-1}\left(\frac{-x}{y}\right)}{y} CP(\omega) \exp(-i\omega t) \exp\left[i\frac{\omega}{c}\left(\frac{c}{v}\right)x\right] \exp\left[\pm i\frac{\omega}{c}\sqrt{\left(1-\frac{c^2}{v^2}\right)}y\right] \quad 34$$

Equation 34 exhibits the essential properties of the seismic "bow wave" generated by a moving pressure load. Observe that if  $v \geq c$  the radical in equation 34 is real and  $H$  becomes a plane wave which propagates at speed  $c$  in the direction

$$\phi = \cos^{-1}\left(\frac{c}{v}\right) \quad 35$$

On the other hand, if  $v < c$ , the radical in equation 34 is a pure imaginary and  $H$  becomes a disturbance which propagates at the speed of, and on the path of the moving load but decays exponentially in a direction normal to the path.

The evolution of  $H$  as  $L$  increases is illustrated by the relative amplitude profiles shown in Figure 3-9-a. The relative amplitude,  $A$ , of  $H$  is defined as

$$A = \frac{|H|}{\frac{C|P(\omega)|}{r^2}} \quad 36$$

which is seen to be the ratio of the amplitude of  $H$  to the amplitude of a far field body wave generated by the point pressure load at the origin. The profiles were calculated along a line parallel to the load path but offset 100 km in order to approximate far field conditions. Notice that for distances along the profile which are much greater than the path length, the amplitude of  $H$  scales as the amplitude of a point source body wave of strength  $L$ ; whereas for distances comparable to or less than the path length the amplitude of  $H$  differs significantly from that of a point source body wave particularly for large  $L$ . The two dimensional behavior of the relative amplitude of  $H$  for large  $L$  was also studied. The data in this case were calculated for the case where  $L = 1000$  km. Inside the region,  $r < L$ , the relative amplitude of  $H$  reaches a maximum of about 85 dB for  $x$  near  $L$  and  $y = 100$  km., then approaches 0 dB as  $x$  and  $y$  approach zero.

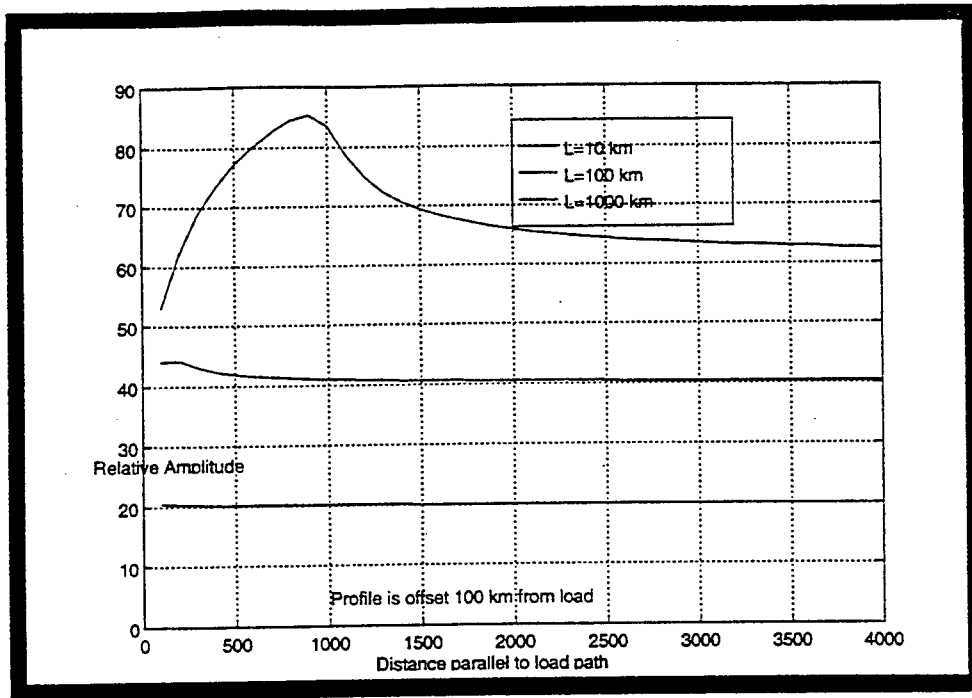


Figure 3-9. Relative amplitudes of H. Relative amplitude profiles of U taken parallel to the load path at an offset distance of 100 km.

Finally, by letting

$$v = x - L \tag{37}$$

and recognizing that

$$L = vt \tag{38}$$

equation 34 may be rewritten as

$$U = \frac{\tan^{-1}\left(\frac{-v}{y}\right) - \tan^{-1}\left(\frac{-v - vt}{y}\right)}{y} CP(\omega) \exp\left[i \frac{\omega}{c} \left(\frac{c}{v}\right) \xi\right] \exp\left[i \frac{\omega}{c} \sqrt{\left(1 - \frac{c^2}{v^2}\right)} y\right] \tag{39}$$

which for large values of  $t$  reduces to

$$U = \frac{\tan^{-1}\left(\frac{-v}{y}\right) + \frac{\pi}{2}}{y} CP(\omega) \exp\left[i \frac{\omega}{c} \left(\frac{c}{v}\right) v\right] \exp\left[i \frac{\omega}{c} \sqrt{\left(1 - \frac{c^2}{v^2}\right)} y\right] \tag{40}$$

Equation 40 demonstrates that for large values of  $L$  and as seen in a reference system fixed to the moving load,  $H$  is essentially independent of time.

It may be concluded from this analysis that relatively weak pressure sources will create signals that are detectable at stations which are located at within a few hundred kilometers of the load path when the length of the path is of the order of 1000 km and  $v \geq c$ .

## **APPENDIX 4. Preliminary Tests of Alternative Infrasonic Sensor Designs**

### **Introduction**

As a result of the Comprehensive Test Ban Treaty (CTBT), there is a renewed interest in detecting and recording infrasonic phenomena. Up to now, only a few research and volcano observatories have maintained infrasound sensors and data collection facilities. These existing stations have not generally recorded high dynamic range (118 dB), broadband (0.02-16 Hz) signals. Experimental infrasound arrays have been deployed, but these do not always have the CTBT recommended 1-2 km aperture.

Current operational systems use one of two types of microbarographs, the absolute pressure device (Figure 1) and the differential pressure microbarograph (Figure 2) used at Lajitas, Texas (TXAR), and Warramunga, Australia (WRA). Each has advantages. The differential microbarograph is easy to assemble from off-the-shelf commercial products, making it inexpensive; measures only the band of interest, making it suitable for low dynamic range recorders; is capable of a bandwidths that include audio, allowing overlap calibration with microphones; and is reasonably linear over wide variations in atmospheric pressure, minimizing the need to record atmospheric pressure. The absolute microbarograph is much less sensitive to ambient temperature and temperature gradients, allowing it to be used in shallow vaults; delivers state-of-health atmospheric barometric pressure as part of the data; and is simpler to describe, giving a simplified theoretical response.

Work at SMU has concentrated exclusively on differential sensors because they are reasonably priced, are physically compact, and are compatible with existing seismic digitizers. The microbarographs operating at TXAR were assembled for nominal material cost using simple tools. The compact assembled system is reasonably rugged and fits inside the 8 in. borehole above the seismometer. Since the electronics and interface are plug compatible with existing seismic digitizers, a seismic array may be easily upgraded to a seismo-acoustic array by replacing a single component digitizer with a two channel digitizer.

### **Previous Work**

Specific work in practical infrasonic instrumentation design is sparse. Original theoretical work by Benade (1968), Burrige (1971), Cook and Bedard (1971), Daniels (1950 and 1959) describe the basic physics involved in microbarograph responses and the

responses of the associated noise reducing pipe arrays. The work by Haak and Wilde (1996) is an unusually complete summary of the physics for microbarograph design.

Like much of the infrasound community, SMU has used porous garden soaker hoses in noise reducing pipe arrays as an inexpensive alternative to the more elaborate Daniel's line microphone. A previous study at SMU, (Hayward, 1996) considered the characteristics of the sensors and hoses currently deployed at TXAR and discussed the response variability and resonance peaks as a function of differing hoses (all of the same manufacture). The study also considered several methods for characterizing the response of a porous hose. For example, responses of two identical hoses laid outdoors parallel to each other 7 cm apart was incoherent over much of the spectrum. A differential sensor was used to measure the pressure gradient along the hose and this was compared against the readings from a differential microbarograph. The two relation between the two signals was complex and unexplained. Finally, sensor noise levels and responses measured for three microbarographs subsequently deployed at TXAR suggested that noise levels for the sensors could vary widely. Resolving these problems was postponed until the characteristics of the equipment and processes were understood.

Since the initial experiments with sensors at SMU, Haak and Wilde (1996) reviewed the physics involved in porous hose design and suggested alternative designs such as those based on a closed compliant tube, and McLaughlin (1997) analyzed various porous hose effects based on simple laboratory measurements and the results from a finite difference modeling program.

### ***Current Sensor Design***

The microbarograph currently used at TXAR (Figure 3) is based on Reinke's (1985) design which in turn was based on the early work of Stachura, Siskind, and Engeler (1981) utilizing differential pressure gauges to measure blasting overpressures. A short section of iron pipe forms the backing volume. Instead of a capillary tube as a bleed resistance, a variable needle valve is used to set the low frequency corner of 1/60 Hz. The valve is adjusted in the lab and then locked into place with a small dab of glue. A standard garden hose connector at the top allows connection to the pipe array. At TXAR, the sensors are placed about 2 m below the surface for security and temperature stability.

The pressure sensor is the Validyne P305D sensor, a differential pressure gauge with a range of  $\pm 0.125$  PSI ( $\pm 850$  Pa) and a  $\pm 5$  Volt output. Higher pressure ranges are available, but this would limit the use for small signals. Careful handling during installation

is required to avoid exceeding the rated pressure of  $\pm 3$  inches water. While overpressures generally do no permanent harm, they can disturb the calibration.

The sensor itself is a variable reluctance device. Two coils are positioned on either side of a magnetically permeable stainless steel diaphragm. Small changes in the diaphragm position cause a change in the inductance of the sensor coils, an increase on one side and a decrease on the opposite side. There are a number of methods to convert this impedance change to an analog signal. Most techniques incorporate the two sensor coils into an AC bridge balanced at zero pressure. The P305 electronics uses an internal 5.2 KHz  $\pm 5$  Volt square wave excitation and produces an output with less than -70 dBV (0.05 Pa equivalent) noise at the half the primary excitation frequency (2600 Hz). Antialias filtering in the digitizer removes the remnants. The gauges produces a  $\pm 5$  Volt single ended signal referenced to the negative supply bandlimited from DC to 200 Hz from an unfiltered primary 12 Volt power supply. Sensor output is digitized at 40 SPS on a 24-bit Science Horizons digitizer with a 2  $\mu$ V (0.00035 Pa) LSB.

The construction and plumbing in the current TXAR design was based on conservative modification and quick fabrication of Reinke's design rather than by extensive calculation and testing. It resulted in a system that possessed a number of unknowns and idiosyncrasies. In spite of this, for the past two years TXAR has produced highly relevant infrasonic data leading to significant advances in the understanding of infrasonic processes above 1/2 Hz.

### ***Problems with Current System at TXAR***

The microbarograph design can be divided into three logical subsystems, the sensor and associated signal processing electronics, the backing volume and associated plumbing required to create a low cut filter (the microbarograph itself), and the noise reducing pipe array. While all of these components contribute to the total system response, most obvious problems in the current design can be attributed to one subcomponent.

#### ***Sensor***

There are four problems with the Validyne P305 sensor; high self noise, DC drifts, single ended outputs, and a strong sensitivity to RF interference. None of these preclude the use of the sensor, but all have to be considered and handled during testing and installation.

During the initial noise tests, one sensor was found to have a noise floor 14 dB higher than the quietest. At the time, this was attributed to a noisy set of electronics, and it was felt that it might be necessary to select units prior to deployment. The noisy unit was subsequently retained as a laboratory test unit. The manufacture's specifications suggested only a RMS noise floor  $\leq 5$  mV (equivalent to 0.86 Pa). Measured noise in the band of interest (0.02-20 Hz) was far below this.

Sensor output is relative to the negative power supply. In the current AIM systems, the primary power supply is completely isolated from signal paths by DC-DC converters. When a Validyne sensor is installed in the system though, the negative primary supply must be tied to negative signal output. This results in a signal path back through the power supply that can introduce noise into the system.

When small amounts of modulated RF energy above 100 MHz are present in the cable connecting the Validyne electronics, the output may be excessively noisy. This was noted at TXAR for sites using packetized RF telemetry. The effect does not seem to be consistent. The digitizer front ends also are susceptible making it difficult to isolate the problem. In the field, the RF interference is minimized by moving antennas away from the electronics, shielding the borehole, and nulling the local field by adjusting cable positions.

DC offset varies with ambient temperature partly from offsets in the electronics and partly due to minor changes in the diaphragm position as the sensor block is subjected to differing temperature gradients. Offset also varies with sensor orientation, since gravity affects diaphragm position. This DC offset may be set to zero with an internal adjustment; however, in outdoor field experiments with the sensor on the surface, it was not possible to keep the offset within 62 mV over a several hour period. This offset is a problem for 16-bit digitizers, which have a maximum input of 62 mV ( $32767 * 2$  uV) when the sensitivity is low enough to detect small signals. For laboratory and field testing, sensors were adjusted for zero offset and tests were kept brief. When installed at TXAR, the systems were connected to 24-bit digitizers.

### *Microbarograph*

Problems with the microbarograph are divided into three groups; unknown characteristics, practical problems, and technical problems with the response. Characteristics such as impedance, thermal constants, backing chamber volume and fore volume, are unknown. Practical problems include the fragile nature of the finished product, the tendency of the adjustable needle valve to get bumped, and a difficulty in

keeping critical areas of the plumbing clear of dirt and moisture. There are three specific technical problems with the response; the construction results in a high-cut acoustic filter at about 5 Hz (although it varies slightly from unit to unit), units in the field drift from the laboratory setting and eventually have wildly different responses, and there is no way to remotely calibrate the unit.

It is essential to keep the plumbing clean and dry. Once assembled, but prior to connecting the sensor, the plumbing is washed with a degreasing cleaner to eliminate all traces of grease and dirt. Joints are sealed with Teflon tape. On repeated assembly and disassembly small pieces of tape have a tendency to collect inside fittings.

The needle valve, used to adjust the response, is particularly troublesome. As delivered, the spring loaded needle is greased at several points. In order to obtain the proper response the valve had to be nearly closed. The resulting orifice is inconsistent. Grease in the spring assembly caused valve creep over periods of minutes and hours. It is essential to completely disassemble the needle valve and thoroughly degrease the components. Still, valves set correctly in the morning can creep completely closed by the evening. Mechanical backlash in the system requires that the adjustments be made from one direction (open to closed).

Once the valve is properly set, the control is cemented in place. This did not always result in a fixed setting. Moderate blows to the assembly or large temperature changes sometimes resulted in a significant change in the response

Laboratory tests demonstrated that the system has an unplanned 5 Hz low pass acoustic filter. This was demonstrated by comparing the response of a plumbed system with a sensor running as a simple microphone (using a closed backing volume) to noise generated by a high pressure air jet. Although few infrasonic signals of interest have significant energy above 5 Hz and the addition of noise reducing pipes will further attenuate these higher frequencies, this additional filter term complicates the system response.

To a first order the response of the microbarograph is a simple 1 pole RC filter. It was intended that the corner be at 1/60 Hz. Observation of field data suggests that two of the sensors now have corners at far longer periods. Initially this appeared as a slow drift towards longer frequencies. It is unknown if the present position is stable.

Sensors have never been calibrated for sensitivity other than the initial factory calibration. Factory calibration of  $\pm 0.25\%$  is sufficient given the uncertainties in the system response, provided no damage or overpressure has occurred. Overpressures of as little as

10 times (18 KPa) may change the sensitivity by 2%. Pressures of 100 times (180 KPa) may make a 4% change. A more critical problem is dirt or moisture in the diaphragm chamber which may result in sensitivity changes of 100% or more. Being able to remotely calibrate sensors would significantly increase the confidence in the response and sensitivity.

The acoustic and physical characteristics of the plumbing are unknown and dimensions that could be used to estimate these are unknown and uncontrolled. While simple experiments were done to measure the sensor noise characteristics and dynamic response of the system to large signals, more specific measurements, such as acoustic impedances, thermal capacity, or internal resonances were undetermined. Without these, designing a matching feed line for a pipe array is difficult.

### *Pipe Array*

The pipe array at TXAR consists of five or six<sup>1</sup> 5/8 in. by 50 ft., porous garden hoses connected to 25 ft. of 5/8 in. hard wall garden hose in turn connected to a manifold with a volume of roughly 2 liters. A 25 ft. hard wall garden hose connects the manifold to the microbarograph hanging 2m. below the surface in an 8 in. cased borehole shared with a seismometer. Like the microbarograph, the pipe array was constructed with easily obtained local material and deployed quickly. Based on initial tests on the SMU campus and observations of data collected at TXAR, the array has the following problems: strong variable hose resonances, incoherence on adjacent hoses, and leaks of end points. In addition the hose state-of-health, acoustic characteristics, spatial and frequency response, and aging characteristics are unknown.

At TXAR sites, pipe arrays appear to have unique resonances, although all sites use the same array design. The origin resonances have not been investigated.

Hose connection points often have substantial air leaks as the result of a poorly seated washer or an incomplete crimp on the connector ferrule. Some leaks were equivalent to the contribution of 50 ft. of hose. Leaks were located by observing the signal from a low pressure air jet as it was moved along the hose and connector. Loose connections were reseated and tightened while leaky ferrules were taped.

Soaker hoses at TXAR are subject to intense sunlight, dust, and occasional investigation by javalena (wild pigs) in the area. In addition aggressive vegetation and insects are risks. Because the acoustic resistance of the pipe array is significant, a single

---

<sup>1</sup> One site uses six hoses, the other three use five hoses.

cut or tear in any hose will result in a change in the frequency response and a significant reduction in the spatial filtering.

Unfortunately, it is nearly impossible to monitor the state of the hose array from observing the data itself. If there were archived background responses during no wind conditions, it might be possible to recognize a change in the spectra that would indicate a cut or break in the hose, but wind conditions are not recorded nor has noise spectra been routinely collected. Examining the hoses on a routine maintenance visit could locate obvious tears and breaks, but could also miss small punctures and would require significant time. It would probably be more economical to simply replace hoses—if one could be assured the acoustic response of the system would be the same.

Experiments by Haak and Wilde (1996) and McLaughlin (1997) have confirmed that acoustic characteristics of soaker hoses change substantially as a result of aging and moisture in exposed hoses. This would affect both the frequency and spatial response of a system. Haak and Wilde (1996) suggested that hoses be protected from moisture and dirt by elevating them from the ground and adding a roof. This though has the disadvantage of moving them farther from the ground boundary layer.

## **Purpose**

The purpose of this paper is to document an improved microbarograph design, to discuss the initial laboratory experiments using the new design and to suggest methods for field calibration and state-of-health monitoring.

The improved design involves different plumbing of the same P305D sensor, and an initial consideration of two alternative sensors, one with an enhanced sensitivity (up to 30 times) and one with a lower price (about 1/5).

This is intended as a starting point for further modifications, for comparing alternative sensors, for measuring the acoustic and electrical characteristics of the system, and for comparing the measured responses with theoretical responses.

Three simple calibrators for remote field calibration and state-of-health monitoring are suggested and demonstrated on the prototype system.

## Results

### *Microbarograph Design*

The design goals were to increase the backing volume to 1 liter; to replace the variable needle valve with either a fixed orifice or capillary tube; to allow some form of field calibration; to increase the high frequency cutoff of the system beyond the digitizer cutoff of 20 Hz; to increase the thermal mass such that the sensor is less sensitive to small temperature changes; to keep the system small enough to fit within the existing boreholes at TXAR (8" internal diameter with sufficient room to clear existing cables); and to keep the design flexible and inexpensive such that changes could be made during tests. Like the TXAR design, this improvement uses the Validyne P305D sensor.

The design is based on 4 in. schedule 40 PVC tubing (Figures 4, 5, 6, and 7). PVC prototypes may be quickly constructed, are inexpensive, and provide a significant thermal insulation between the outside and inside air temperatures. The inside of 4 in. PVC end caps have been reamed slightly to close each end of a tube with a slip fit. O-rings in machined grooves on the body of the instrument ensure air tight seals. The end caps are fitted inside 5.5 in. pipe to form support for the electronics, and to form a flat base for the bottom. A small ring around the outside in the middle of the tube is used to support the device in an arbor press for assembly and disassembly. Two test ports to in the fore and backing volumes are closed with short lengths of stoppered Tygon tubing when not used for testing. A divider in the center, machined from 4 in. PVC rods stock, separates the fore and backing volumes.

In order to keep the sensor at a constant ambient temperature and maintain short plumbing connections (for good high frequency response), the diaphragm assembly was separated from its electronics and mounted inside the fore volume on a short length of brass tubing. To prevent dirt and moisture from accumulating in the sensor the fore volume side of the sensor is protected with a short right angle connector. Wires from the sensor penetrate the top cap through a 1/8 in. pipe fitting filled with a sealing compound. Once the sensor is in place, the top is filled with 5 stainless steel scrubbing pads to increase the thermal capacity, reduce internal temperature gradients, and reduce internal resonances.

The backing volume contains only the capillary tube. Roughly 27 in. of 0.03 in. capillary tube slips inside a short piece of 1/16 in. Tygon so that the capillary may be connected to the internal fore volume port. Once the capillary is in place the backing volume is also loaded with 5 stainless steel scrub pads.

The bottom end cap is fitted with a standard male garden hose connector. This is left open as the device is assembled to prevent the backing volume from being overpressured and damaging the diaphragm. It is then closed with a solid cap.

The top end cap is more complex. It contains the wire feed through for the diaphragm (4 wires), a flexible hose to connect to the input garden hose, a plumbing connector for calibration input to the fore volume, the impulse pump calibrator, and the P305 electronics. The impulse pump is normally connected to fore volume, but may alternately be connected to any of the four connectors along the side of the instrument to allow impulse testing of the backing volume only or combined testing of the fore and backing volume.

Such a system is expected to operate in boreholes at least 2 m below the surface. During tests in the lab, the system was placed in a Styrofoam box internally lined with thin aluminum plates and then filled with Styrofoam packing peanuts (Figure 8).

During the initial qualitative tests, it was found that the microbarograph was sensitive to small vibrations as a result of flexing in the connector hose at the top of the assembly. Running the system on a pier eliminated visible seismic response. When the microbarograph was closed and the brass hose connection exposed to the ambient air, it behaved as a gas thermometer, registering the small changes in temperature due to the cycling building air conditioning. This was eliminated by insulating the fittings with several layers of bubble wrap.

### ***Calibrator Design***

The calibrator design had four goals. First, the calibrator had to be remotely activated, ideally by using simple modifications to the existing calibrator electronics in the digitizer. Second, it must produce a signal of sufficient bandwidth to demonstrate that the dynamic response of the system is unchanged. Third, it should be able to vary the amplitude for varying noise conditions. Fourth, it should calibrate as much of the system as practical. In this regard a diaphragm activator is less desirable than a calibrator that produces a pulse in the backing volume. A calibrator which produces a signal in the hoses is even better. A calibrator which could produce a known plane wave in ambient air would be ideal.

Three different calibrators were examined: a modified bellows calibrator from an old NBS microbarograph system, a metering pump used as a step generator, and a

headphone element from a Koss high-velocity open style headphone. Each of these has specific advantages and ranges where they proved useful.

### *Bellows calibrator*

The bellows calibrator (Figure 9) produces a small volume change from a DC gear driven motor. The original calibrator produced a 1/3 Hz signal when driven from 12 Volts, close to the high frequency end of the original NBS microbarograph. The motor was replaced with a 1 RPM unit to produce a constant displacement calibrator that could operate near the desired low frequency corner of the microbarograph. The calibrator is capable of operating at periods down to 5 minutes at reduced voltages. Even longer periods are possible if the motor is operated in pulsed mode. Because the fore and backing volume is only 1 liter, the pump must either be connected with short tubing, or the volume of the connecting tubing must be included in the calculation.

### *Impulse calibrator*

A surplus impulse metering pump was configured as a step function calibrator. On each 24 Volt impulse, a piston moves a specific amount (adjustable over a small range during installation), producing a known change in volume. While designed to work with liquids, a film of light oil allowed the pump to be used with air. The impulse rise time is fast, in excess of 0.05 seconds as observed by the Gibb's effect in the impulse data. The displacement may be adjusted from roughly 0.025 cm<sup>3</sup> to 0.250 cm<sup>3</sup>. No leaks were observed even after repeated cycling, allowing the pump to be permanently connected and plumbed. The pump may be cycled at 4 Hz to produce a large pressure pulse on systems which have a long period response of many seconds.

There are several disadvantages. The pump is surplus and exact off-the-shelf replacements may not be readily available. It requires a 24 Volt supply to work reliably at all stroke volumes requiring either a separate power supply or limiting displacements to only the smaller volume. During trigger-release cycles the coil produces a strong back EMF that couples into the signal line as a spike. Finally when operated at 24 Volts, the piston produces a strong vibration that becomes part of the diaphragm signal.

### *Headphone element*

A high velocity headphone element from a Koss open style headphone was used as the driver for a calibrator built from plastic plumbing (Figure 10). The front of the headphone element was cemented to a reducing string and caulked to assure an air tight fit.

The backing volume was packed with foam rubber. A small compensation bleed tube connects the backing volume to the fore volume through a calibrated orifice (0.003 in.). During use, the element is driven from a signal generator or noise generator to produce high to mid frequency drive signals (1/10 Hz to 200 Hz).

The small closed backing volume produces nearly constant displacement with voltage signal, since the spring compliance of the headphone diaphragm is dominated by the compliance of the air in the backing volume. The small backing volume results in a resonant frequency above 500 Hz in contrast to the less than 100 Hz free air resonance. Coupling the system to a 1 liter input does not change the resonant frequency significantly, indicating that the impedance of the system is controlled by the calibrator backing volume and bleed system rather than the input impedance of the microbarograph. Of course driving a lower impedance system would result in loading of the calibrator.

Drive signals with periods as low as 100 second square waves were used to confirm that the calibrator produced a nearly constant displacement output. Unfortunately we found that the residual solvent in the PVC pipe cement would in time attack the diaphragm resulting in small holes and perforations. While the system could produce strong enough signals to calibrate the microbarograph itself, it did not produce sufficient drive to calibrate long sections of porous hose at low frequencies.

### ***Microbarograph Noise Tests***

Microbarograph noise, noise other than that related to a pressure change at the inlet of the microbarograph, is the result of electrical noise, varying magnetic fields, vibration and tilts, temperature strains within the sensor, temperature strains within the microbarograph housing, convection cells within the fore and backing volumes, and mechanical compliances within the system. In the current design, electrical noise includes sensor electronics noise and two additional sources; the single ended input which introduces primary power supply noise into the digitizer, and insufficient RFI protection in the sensor power supply circuits. At some installations, the electrical noise dominates all other noise sources. Varying magnetic fields displace the diaphragm and change the inductance of the sensor coils. Although the diaphragm is reasonably stiff, it will act as an accelerometer and vibrations and tilts appear as small signals. Vertical vibration sensitivity is minimized by orientating the plane of the diaphragm vertically, but this maximizes the sensitivity to small tilts and rocking.

Although the sensor is constructed of a single material to minimize temperature stresses, temperature gradients across the sensor block due to ambient gradients and heat

dissipated by the sensor electronics also introduce stresses. Fortunately the block's large thermal mass makes this only a significant noise source at low frequencies. The largest potential noise source is caused by temperature changes and gradients within the microbarograph backing volume. A change of less than 0.0003°C will produce an equivalent input signal of 0.1 Pa. Dissipation in any electronics within the backing or fore volume increases this noise. Assuming that the thermal mass of the system is 500 gm H<sub>2</sub>O equivalent, it would require about 1 mW to raise the temperature 0.00003 °C in 1 minute. Since the electronics dissipate 96 mW, it is essential to locate them outside the fore or backing volumes..

Changes in the backing volume dimension, as the result of creep, stress or vibration create noise as the effective volume changes. The dimension change required to produce a 0.1 Pa signal may be calculated using the gas relation:

$$\Delta V = \frac{\Delta PV}{\Delta P + P}$$

where P and V are the base pressure and volume, ΔP is the change in pressure, and ΔV is the change in volume. A volume change of 10<sup>-6</sup> cm<sup>3</sup> or an elongation of 1.2x10<sup>-8</sup> cm ( a strain of 10<sup>-9</sup>) assuming no change in diameter would create a 0.1 Pa signal in a 1 liter backing volume. Schedule 40 PVC is sufficiently stiff that low amplitude seismic signals are not a problem as verified by loading the microbarograph with a 1 kg weight (equivalent to a 0.1 g signal) and observing the lack of a resulting signal.. For larger seismic signals volume changes will be dominated by flexing of the more flexible horizontal hoses and pipes rather than the hard PVC material.

Three methods of measuring the sensor self noise were considered.

First, the sensor may be isolated from the input pressure changes. For a seismometer this is done by blocking the mass; for a microphone it is done by isolation in an anechoic chamber; for the microbarograph, the backing volume capillary and fore volume inlets are plugged. In the case of a seismometer this technique overestimates the noise since it is impossible to completely lock the mass and laboratories are notorious for high seismic noise. In the case of a microbarograph, high background pressure noise is not a severe problem. First, while for seismometers ambient seismic noise is considered signal, but for a microbarograph ambient background noise coupled through the instrument is noise. In contrast to the seismometer, the microbarograph itself is supposed to have no response to pressure changes, all signals are introduced through the pipe array. Second, the dynamic range for seismic signals is higher than that for microbarograph signals. The

advantage of an isolation technique is that it requires only one sensor, is quick, and gives a reasonable qualitative result. To the extent that laboratory noise couples through the closed instrument, the technique will overestimate self noise.

The second method substitutes a dummy input for the sensor. For a passive electromagnetic velocity seismometer, a resistor is typically substituted for the main coil. For the Validyne, a matched set of resistors, a center tapped transformer, or matched inductors could be substituted for the sensor. Alternatively a high pressure diaphragm could be substituted for the ultra-low pressure diaphragm. Since the technique estimates the electronics noise only, it underestimates the total system noise, but verifies that the electronic noise is below the system noise requirement and that stray RFI or EMI noise is not significant.

The final method is the signal coherence method which measures system noise during signal conditions. Its primary disadvantage is that it requires two matched systems. In a prior experiment, analysis of sensor coherence determined that self noise at 1/50 Hz was 20 dB above that at 1/10 Hz. Since only one system was available in this study, it was thus impossible to measure coherence.

### *Noise Tests Results*

Four simple tests were made to estimate the background noise inherent in the sensors and associated electronics (Figure 11). The microbarograph was wrapped in bubble wrap, placed in an insulated box on an isolated pier and allowed to temperature stabilize for 3 hours during the late evening. The sensor was connected to a 24-bit recorder with the sensor and digitizer power supplied from a common 12 Volt 100 amp/hour battery. Data was radio telemetered to a workstation one floor above and analyzed in Matlab.

The first test (Figure 11-dummy load) substituted  $500\Omega$  resistors for the nominal 20 mh sensor coils. The two resistors were glued in contact, insulated by wrapping them in Styrofoam peanuts, and connected in place of the sensor coils. Data was collected at 40 Hz for 12 hours. The result produced a wideband RMS noise of 0.006 Pa or an equivalent 35 uV RMS noise. Small DC biases added to either resistor result in bridge imbalance and can create a signal.

The second test (Figure 11-closed no bleed) recorded data with both the input and bleed plugged resulting in a system of two volumes connected by a diaphragm. At frequencies below 0.03 Hz, the noise level rises as a result of low frequency thermal

coupling or a pinhole bleed around the wire feed through. In later tests we found problems in the seals of wire feed-through.

The third test (Figure 11-closed system) recorded a sealed input port but connected the backing and fore volumes with a 0.003 in. bleed orifice to produce a high pass acoustic filter at 1/60 Hz. If the fore volume were open or connected to a low impedance source this orifice would result in a high pass of 1/120 Hz.

The fourth test (Figure 11-HF closed system) is a repeat of the previous test, but with a 320 Hz sample rate. The spike at 60 Hz is probably a result of electrical noise rather than magnetic coupling.

All of the three tests show similar results; a noise decay below 0.3 Hz proportional to 1/frequency and above the dummy load electrical noise. The RMS noise from 1/60 Hz to 20 Hz is 0.015 Pa with most of the noise concentrated in the low end of the spectrum. This is equivalent to 88 uV RMS noise, far below manufacturer's specified 5000 uV. This means that sensor noise level will need to be routinely verified for any new sensors, since a manufacturing change could substantially increase noise levels but still meet the advertised specification.

### *Volume and thermal measurements*

In order to measure the effective fore and backing volumes, all test ports were sealed and the bleed between the two volumes was plugged. A syringe was then used to inject 2 cc of air into one of the test ports of the closed fore and backing volume. Each injection was repeated three times (Figure 12). The temperature gradient between the fore and backing volumes changed during the experiment, resulting in a background linear trend. The overshoot<sup>2</sup> represents the shift from adiabatic to isothermal response. Exponential decays (Figure 13) were fit to the detrended pulses. This is the classical experiment of Clement and Desmores to measure the ratio of  $C_p/C_v$ , the ratio of the heat capacity at constant volume to the heat capacity at constant pressure. The calculated median fore and backing volumes were 1.07 and 1.16 liters respectively. Gamma ( $C_p/C_v$ ) for the fore and backing volume was only about 1.03 and the low cut corner frequency 0.48 Hz for the fore volume and 0.29 Hz for the backing volume. The low gamma, less than 5% overshoot, is due to the small volume and the stainless steel packing. This small gamma means that the effect of the adiabatic to isothermal transition can be ignored in computing instrument response.

---

<sup>2</sup> The overshoot is not related to the rubber connectors or give in the syringe since it could not be produced by squeezing a fully depressed syringe.

## ***Calibrator Demonstrations***

Each of the three calibrators was demonstrated by performing one or more simple measurements. The purpose was not to exhaustively test the calibrators but rather to demonstrate their effectiveness and deficiencies.

### ***Impulse Calibrator***

The impulse calibrator was connected between the fore and backing volume and adjusted to produce a 3 Pa pulse. Tests in four configurations were made.

The first test, where all ports and bleeds were plugged, verified that the connections to the impulse pump produced no new leaks and estimated the volume produced by each impulse (Figure 14). Again, the trend produced by the changing temperature gradient had to be removed. The pump displacement was set to the maximum that would operate reliably at 12 Volts (the rated drive is 24 Volts). Based on the backing volume calculated with the syringe, the impulse pump produced a volume change of roughly 1.7 mm<sup>3</sup>. The overshoot associated with the impulse is composed of three components: a small contribution due to the gamma of the system; the seismic shock as the piston hits the stop; and the electrical and magnetic coupling during the rise and fall of the solenoid impulse current.

The following tests fit simple one pole responses to the recorded impulse response using Prony's method. For cases where the fore volume was open to the laboratory, multiple impulses were used to create large enough signal that could be reliably fit (Figure 15).

In test two, the fore volume was closed. The pump was connected between the fore and backing volume. A set of two 0.007 in. and one 0.003 in. orifices were connected in series as the bleed resistance between the two volumes. When the fore volume is closed, the reponse will be related to the equivalent volume given by:

$$\frac{1}{\frac{1}{V_{fore}} + \frac{1}{V_{back}}}$$

Since fore and backing volume are about the same, this should result in a period about half of that of a measurement that leave the fore volume open (as was done in tests three and four). In test three (open fore volume) the same set of orifices were used in the bleed resistance, but the fore volume was unplugged and allowed to vent to laboratory air

through a 1 foot long 5/8 in. garden hose. The final test repeated test three, but replaced the 0.003 in. orifice with a 0.03 in. by 27 in. Teflon capillary tube.

Normalized responses (Figure 16) were determined and the mean and standard deviation calculated for each of the impulses. On the semilog plots, theoretical exponential response should plot as a straight line. Deviations are the result of noise, such as opening and closing doors or elevators running during tests.

For the closed fore volume with the orifices, the mean period was 56.6 seconds; for the open fore volume, 134.2 seconds; for the case with the capillary, 57.6 seconds. For the final case with the capillary, two standard deviations span periods from 51 to 66 seconds. This dispersion could be reduced by increasing the pulse amplitude or selecting pulses with no interfering noise.

### *Electromagnetic Calibrator*

An electromagnetic calibrator using a headphone drive element in plastic plumbing (Figure 17) was envisioned as a method to make high frequency and broadband calibrations, for example to determine the response of the instrument up to 120 Hz.

The calibrator resonance was determined by observing the frequency where the drive current was minimum. When operating in free air with the backing volume sealed, the resonance was 550 Hz. Attaching the calibrator to the input of the microbarograph did not change the resonance point appreciably. The calibrator transfer function was qualitatively measured by comparing the drive signal to the acoustic signal recorded with a laboratory B&K model 4165 microphone sealed into the front cavity. This produced a response that was almost flat from 2 Hz-200 Hz. Frequencies below 2 Hz, the low frequency corner for the microphone, were not examined.

The calibrator was sealed to the microbarograph (Figure 17) and driven with a 14 second period square wave at  $\pm 1.5$  Volts,  $\pm 0.47$  Volts, and  $\pm 0.15$  Volts peak-to-peak. This was done once with the calibrator backing volume open and once closed (Figure 18). With the calibrator backing open, there is an obvious distortion, particularly at the highest drive level. This could represent a diaphragm distortion, a leak opened during high drive levels or even a thermal effect as the voice coil heats. At  $\pm 0.15$  Volts drive, with an open backing, there is a high-cut effect as well. Signals with the backing volume closed are substantially smaller and undistorted. The use of a small sealed backing volume limits the

diaphragm movement to a linear zone and results in a calibrator with a constant displacement response.

Using the above results, the peak-to-peak volume was calculated for each drive level with and without the closed backing (Figure 19). The volume displacement is linear with drive level in both cases, but the displacement is 9.7 times smaller for a closed backing volume. This seems reasonable based on the ratio of the calibrator backing volume to the microbarograph fore volume. With a closed backing volume the calibrator produces a displacement of about  $0.1 \text{ cm}^3$ , sufficient to calibrate the microbarograph with a closed fore volume, or to inject a signal into the backing volume, but insufficient to drive a system of hoses. The drive efficiency (Figure 20) shows the nonlinearity exhibited by the unbacked system compared to the backed system.

It is impossible to operate the calibrator for extended times with a sealed backing since a small ambient pressure change will change the equivalent spring constant or rupture the diaphragm. To avoid this, a 0.003 in. orifice was used to connect the headphone backing to the drive output. A 100 second,  $\pm 0.45$  Volt, square wave was recorded by the microbarograph operating with a sealed backing volume (Figure 21). Prony's method was used to fit a one pole RC filter to determine the corner frequency. With the 0.003 in. orifice the calibrator had a low cut corner of 1/91 Hz, low enough to calibrate the microbarograph over the full bandwidth.

To demonstrate the calibrator's wideband functionality, four swept sine wave sequences were recorded on an operationally configured microbarograph (capillary leak installed in both the microbarograph and calibrator) (Figure 22). Amplitudes vary depending on the spectral density of the sweep, a function of the time duration, bandwidth, and amplitude, but it is obvious that the amplitude is reasonably constant over several octaves.

A high amplitude broadband calibrator may be used to monitor the state-of-health of a porous hose. One end of the hose was connected to the microbarograph and the other end connected to the calibrator driven by a step sweep from 20 Hz to 2 Hz in 10 increments (Figure 23). The hose resonances appear as peaks at 10 and 8 Hz. The hose was damaged with a small cut halfway along its 50 ft. length. A swept calibration resulted in a reduced and differently shaped response. Repair by taping the hole shut restored the spectra to its original shape and amplitude.

### *Bellows Calibrator*

The bellows calibrator was briefly tested to determine the displacement volume of the system and the range of frequencies which it could produce as well as the amount of harmonic distortion in the mechanical drive. The bellows calibrator was used to determine the response of the previous microbarograph design. In this experiment the motor was replaced with a 1 RPM version to produce a signal close to the instrument low frequency corner. Unfortunately the motor was destroyed by an overvoltage before a complete series of data could be collected.

## References

- Benade, A. H. (1968) On the Propagation of Sound Waves in a Cylindrical Conduit, J. Acoust. Soc Am 44:616-623.
- Burridge, B. (1971) The Acoustics of Pipe Arrays, Geophys. J. R. Astr. Soc. 26:53-69.
- Cook, R. K. And Bedard, A. J, Jr (1971) On the measurement of Infrasound. Geophys. J. R. Astr. Soc 26:5-11, 1971.
- Daniels, F. B. (1950) On the Propagation of Sound Waves in a Clindrical Conduit. J. Acous. Soc. Am 22:563-564.
- Daniels, F. B. (1959) Noise-reducing line microphone for frequencies below 1 cps, J. Acous. Soc. Am. 31:529-531.
- Haak, H. W. and de Wilde, G. J. (1996) Microbarograph Systems for the infrasonic detection of nuclear explosions. Royal Netherlands Meteorological Institute Seismology Division, August 1996 Scientific Report WR 96-06. 45pp.
- Hayward, C. T. (1996) Preliminary Report: Characteristics of the Broadband Acoustic Sensors Installed in the SMU Lajitas GSE prototype array. Southern Methodist University, Geophysics Department, Open file report. 25 pp.
- McLaughlin, Keith L. (1997) Permiable Hose Characteristics and Noise Reduction for Infrasound Monitoring. Presented at the 1997 SSA Annual Meeting. Abstract available at [http://www.maxwell.com/products/geop/infra\\_ssa97/index.htm](http://www.maxwell.com/products/geop/infra_ssa97/index.htm).
- Reinke, Robert R. (1985) A digital Microbarograph System. AFWLTR 84-142.
- Stachura, Virgil J., Siskind, David E.; and Engler, Alvin J. (1981) Airblast Instrumentation and Measurement Techniques for Surface Mine Blasting. US Dept. Of the Interior, Bureau of Mines, Report of Investigations 8508.

# Illustrations

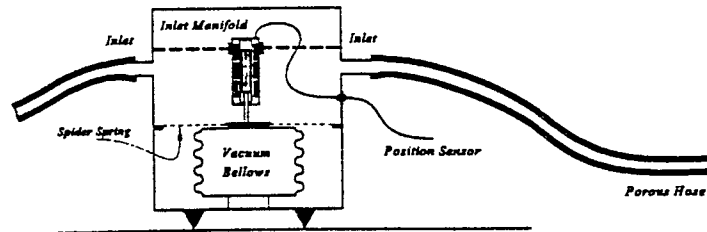


Figure 1. Schematic of an absolute pressure microbarograph (from Haak and Wilde, 1996).

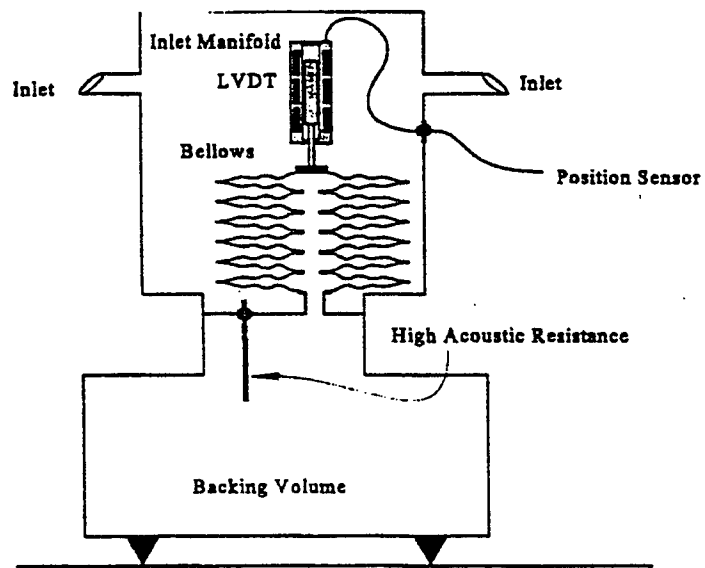
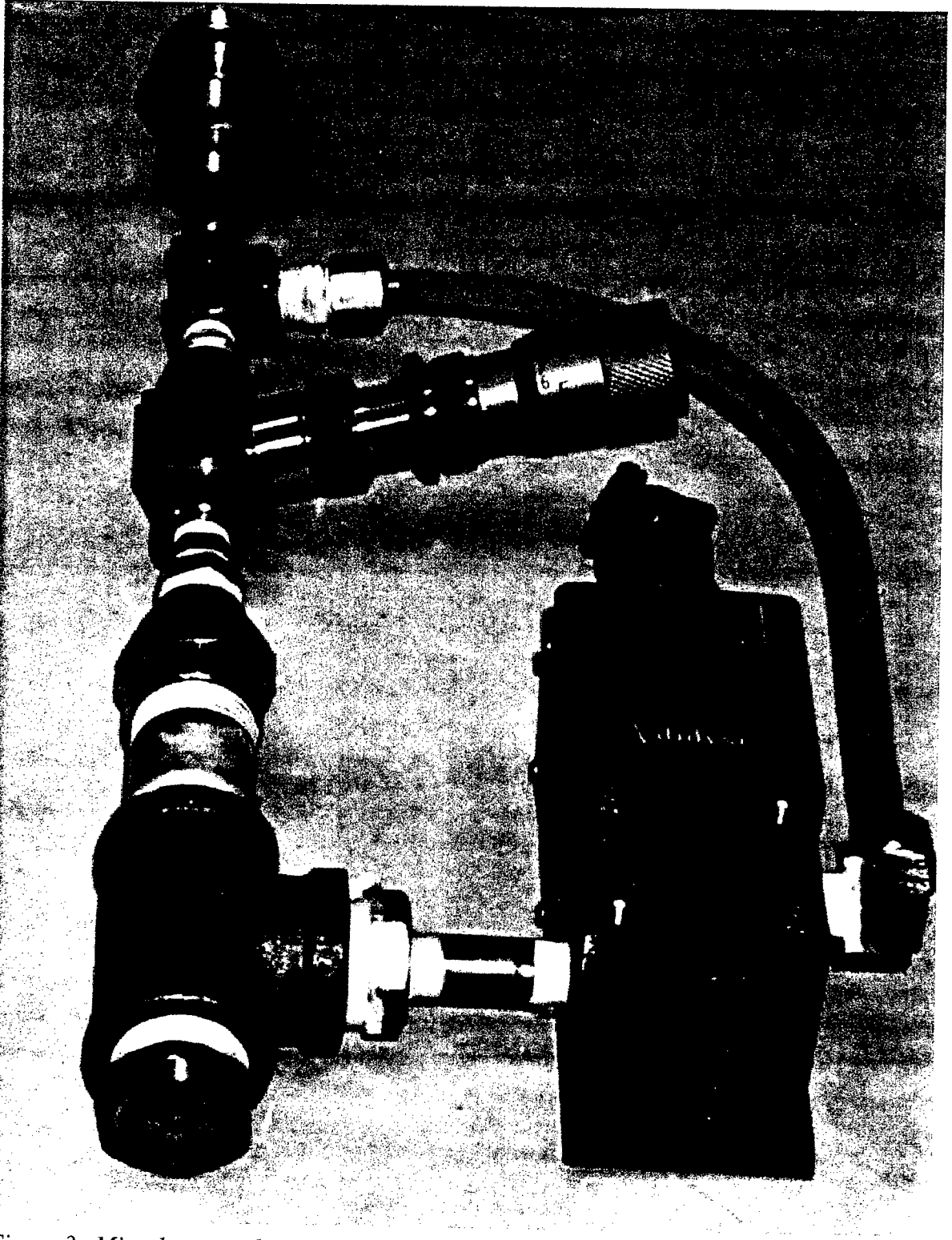


Figure 2. Schematic of a differential pressure microbarograph (from Haak and Wilde, 1996).



*Figure 3. Microbarograph in use at TXAR.*



*Figure 4. Assembled microbarograph.*

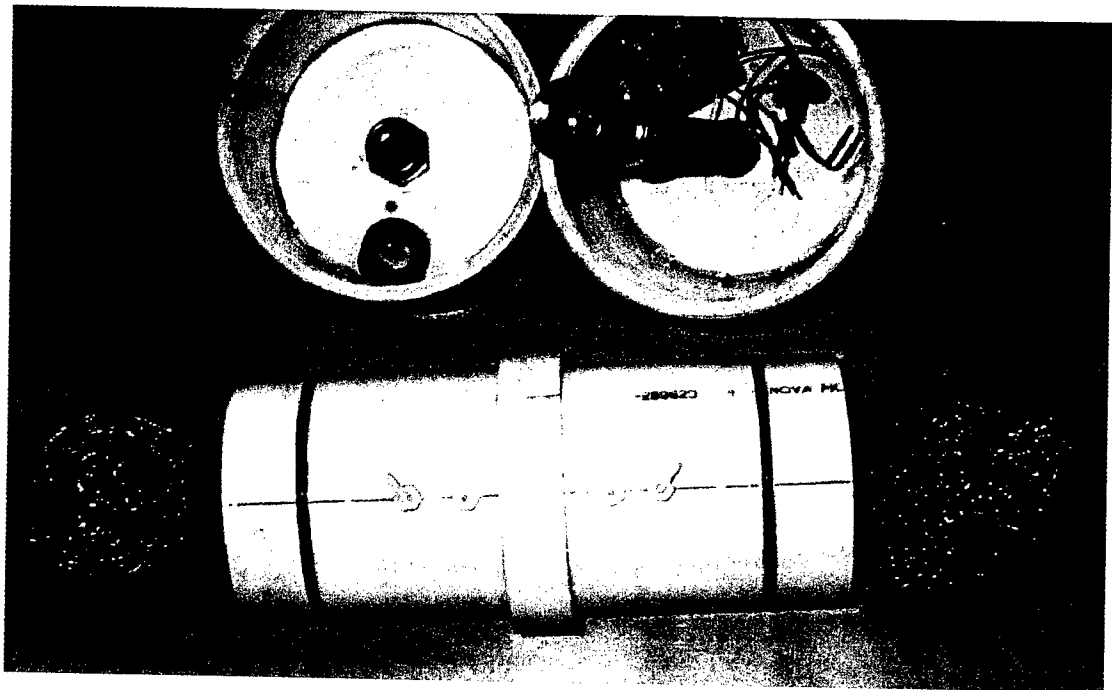


*Figure 5. Open microbarograph. Upper right cap is the top.*

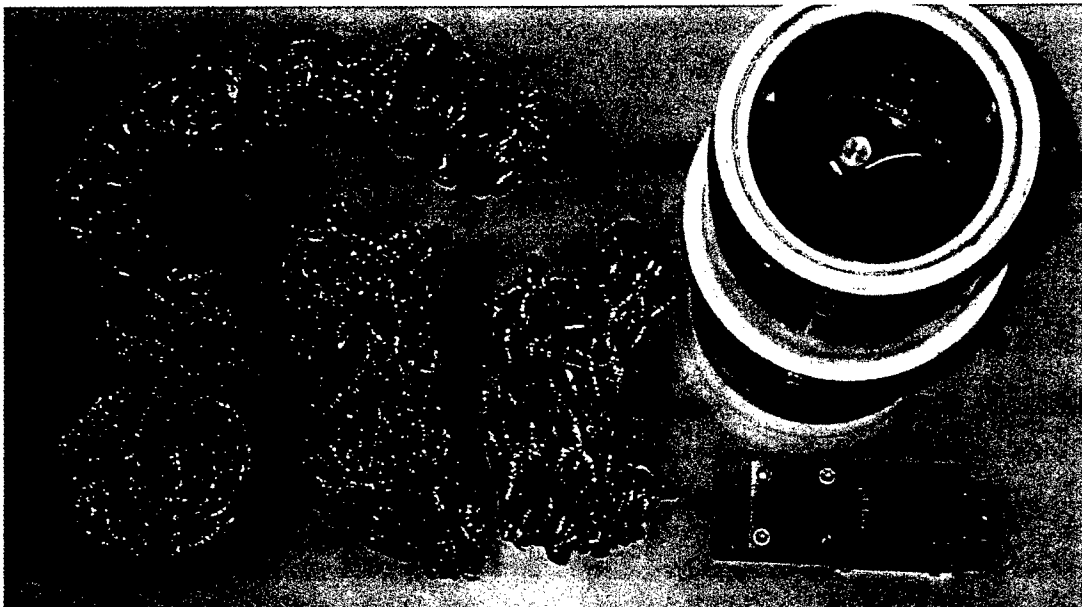
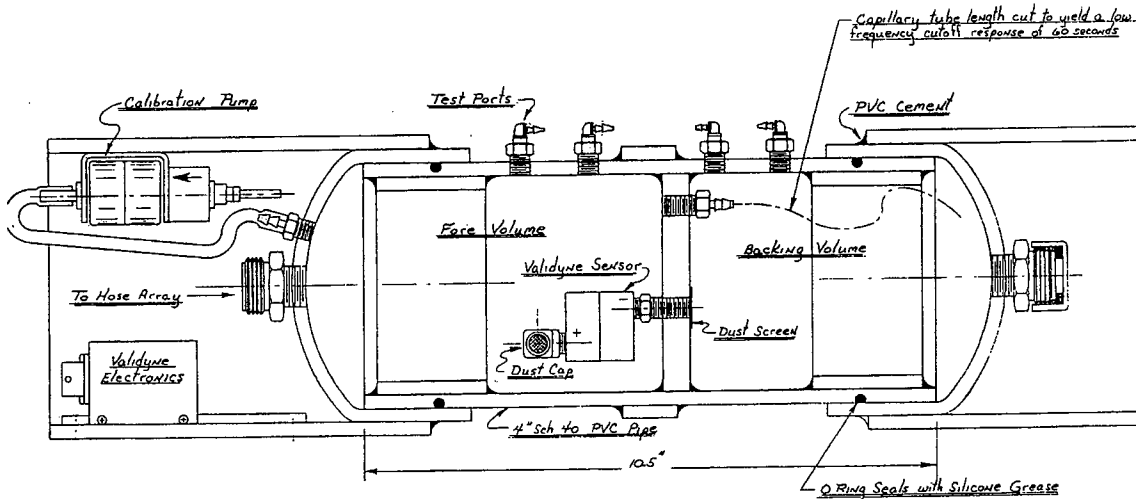
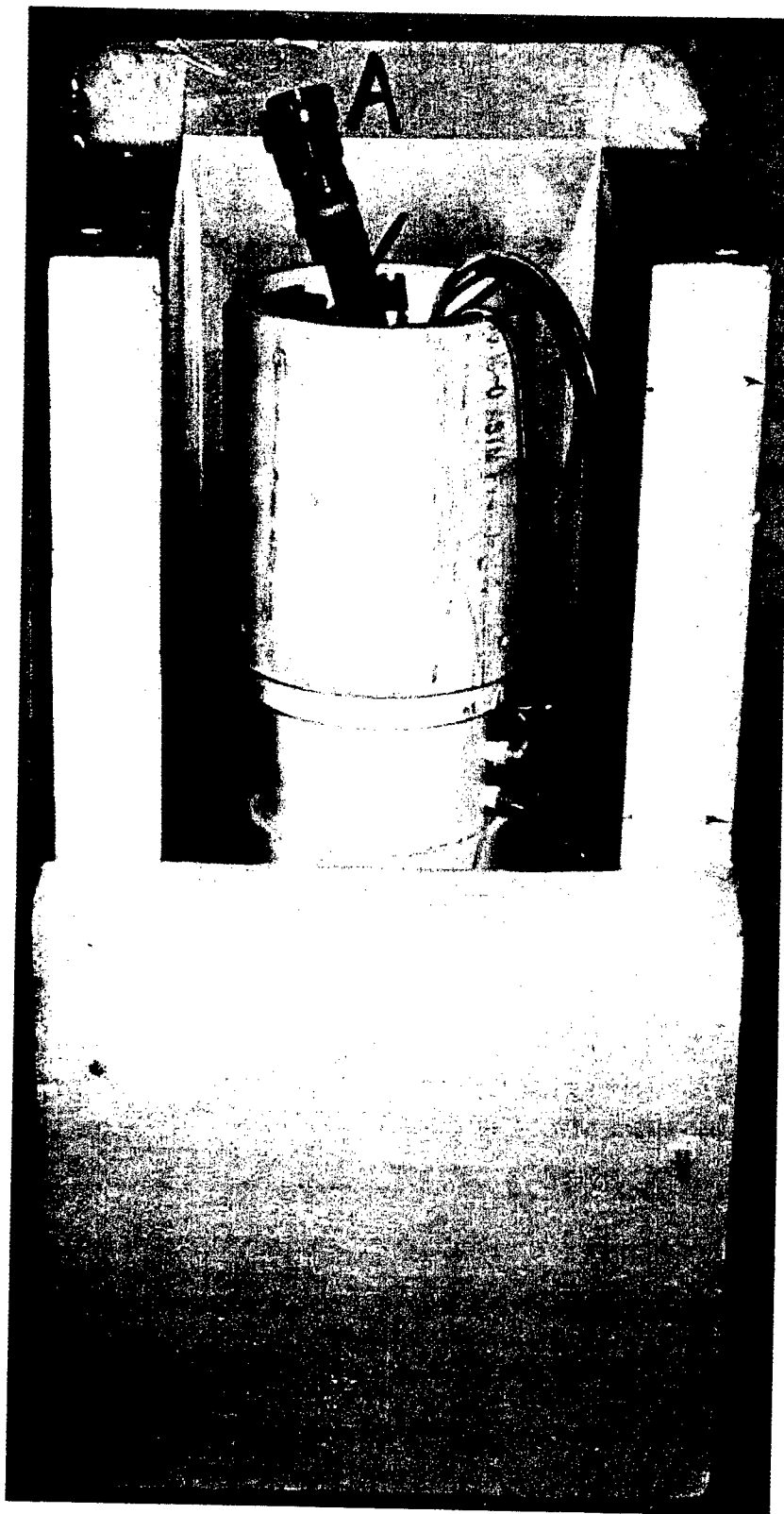


Figure 6. Inside of fore volume. A spare Validyne P305D sensor is shown in the lower left. The Validyne sensor block is visible inside the fore volume. The stainless steel pot scrubbers fill the inside.



INFRASONIC SENSOR ASSEMBLY  
 Southern Methodist University  
 Geological Sciences

Figure 7. Design of the microbarograph built from PVC pipe.



*Figure 8. Microbarograph in insulated cover used during laboratory testing.*

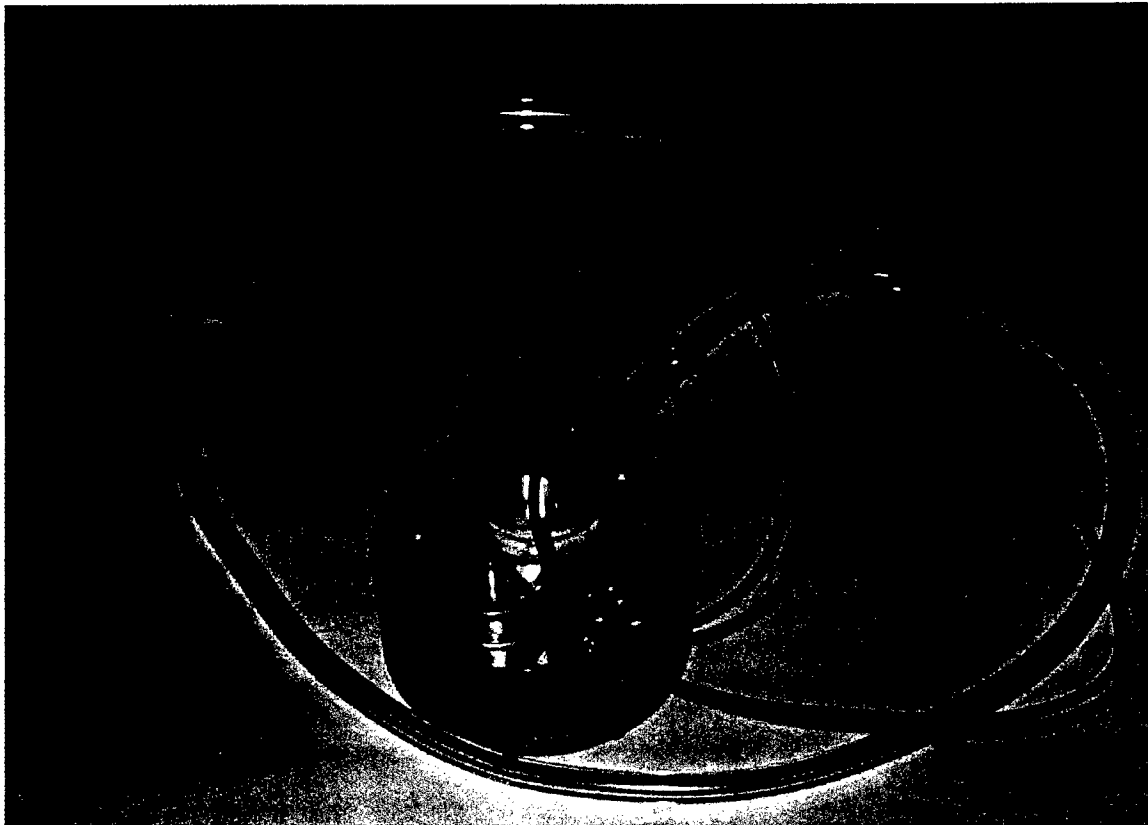


*Figure 9. Modified NBS calibrator.*

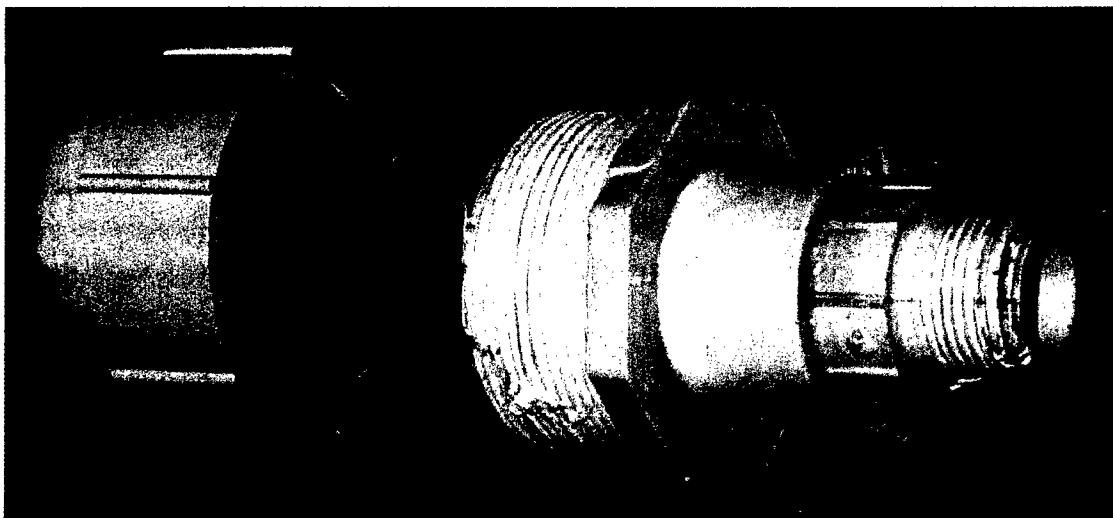


*Figure 10. Headphone calibrator*

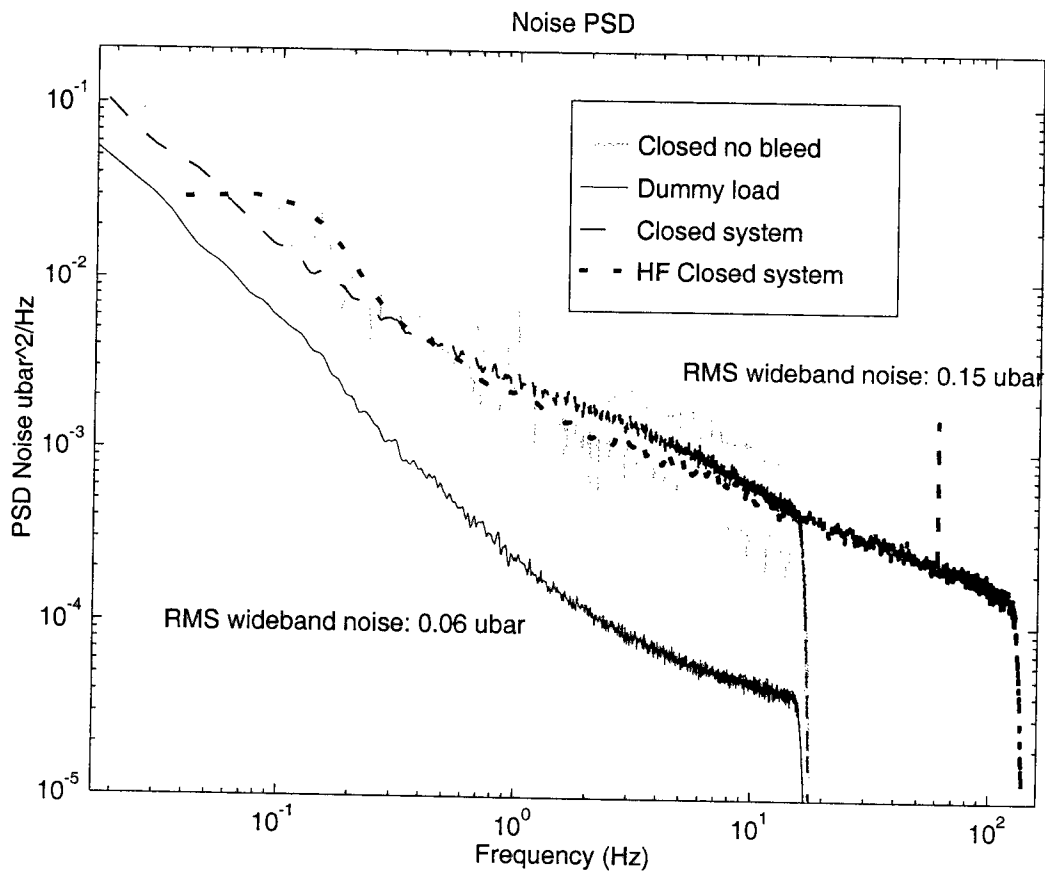


Figure 11. Noise tests of the P305D installed in microbarograph.

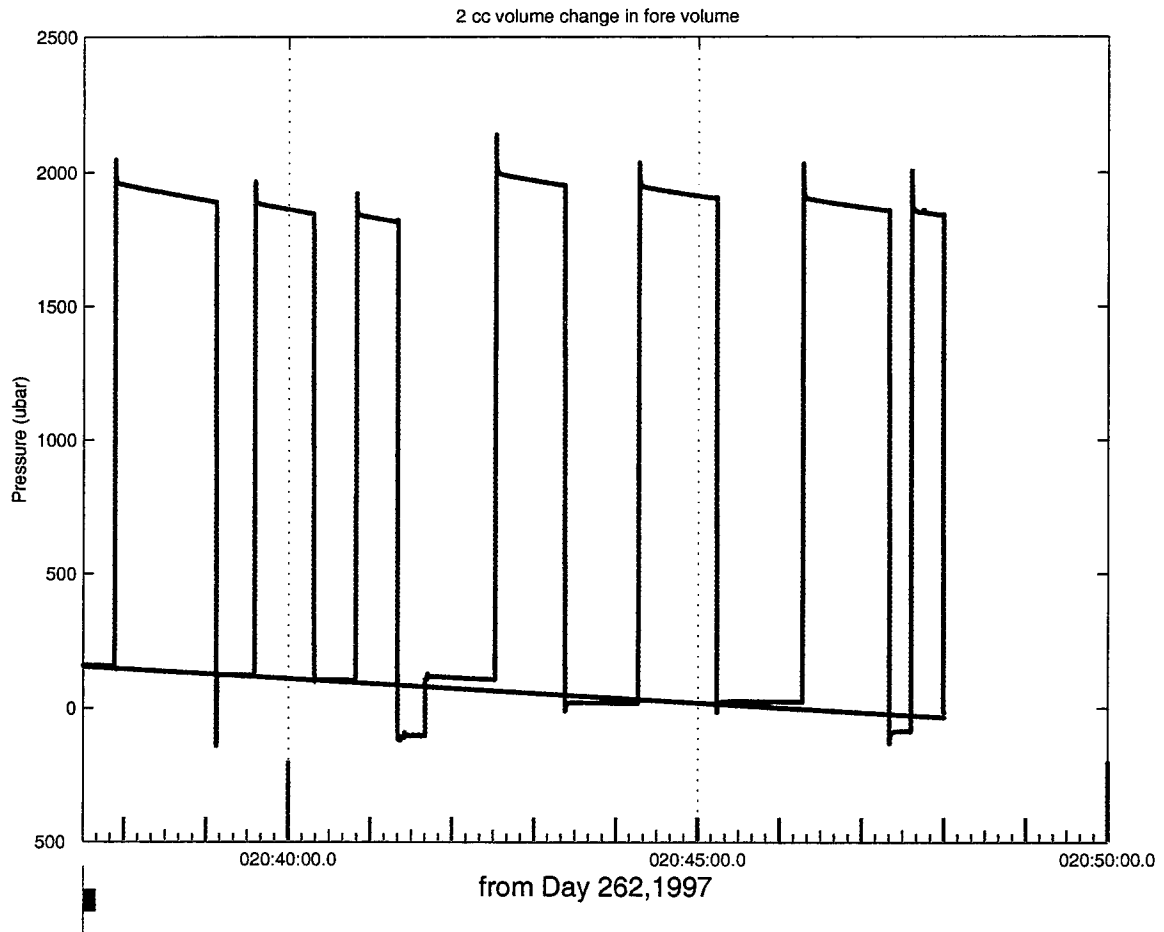


Figure 12. Timeseries from volume measurements.

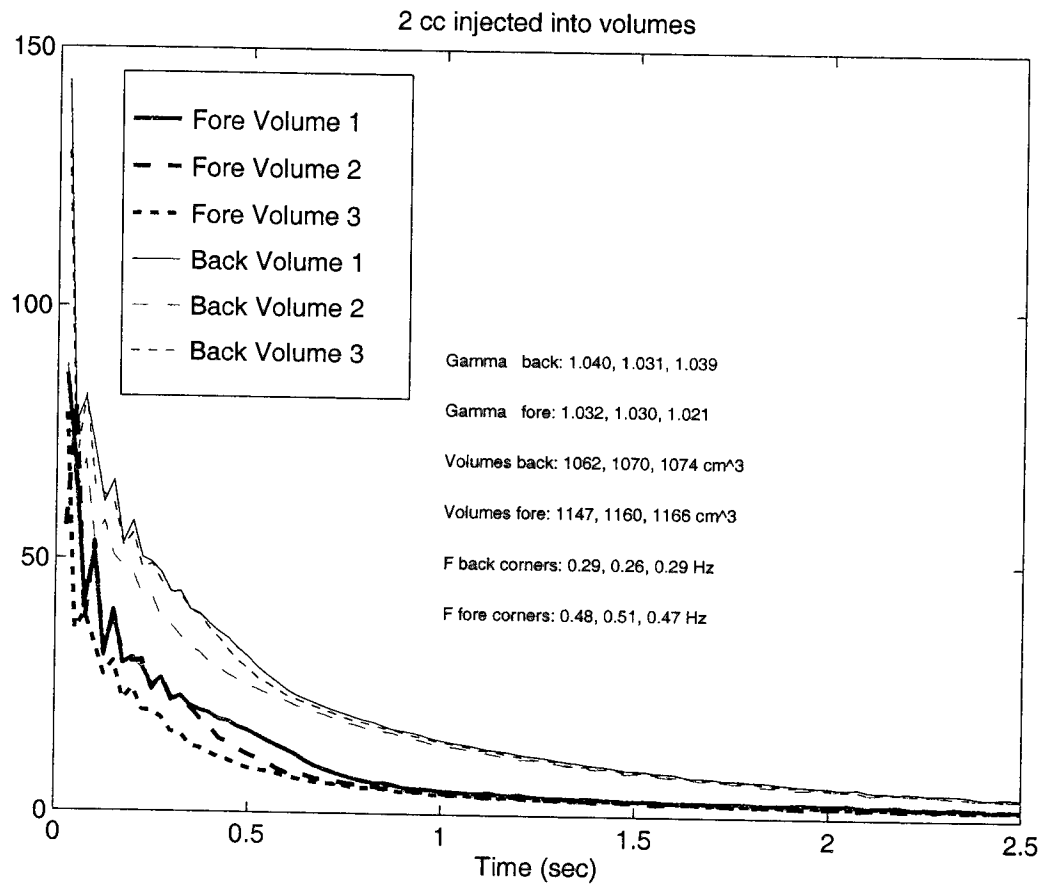


Figure 13. Exponential decays fit to the overshoot.

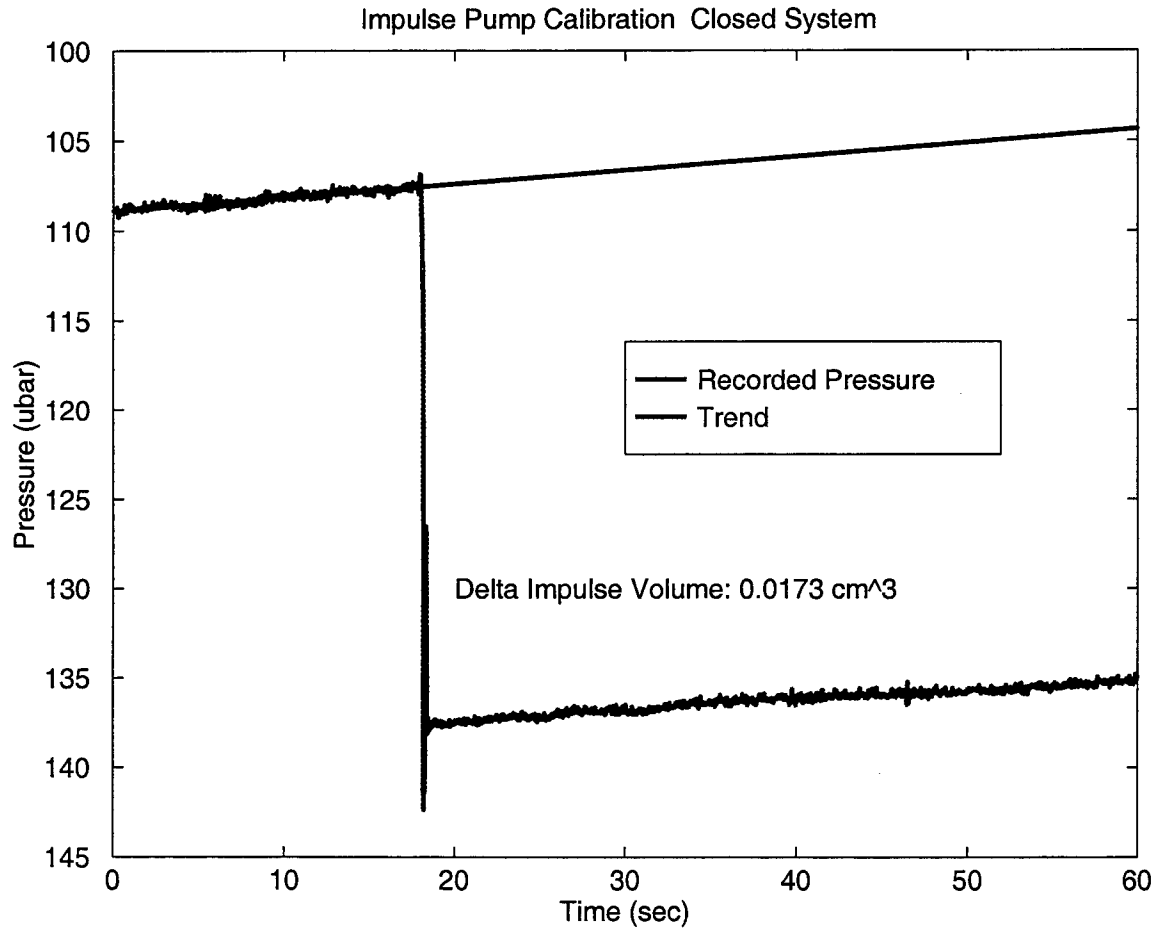


Figure 14. Impulse pump calibrator volume determination.

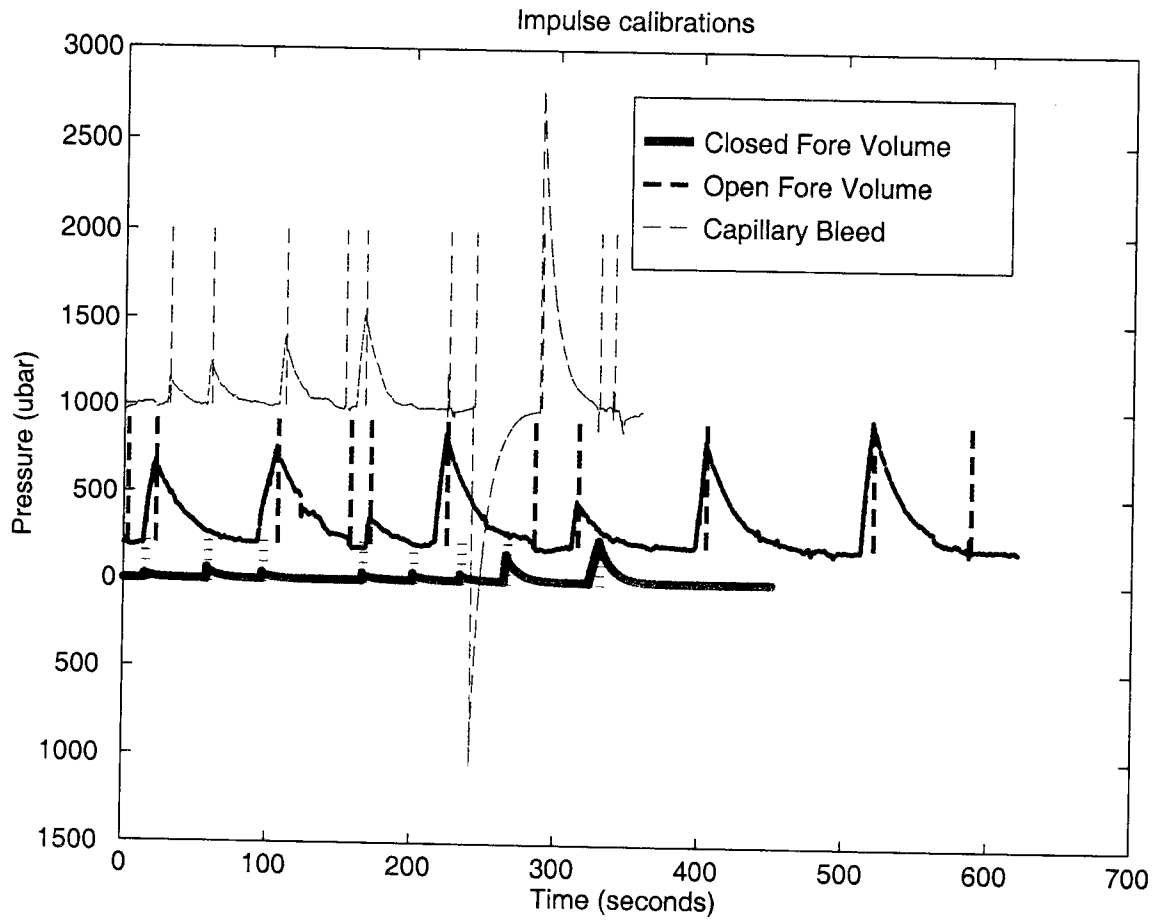


Figure 15. Impulse pump calibration demonstrations.

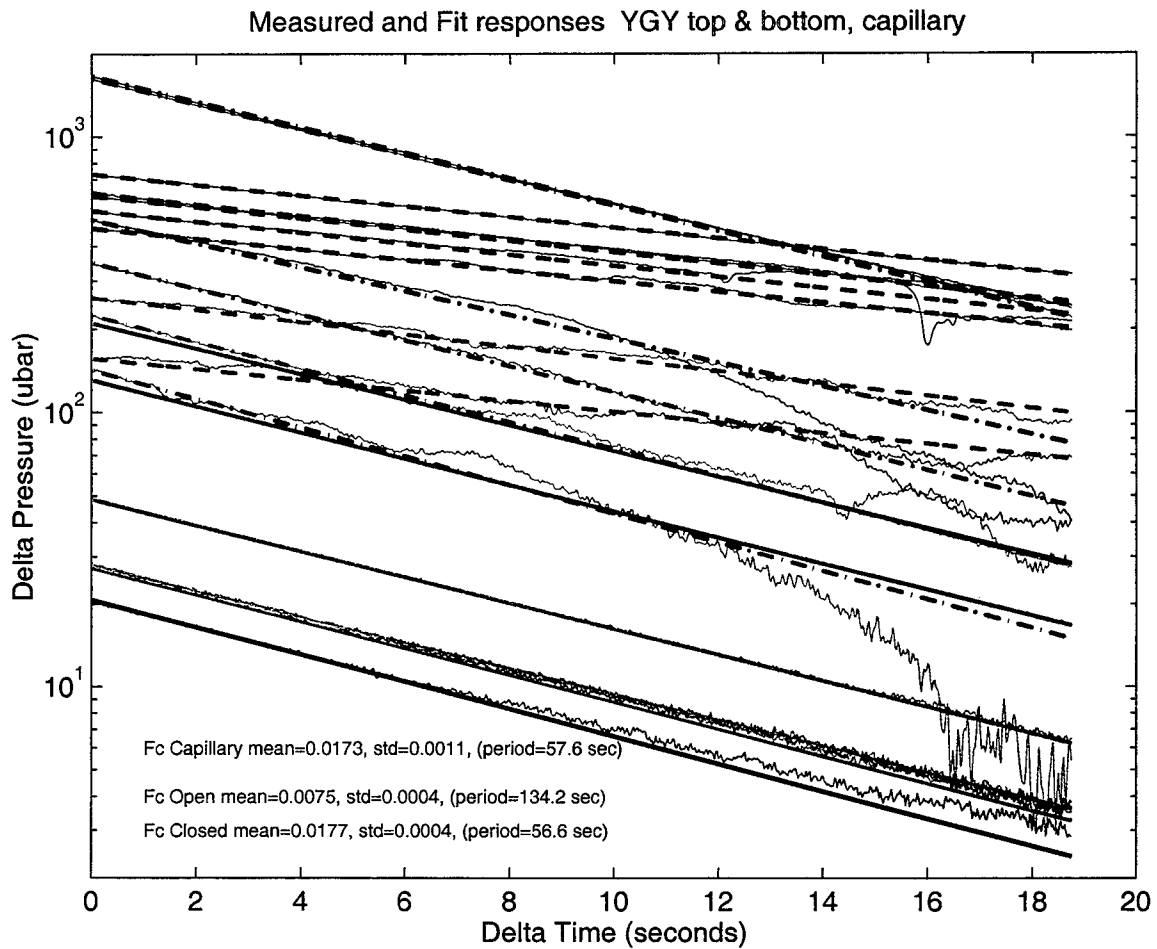


Figure 16. Exponential response curves to impulse calibration.. Fits to test 1 as solid line, to test 2 as dashed line, and to test 3 as dashed-dot line.



Figure 17. Electromagnetic calibrator attached to fore volume.

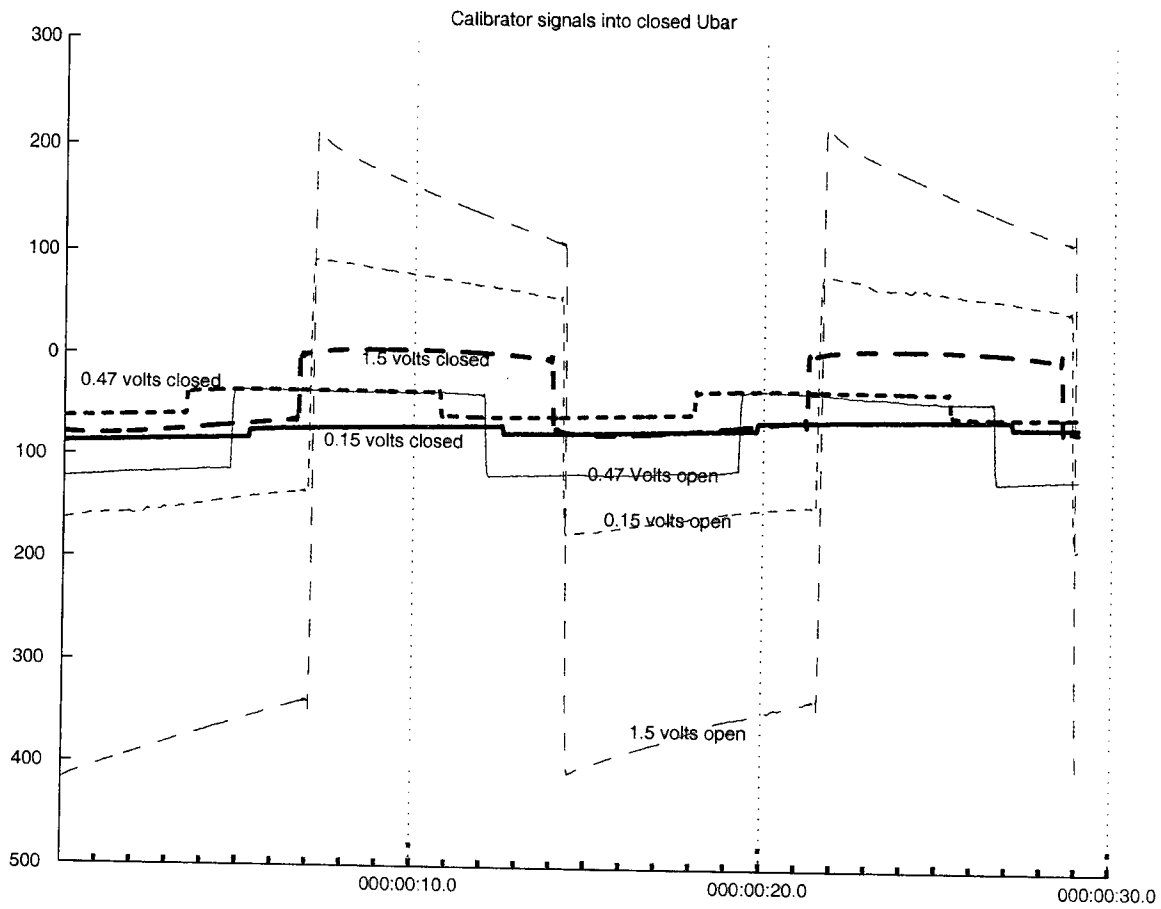


Figure 18. Electromagnetic calibrator demonstration.

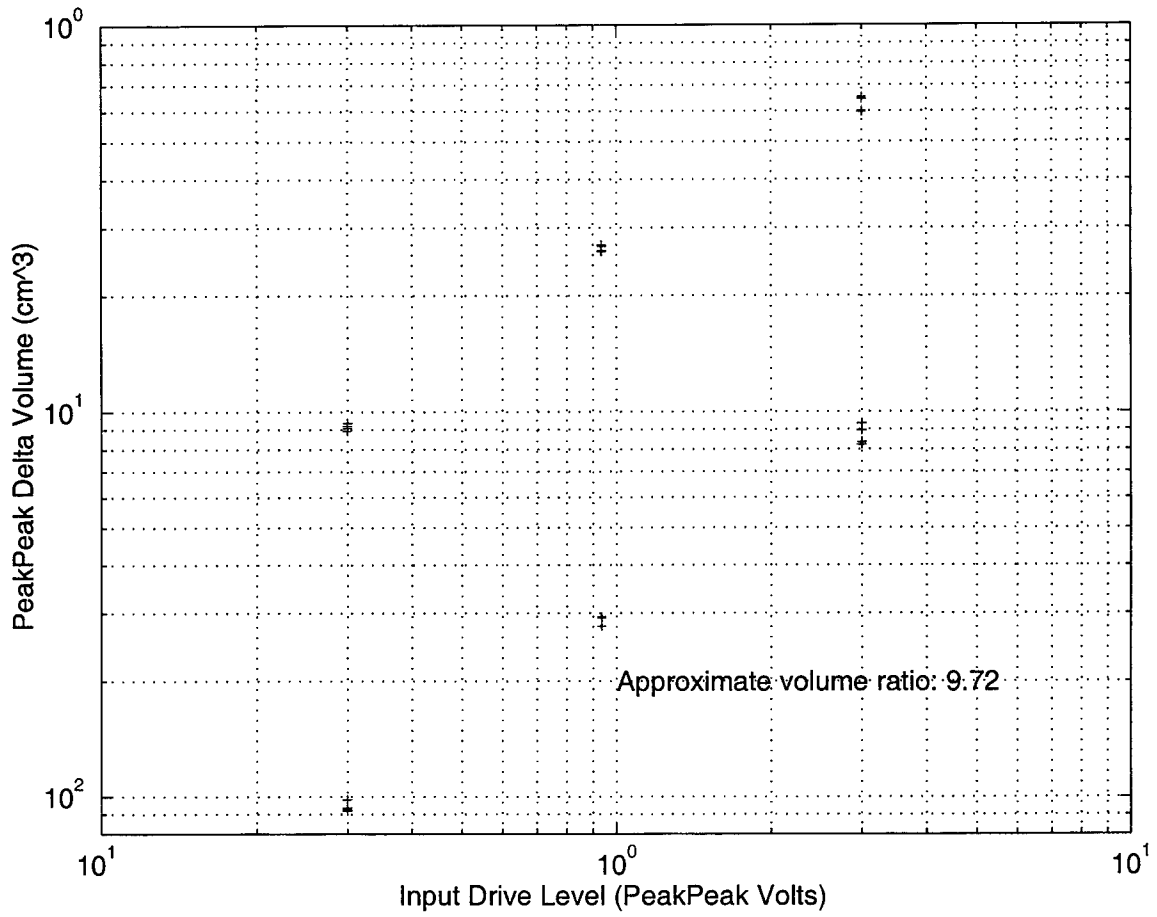


Figure 19. Displacement response of the EM calibrator.

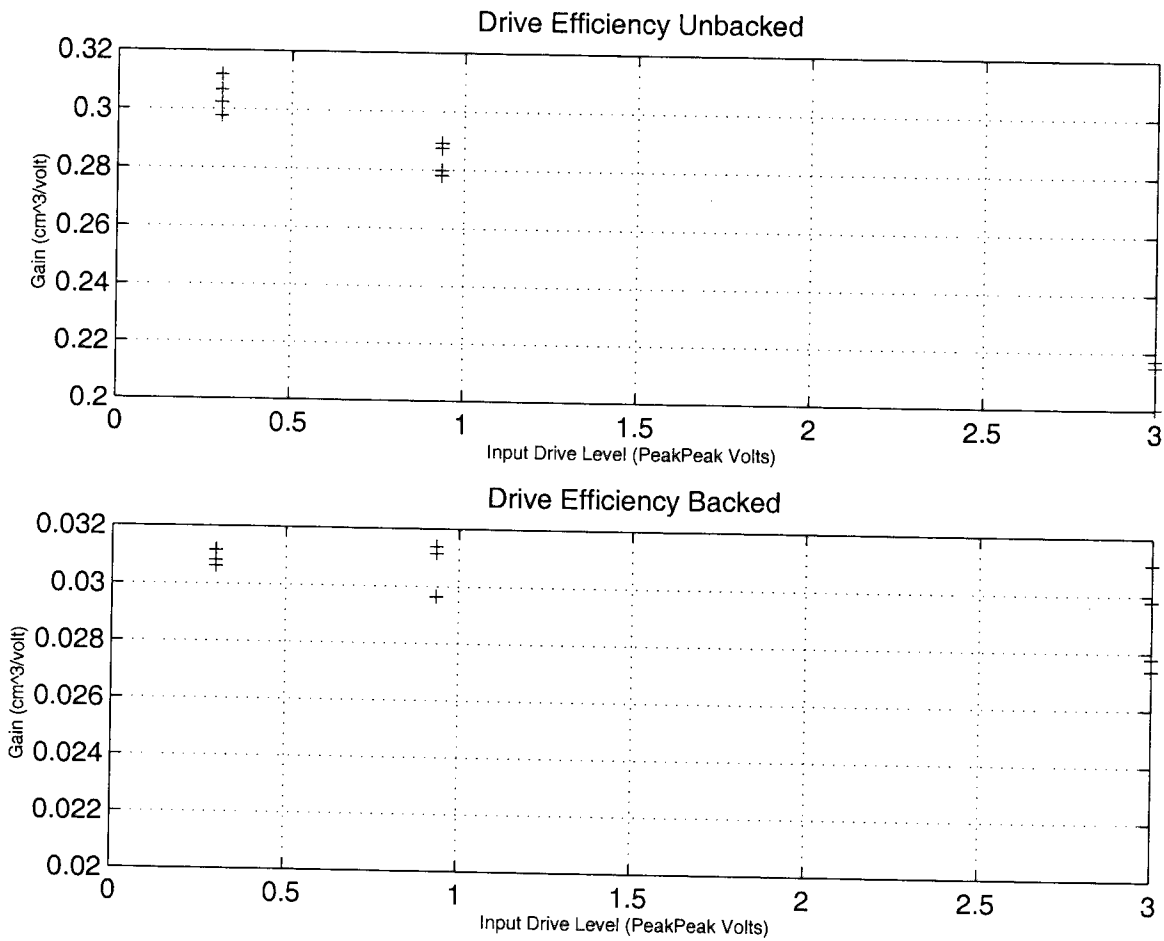


Figure 20. EM Calibrator Efficiency.

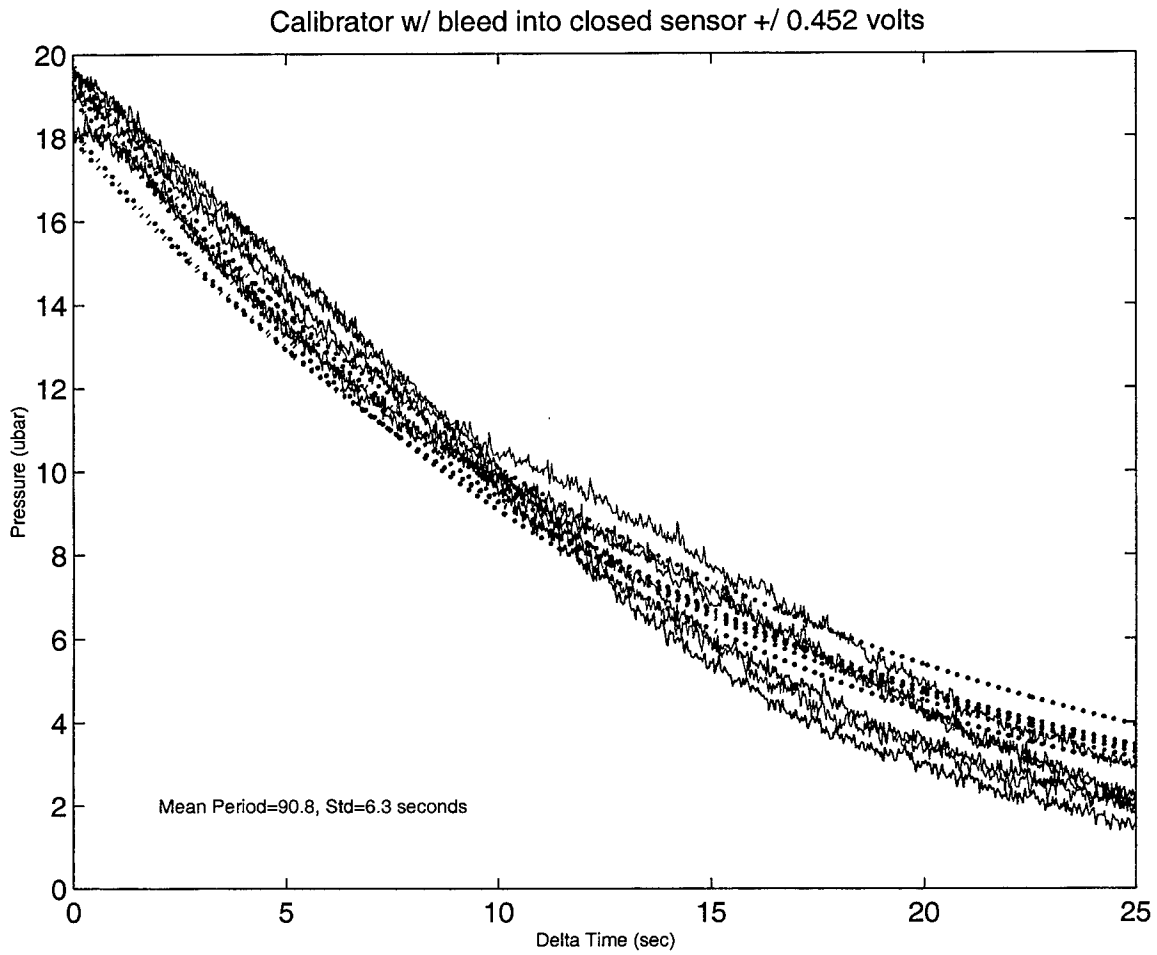


Figure 21. EM Calibrator into closed microbarograph.

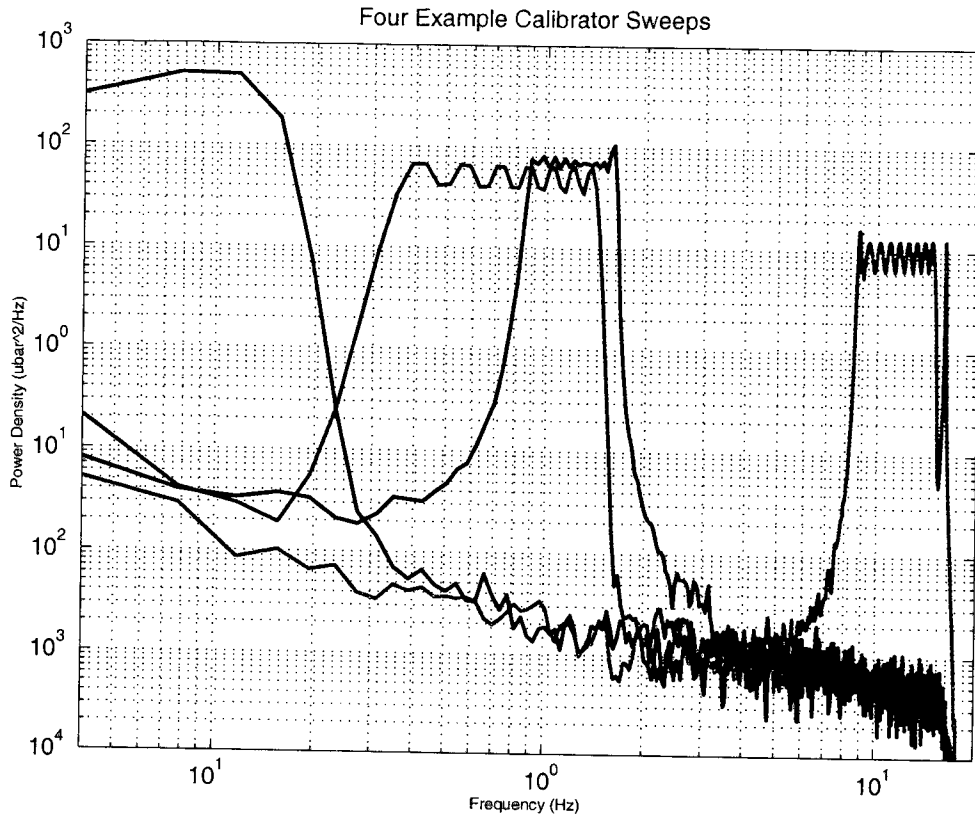


Figure 22. EM calibrator demonstration sweep signals.

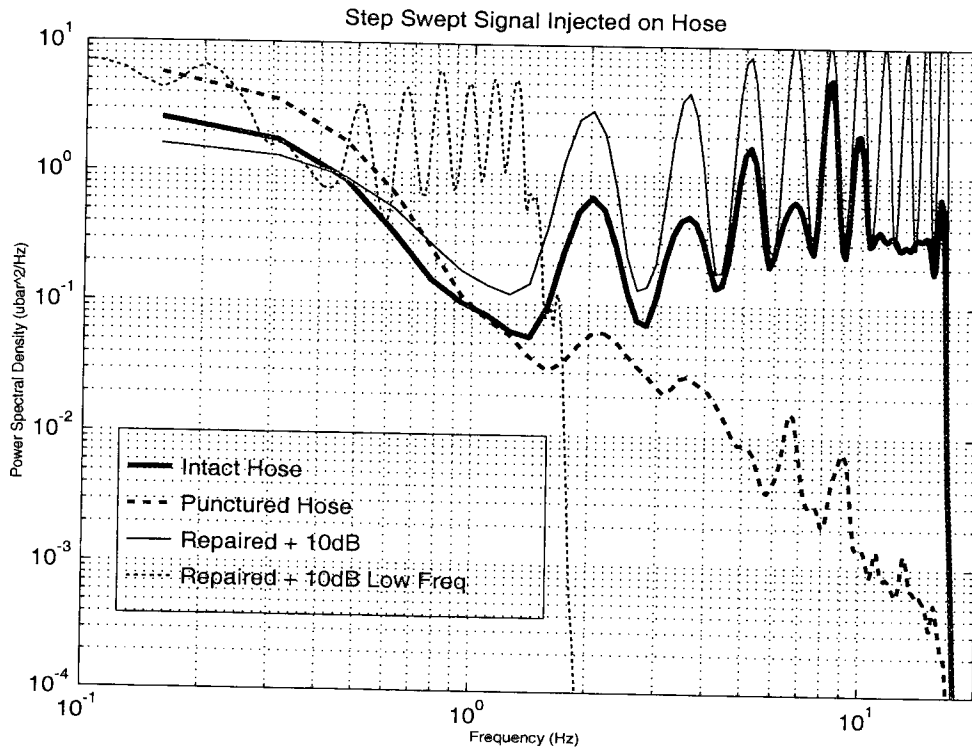


Figure 23. EM calibrator into the end of a porous hose.

## APPENDIX 5. INFRASOUND RECORDINGS OF BOLIDES AND EXPLOSIONS

Jessie Bonner, Paul Golden, and Eugene Herrin

Southern Methodist University operates a four-element acoustic array collocated with a ten-element seismic array (TXAR) near Lajitas, Texas. During the Fall of 1997, three events in West Texas and New Mexico created infrasound signals that were recorded at TXAR and processed by analysts at SMU. These events include a bolide that entered the atmosphere near El Paso, Texas and two large surface (High Energy) explosions from the White Sands Missile Range (WSMR) in south-central New Mexico. For each event, no seismic signal was recorded at TXAR. This fact combined with the size of the infrasound signals and a backazimuth coinciding with the WSMR could bring concerns about the resumption of atmospheric nuclear testing. In the following pages, the results from processing these three events along with plots of the infrasound arrivals as recorded at TXAR are presented.

### El Paso Meteor

On Thursday, October 9, 1997, a series of sonic booms were heard and a fireball (Figure 5-1) was observed by many of the residents of El Paso, Texas and surrounding areas. The cause of these events was a meteorite that entered the atmosphere over West Texas and southern New Mexico. At least four different infrasound arrivals from this event were processed at TXAR (Table I) including the arrivals shown in Figures 5-2 and 5-3.

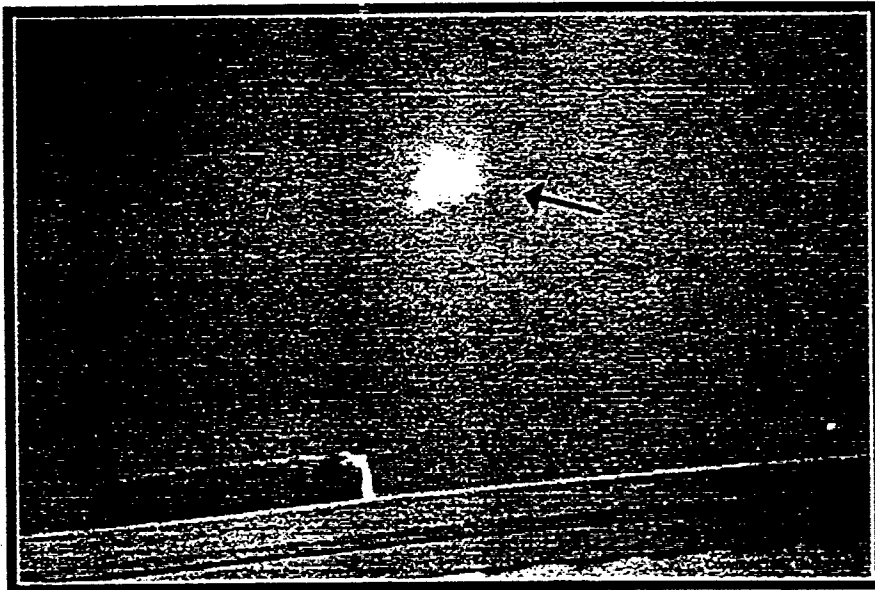


Figure 5-1. Photograph of the El Paso Meteor (Copyright 1997 Bobby Boyd)

Infrasound Arrivals (UTC) <sup>1</sup>	Backazimuth	Phase Velocity (m/sec)	Notes:
19:06:13.6	321.6	348	Small SNR
19:07:54.175	321.0	358	
19:11:38.650	323.9	369	Impulsive
19:11:35	321.8	359	

Table I. Infrasound arrivals at TXAR from the El Paso meteor.

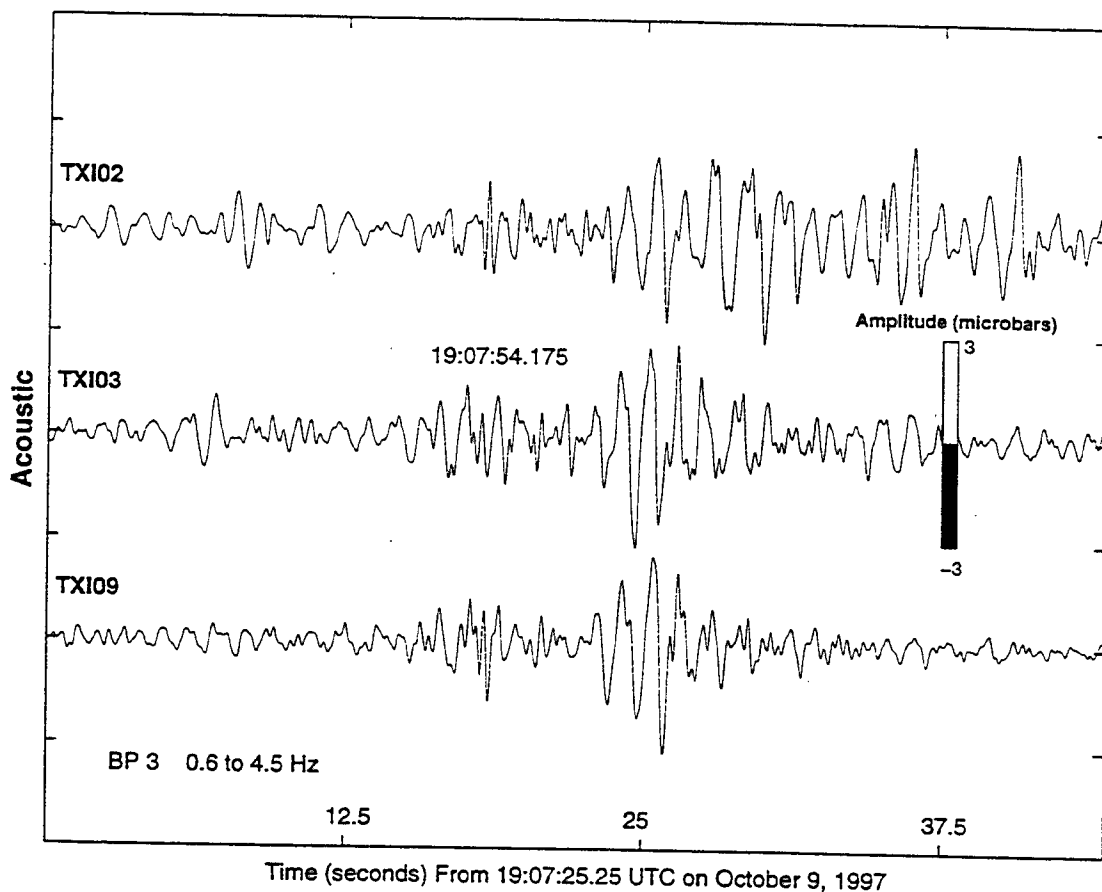
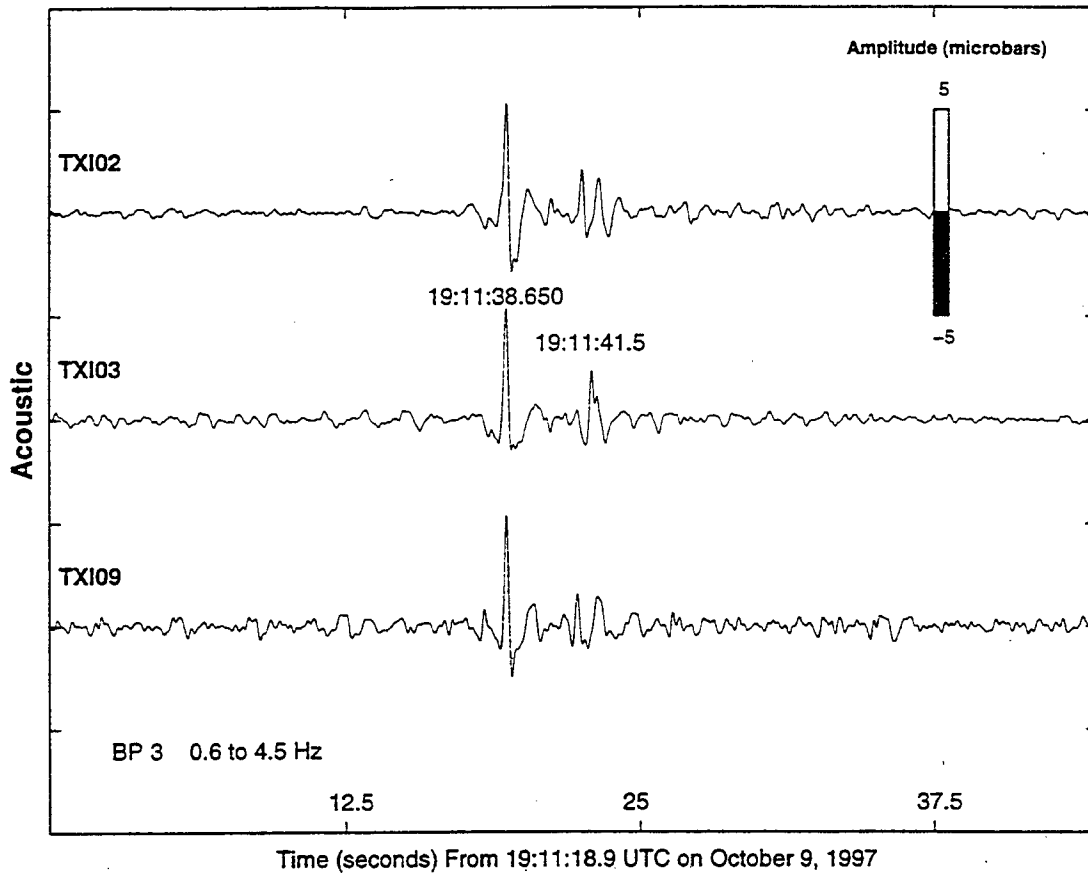


Figure 5-2. Infrasound arrival (19:07:54.175) from the October 9, 1997 El Paso meteor as recorded on the TXAR acoustic array. The traces were aligned to a slowness of 2.793 sec/km and a backazimuth of 321.04°.

<sup>1</sup> At TXI03



**Figure 5-3. Infrasonic arrivals (19:11:38.650 and 19:11:41.5) from the October 9, 1997 El Paso meteor as recorded on the TXAR acoustic array. The traces were aligned to a slowness of 2.710 sec/km and a backazimuth of 323.848°.**

### White Sands Explosive Tests

Explosives tests were carried out on the White Sands Missile Range on November 12, 1997 and November 19, 1997. Each test consisted of detonating C-4 explosives stacked on the ground surface, thus coupling of the seismic energy was limited. This is evident by the fact that seismic energy did not propagate to regional distances, and thus no seismic signals were recorded at TXAR for either blast. Infrasonic signals were recorded for each blast and the results of processing the data is shown in Tables II and III. The signals from the November 12 explosion had less signal-to-noise ratio than the November 19 test (as evident in Figures 5-4 through 5-7) and were difficult to process.

White Sands Explosion#1 12-Nov-97 *10000 lb. C-4 surface*  
 Location: Lat 33.6205 Long 106.4797  
 Distance to TXAR: 552.2 km  
 Backazimuth from TXAR: 331.3°  
 Origin time: 17:47:00.0248

Infrasound Arrivals (UTC)	Backazimuth	Phase Velocity (m/sec)	U (m/sec)
18:16:27.850	332.5	338	313
18:17:46.150	335.3	341	299
18:18:29.050	336.9	342	292

**Table II. Infrasound arrivals from the White Sands test on November 12, 1997.**

White Sands Explosion#2 19-Nov-97 *20000 lb. C-4 surface*  
 Location: Lat 33.6209 Long 106.4797  
 Distance to TXAR: 552.2 km  
 Backazimuth from TXAR: 331.3°  
 Origin time: 18:00:00

Infrasound Arrivals (UTC)	Backazimuth	Phase Velocity (m/sec)	U (m/sec)
18:25:59.375	329.7	340	341
18:28:41.1	332.5	346	321
18:30:29.475	334.2	351	302

**Table III. Infrasound arrivals from the White Sands test on November 19, 1997.**

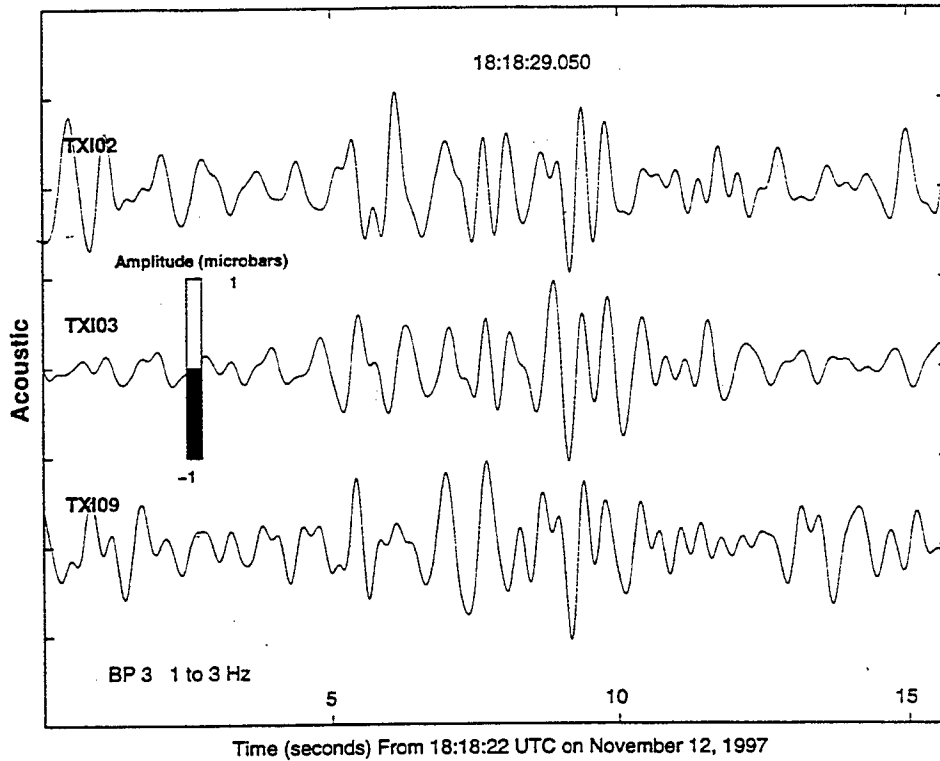


**Figure 5-4. Infrasonic arrival (18:18:29.050) from the November 12, 1997 White Sands explosives test. The traces were aligned to a slowness of 2.934 sec/km and a backazimuth of 336.9°.**

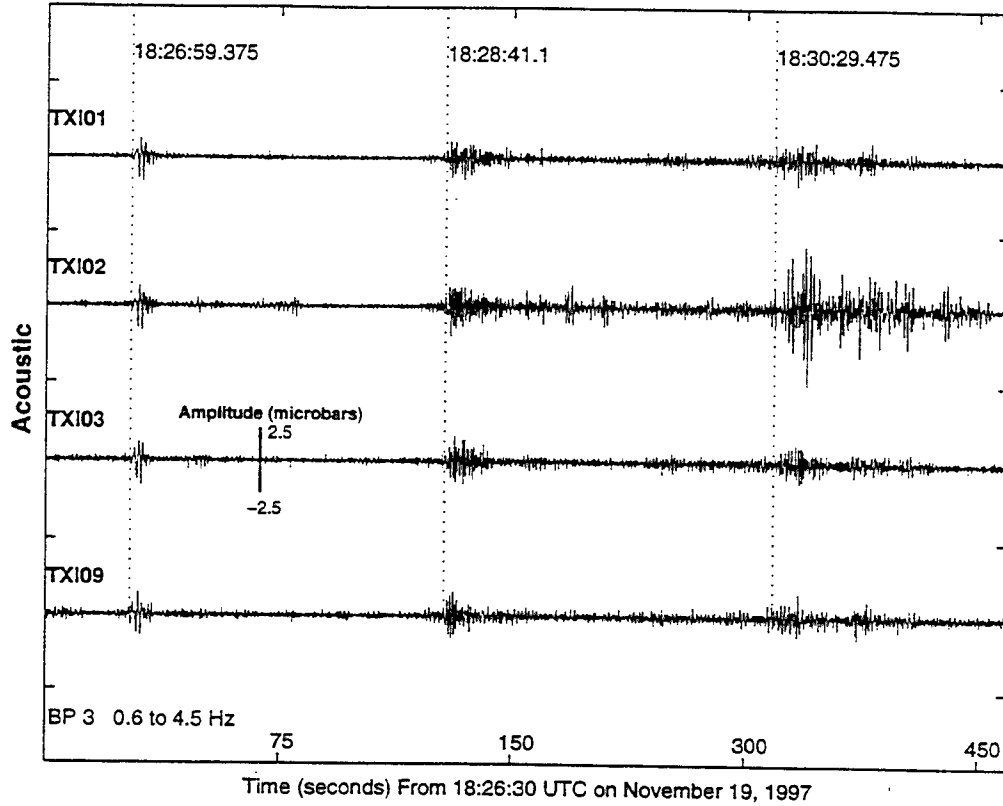


**Figure 5-5. Infrasound arrivals (times shown by vertical lines) from the November 19, 1997 White Sands explosives test. The traces are aligned to a slowness of 2.941 sec/km and a backazimuth of 329.65°.**

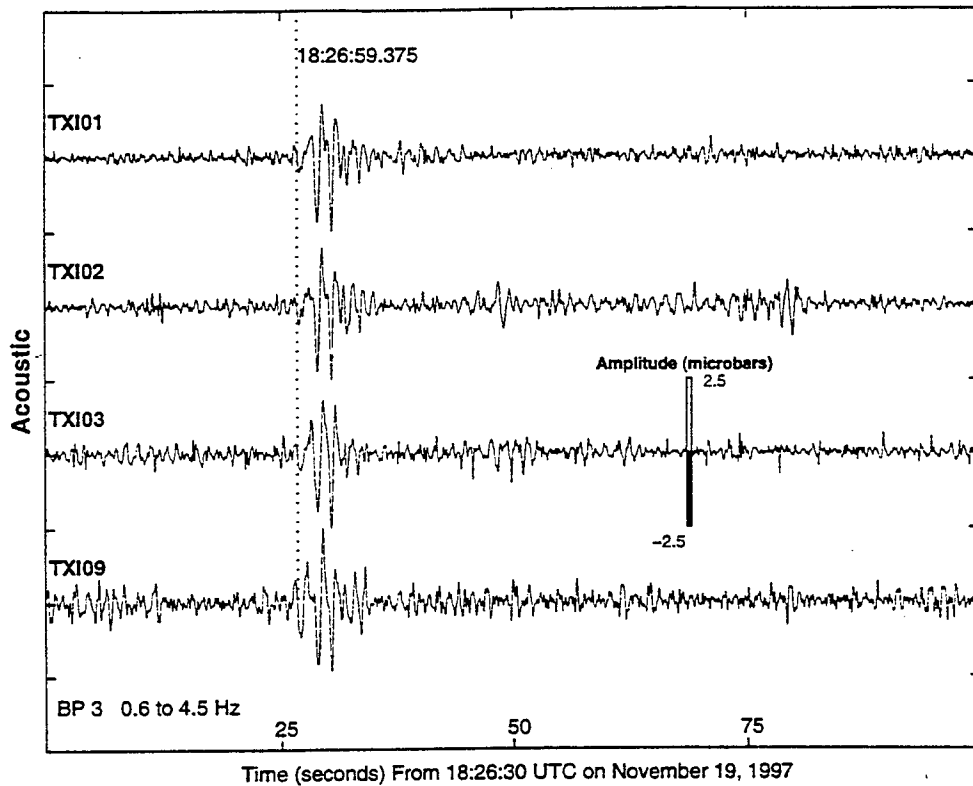


**Figure 5-6. Infrasound arrival (18:26:59.375) from the November 19, 1997 White Sands explosives test. The traces are aligned to a slowness of 2.941 sec/km and a backazimuth of 329.65°.**

## Dispersive Infrasound Arrival

Prior to the November 19, 1997 White Sands test, characteristics for infrasound signals recorded at TXAR fell into two categories: sharp, impulsive types and "ringy" signals dominated by one or two frequencies. The 18:26:59.359 arrival from the 20000 lb. White Sands test (Figure 5-6) is the first noted infrasound signal at TXAR exhibiting dispersion. The signal is normally dispersed between periods of 0.4 and 5 seconds (Figure 5-7). Since the start time for this event is known, a group velocity dispersion

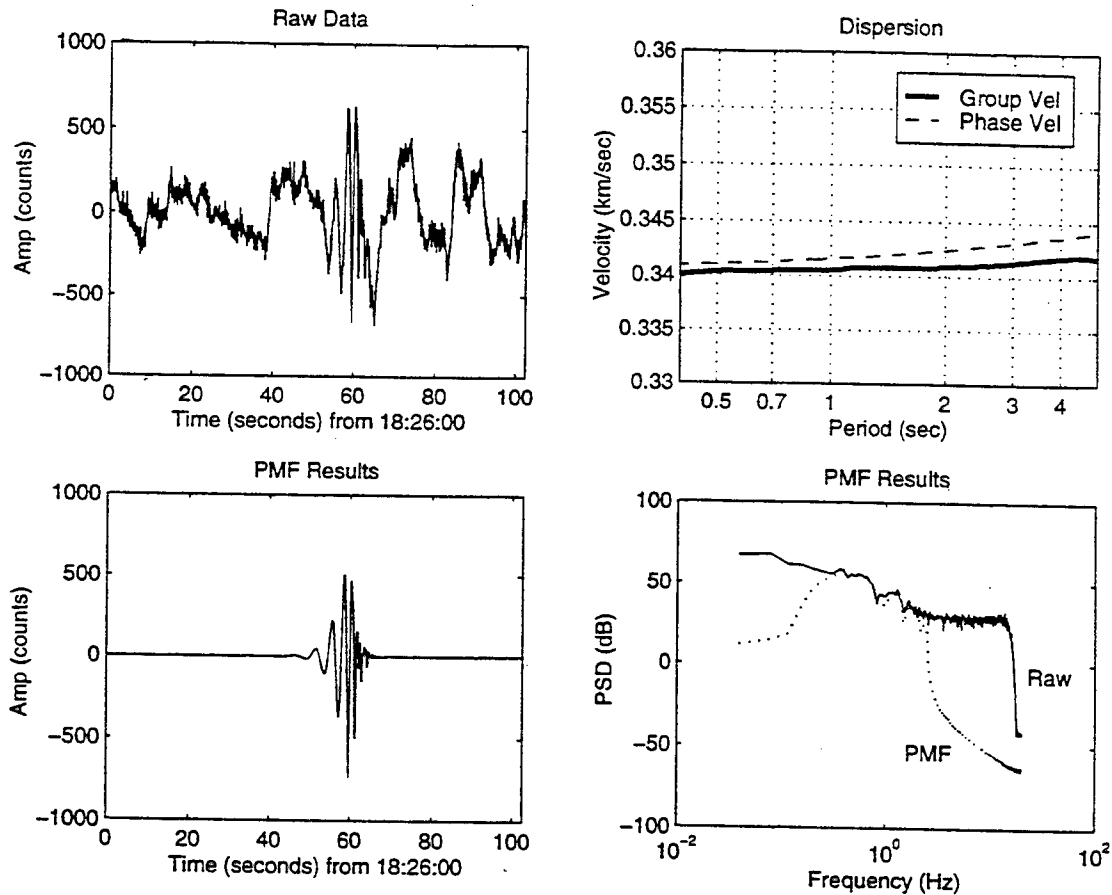


**Figure 5-7. Processing results for the dispersed infrasound arrival from the November 19, 1997 White Sands test. (Upper Left) Raw waveform showing the dispersed signal at approximately 55 seconds into the record. (Upper Right) Dispersion relations for phase and group velocity as obtained from MFA and PMF analysis. (Lower Left) Extracted signal from PMF. (Lower Right) Frequency domain representations of the raw data and the PMF extracted signal.**

curve was established using Multiple Filter Analysis (MFA). This dispersion curve served as the input to the Phase Match Filter (PMF) technique which allowed the

extraction of the dispersed acoustic signal in the time and frequency domains (Figure 5-7). The cause for the dispersion is under investigation.

## DISTRIBUTION LIST

### DEPARTMENT OF DEFENSE

DEFENSE TECHNICAL INFORMATION CENTER  
8725 JOHN J KINGMAN RD., SUITE 0944  
FORT BELVOIR, VA 22060-6218  
ATTN: DTIC/OCF

DEFENSE THREAT REDUCTION AGENCY  
6801 TELEGRAPH ROAD  
ALEXANDRIA, VA 22310-3398  
ATTN: CP, D LINGER  
ATTN: CPF, M SHORE  
ATTN: CPFG, RONGSONG JIH  
ATTN: CPWCT  
ATTN: CPWT  
ATTN: OST, DR ANTON DAINTY  
ATTN: OST, DR CHARLES GALLAWAY  
ATTN: OST, DR RICHARD A GUSTAFSON

DEFENSE THREAT REDUCTION AGENCY  
ALBUQUERQUE OPERATIONS  
1680 TEXAS ST. SE  
KIRTLAND AFB, NM 87117-5669  
ATTN: CPTP R REINKE

### DEPARTMENT OF DEFENSE CONTRACTORS

ACIS  
6T11 NHB  
WASHINGTON, DC 20505  
ATTN: DR JOHN FILSON

CALIFORNIA, UNIVERSITY AT SAN DIEGO  
SCRIPPS INSTITUTION OF OCEANOGRAPHY  
P O BOX 6049  
SAN DIEGO, CA 92166-6049  
ATTN: DR. MICHAEL A H HEDLIN  
ATTN: PROF. BERNARD MINISTER  
ATTN: PROF. FRANK VERNON  
ATTN: PROF. JOHN A ORCUTT  
ATTN: PROF. JONATHAN BERGER

CENTER FOR MONITORING RESEARCH  
1300 N, 17TH STREET  
SUITE 1450  
ARLINGTON, VA 22209  
ATTN: DR HANS ISRAELSON  
ATTN: DR K L MCLAUGHLIN  
ATTN: DR ROBERT NORTH

CTB TREATY MANAGER  
ROSSLYN GATEWAY  
1901 N. MOORE STREET  
SUITE 609  
ARLINGTON, VA 22209  
ATTN: DR. RALPH W. ALEWINE, III

DALE GLOVER  
8950 SPICEWOOD RUN  
BELL ALTON, MD 20611  
ATTN: DALE GLOVER

DENVER FEDERAL CENTER  
P O BOX 25046  
MAIL STOP 967  
DENVER, CO 80225  
ATTN: DR ROBERT P. MASSE

ENSCO, INC.  
P O BOX 1346  
SPRINGFIELD, VA 22151-0346  
ATTN: DOUGLAS BAUMGARDT  
ATTN: DR ZOLTAN A DER

GEOPEX, LTD.  
WESTON GEOPHYSICAL  
325 WEST MAIN STREET  
NORTHBOROUGH, MA 01532  
ATTN: DR. DELAINE REITER  
ATTN: MR. JIM LEWKOWICZ

ITT INDUSTRIES  
ITT SYSTEMS CORPORATION  
ATTN: AODTRA/DASIAC  
1680 TEXAS ST SE  
KIRTLAND AFB, NM 87117-5669  
ATTN: DASIAC  
ATTN: DASIAC/DARE

MAXWELL LABORATORIES, INC.  
S-CUBED WASHINGTON RESEARCH OFFICE  
11800 SUNRISE VALLEY DRIVE  
SUITE 1212  
RESTON, VA 22091  
ATTN: DR THERON J BENNETT  
ATTN: JOHN R MURPHY

MAXWELL TECHNOLOGIES INC  
FEDERAL DIVISION  
8888 BALBOA AVENUE  
SAN DIEGO, CA 92123-1506  
ATTN: DR G ELI BAKER  
ATTN: DR JEFFREY L STEVENS

MISSION RESEARCH CORP  
8560 CINDERBED ROAD  
SUITE 700  
NEWINGTON, VA 22122  
ATTN: DR. MARK FISK

MULTIMAX, INC  
1441 MCCORMICK DRIVE  
LANDOVER, MD 20785  
ATTN: DR INDRA N GUPTA  
ATTN: DR WINSTON CHAN

MULTIMAX, INC  
1441 MCCORMICK DRIVE  
LANDOVER, MD 20785  
ATTN: DR. IVAN HENSON  
ATTN: MS. LORI GRANT

SCIENCE APPLICATIONS INTL CORP  
10260 CAMPUS POINT DRIVE  
SAN DIEGO, CA 92121-1578  
ATTN: DR TOMAS C. BACHE, JR  
ATTN: DR TOMAS J. SERENO, JR

SOUTHERN METHODIST UNIV  
DEPT OF GEOLOGICAL SCIENCE  
P O BOX 395  
DALLAS, TX 75275-0395  
ATTN: CHRIS HAYWARD  
ATTN: DR BRIAN STUMP  
ATTN: E HERRIN  
ATTN: GORDEN SORRELLS  
ATTN: JESSE BONNER  
ATTN: PAUL GOLDEN

ST LOUIS UNIVERSITY  
P O BOX 8148  
PIERRE LACLEDE STATION  
ST LOUIS, MO 63156-8148  
ATTN: PROF. BOB HERRMANN  
ATTN: PROF. BRIAN J MITCHELL

WOODWARD-CLYDE CONSULTANTS  
566 EL DORADO STREET  
PASADENA, CA 91109-3245  
ATTN: DR BRADLEY B. WOODS  
ATTN: DR CHANDAN K. SAIKIA

#### DEPARTMENT OF ENERGY

HEADQUARTERS  
DEPARTMENT OF ENERGY  
FORRESTAL BUILDING  
WASHINGTON, DC 20585  
ATTN: MS LESLIE CASEY, DP-5.1

UNIVERSITY OF CALIFORNIA  
LAWRENCE LIVERMORE NATIONAL LAB  
P O BOX 808  
LIVERMORE, CA 94551-9900  
ATTN: DR. KEVEN MAYEDA  
ATTN: DR. WILLIAM WALTER  
ATTN: L-205 DR JOHN ZUCCA  
ATTN: L-205 MARVIN DENNY

LOS ALAMOS NATIONAL LABORATORY  
P O BOX 1663  
LOS ALAMOS, NM 87545  
ATTN: DR. GEORGE RANDALL  
ATTN: DR. HOWARD PATTON  
ATTN: DR. SCOTT PHILLIPS  
ATTN: MS-F 607 D STEEDMAN  
ATTN: W BRUNISH, MS-F659

SENIOR DIRECTOR  
PACIFIC NORTHWEST LABORATORY  
P O BOX 999  
RICHLAND, WA 99352  
ATTN: DR. DALE ANDERSON  
ATTN: DR. KEVIN ANDERSON  
ATTN: DR. RAY WARNER

SANDIA NATIONAL LABORATORIES  
ATTN: MAIL SERVICES  
P O BOX 5800  
ALBUQUERQUE, NM 87185-0459  
ATTN: DR. DALE BREIDING, DIV 98241  
ATTN: DR. ERIC P. CHAEL, DIV 9241  
ATTN: DR. LARRY S WALKER, DIV 98241  
ATTN: DR. RALPH KEYSER, DIV 9241

#### DEPARTMENT OF THE AIR FORCE

AIR FORCE TECHNICAL APPLICATIONS CENTER  
1300 17TH STREET R  
SUITE 1450  
ARLINGTON, VA 22209  
ATTN: ROBERT BLANDFORD

AIR FORCE TECHNICAL APPLICATIONS CTR/TTA  
1030 S HIGHWAY AIA  
PATRICK AFB, FL 32925-3002  
ATTN: CA/STINFO  
ATTN: DR BOB KEMERAIT  
ATTN: DR GORDAN CROFT  
ATTN: DR JOHN DWYER  
ATTN: DR. DAVID RUSSELL  
ATTN: DR. RICK SCHULT  
ATTN: FRANK PILOTTE/TT  
ATTN: MR. MATTHEW SIBOL

#### DIRECTORY OF OTHER (LIBRARIES AND UNIVERSITIES)

ARIZONA, UNIVERSITY OF  
DEPT. OF GEOSCIENCES/SASO  
TUCSON, AZ 85721  
ATTN: PROF. SUSAN L BECK  
ATTN: PROF. TERRY C. WALLACE

BOSTON COLLEGE  
24 MARTHA'S POINT ROAD  
CONCORD, MA 01742  
ATTN: PROF. DAVID G. HARKRIDER

CALIFORNIA INSTITUTE OF TECHNOLOGY  
DIVISION OF GEOLOGY & PLANETARY SCIENCES  
PASADENA, CA 91125  
ATTN: PROF. DONALD V HELMBERGER  
ATTN: PROF. THOMAS J AHRENS

CALIFORNIA-DAVIS, UNIVERSITY OF  
DAVIS, CA 95616  
ATTN: R. H. SHUMWAY, DIV STATISTICS

CALIFORNIA-SANTA CRUZ, UNIVERSITY OF  
INSTITUTE OF TECTONICS  
SANTA CRUZ, CA 95064  
ATTN: DR. RU SHAN WU  
ATTN: PROF. SUSAN SCHWARTZ  
ATTN: PROF. THORNE LAY

COLUMBIA UNIVERSITY  
LAMONT-DOHERTY EARTH OBSERVATORY  
PALISADES, NY 10964  
ATTN: DR LYNN R SYKES  
ATTN: DR. JACK XIE  
ATTN: DR. WON YOUNG KIM  
ATTN: PROF. ARTHUR LERNER-LAM  
ATTN: PROF. PAUL G RICHARDS  
ATTN: PROF. WILLIAM MENKE

CONNECTICUT, UNIVERSITY OF  
DEPT. OF GEOLOGY & GEOPHICS  
STOORS, CT 06269-2045  
ATTN: PROF. VERNON F CORMIER

CORNELL UNIVERSITY  
DEPT. OF GEOLOGICAL SCIENCES  
SNEE HALL  
ITHACA, NY 14850  
ATTN: PROF. BRYAN ISACKS  
ATTN: PROF. MUAWIA BARAZANGI

HARVARD UNIVERSITY  
HOFFMAN LABORATORY  
20 OXFORD STREET  
CAMBRIDGE, MA 02138  
ATTN: PROF. ADAM DZIEWONSKI  
ATTN: PROF. GORAN EKSTROM

INSTITUTE OF GEOPHYSICS  
8701 NORTH MOPAC  
AUSTIN, TX 78759  
ATTN: PROF CLIFF FROLICH

IRIS  
1200 NEW YORK AVENUE, NW  
SUITE 800  
WASHINGTON, DC 20005  
ATTN: DR DAVID SIMPSON  
ATTN: DR GREGORY E. VAN DER VINK

MASSACHUSETTS INSTITUTE OF TECHNOLOGY  
DEPARTMENT OF EARTH  
ATMOSPHERIC AND PLANETARY SCIENCES  
CAMBRIDGE, MA 02139  
ATTN: PROF THOMAS H JORDAN

MASSACHUSETTS INSTITUTE OF TECHNOLOGY  
EARTH RESOURCES LABORATORY  
42 CARLETON STREET  
CAMBRIDGE, MA 02142  
ATTN: DR. WILLIAM RODI  
ATTN: PROF. M. NAFI TOKSOZ

NEW MEXICO STATE UNIVERSITY  
DEPT. OF PHYSICS  
LAS CRUCES, NM 88003  
ATTN: PROF. JAMES NI  
ATTN: PROF. THOMAS HEARN

PENNSYLVANIA STATE UNIVERSITY  
GEOSCIENCES DEPARTMENT  
403 DEIKE BUILDING  
UNIVERSITY PARK, PA 16802  
ATTN: PROF. CHARLES A LANGSTON  
ATTN: PROF. SHELTON ALEXANDER

RICE UNIVERSITY, MS 126  
DEPT. OF GEOLOGY & GEOPHYSICS  
HOUSTON, TX 77005  
ATTN: PROF. ALAN R LEVANDER

SAN DIEGO STATE UNIVERSITY  
DEPT OF GEOLOGICAL SCIENCES  
SAN DIEGO, CA 92182  
ATTN: PROF STEVEN M DAY

SOUTHERN METHODIST UNIVERSITY  
FONDREN LIBRARY  
DALLAS, TX 75275  
ATTN: G MCCARTOR, DEPT OF PHYSICS  
ATTN: H L GRAY, DEPT OF STATISTICS

UNIVERSITY OF CALIFORNIA  
SEISMOGRAPHIC STATION  
475 MCCONE HALL  
BERKELEY, CA 94720  
ATTN: PROF. BARBARA ROMANOWICZ  
ATTN: PROF. LANE R. JOHNSON  
ATTN: PROF. THOMAS V MCEVILLY

UNIVERSITY OF COLORADO  
CAMPUS 583  
BOULDER, CO 80309  
ATTN: DR. ANATOLU L. LEVSHIN  
ATTN: DR. E. ROBERT ENGDAHL  
ATTN: DR. MICHAEL RITZEWOLLER  
ATTN: PROF. CHARLES B. ARCHMBAU

UNIVERSITY OF SOUTHERN CALIFORNIA  
520 SEAVER SCIENCE CENTER  
UNIVERSITY PARK  
LOS ANGELES, CA 90089-0483  
ATTN: PROF. CHARLES G. SAMMIS

UNIVERSITY OF WISCONSIN-MADISON  
DEPT OF GEOLOGY & GEOPHYSICS  
1215 WEST DAYTON STREET  
MADISON, WS 53706  
ATTN: PROF. CLIFORD THURBER

VIRGINIA POLYTECHNIC INSTITUTE  
DEPT OF GEOLOGICAL SCIENCES  
21044 DERRING HALL  
BLACKSBURG, VA 24061  
ATTN: DR. G. A. BOLLINGER

YALE UNIVERSITY  
DEPT. OF GEOLOGY & GEOPHYSICS  
P O BOX 208109  
NEW HAVEN, CT 06520  
ATTN: DR. JONATHAN LEES  
ATTN: PROF. JEFFREY PARK

#### FOREIGN

BUREAU OF MINERAL RESOURCES  
GEOLOGY & GEOPHYSICS  
NUCLEAR MONITORING SECTION  
G.P.O. BOX 378  
CANBERRA, AUSTRALIA  
ATTN: DAVID JEPSEN

CTBTO, VIENNA  
INTERNATIONAL CENTER  
P O BOX 1200  
VIENNA, A-1400 AUSTRIA  
ATTN: DR. HOLLY GIVEN  
ATTN: DR. PETR FIRBAS  
ATTN: DR. STEVE BRATT

GEOPHYSICAL INSTITUTE OF ISRAEL  
HAMASHBIR STREET, 1  
HOLON, 58122 ISRAEL  
ATTN: DR YEFIM GITTERMAN

INSTITUTE FOR DYNAMICS  
OF GEOSPHERES  
RUSSIAN ACADEMY OF SCIENCES  
MOSCOW, RUSSIA  
ATTN: DR. I O KITOV  
ATTN: DR. V V ADUSHKIN

MINISTRY OF DEFENSE/  
PROCUREMENT EXECUTIVE  
ALACKNESS, BRIMPTON  
READING FG7-4RS ENGLAND  
ATTN: DR ALAN DOUGLAS  
ATTN: DR PETER MARSHALL

NATIONAL DEFENSE  
RESEARCH INSTITUTE  
SENIOR RESEARCH OFFICER  
P O BOX 27322  
S-102 54 STOCKHOLM, SWEDEN  
ATTN: MS. EVA JOHANNISSON

NTNF/NORSAR  
P O BOX 51  
N-2007 KJELLER, NORWAY  
ATTN: DR. FRODE RINGDAL  
ATTN: DR. SVEIN MYKKELTVEIT

OBSERVATORIO SAN CALIXTO  
CASILLA 12656  
LA PAZ, BOLIVIA  
ATTN: DR LAWRENCE A DRAKE

RESEARCH SCHOOL OF EARTH SCIENCES  
INSTITUTE OF ADVANCES STUDIES  
G. P. O. BOX 4  
CANABERRA 2601, AUSTRALIA  
ATTN: PROF. BRIAN L.N. KENNETT

RUHR UNIVERSTY/BOCHUM  
INSTITUTE FOR GEOPHYSIK  
P O BOX 102148  
463 BOCHUM 1, GERMANY  
ATTN: PROF. HANS-PETER HARJES

SOCIETE RADIOMANA  
27 RU CLAUDE BERNARD  
75005 PARIS, FRANCE  
ATTN: DR. BERNARD MASSINON

UNIVERSITY OF BERGEN  
INSTITUTE FOR SOLID EARTH PHYSICS  
ALLEGATION 40  
N-5007 BERGEN, NORWAY  
ATTN: R EYSTEIN HUSEBYE

UNIVERSITY OF CAMBRIDGE  
DEPT. OF EARTH SCIENCES  
MADINGLEY RISE, MADINGLEY ROAD  
CAMBRIDGE CB3 0EZ, ENGLAND  
ATTN: PROF. KEITH PRIESTLEY

**OTHER GOVERNMENT**

U.S. DEPARTMENT OF STATE  
OFFICE OF VERIFICATION AND COMPLIANCE  
BUREAU OF ARMS CONTROL  
2201 C STREET, NW  
WASHINGTON, DC 20520  
ATTN: DR. OWEN J SHEAKS  
ATTN: MR. GIL SATEIA  
ATTN: MR. RICHARD J MORROW  
ATTN: MS. MONA DREICER

US DEPARTMENT OF THE INTERIOR  
US GEOLOGICAL SURVEY NATIONAL CENTER  
MILITARY GEOLOGY PROJECT  
12201 SUNRISE VALLEY DRIVE  
RESTON, VA 22029  
ATTN: DR. JOHN FILSON  
ATTN: MS 928/DR R. MATZKO  
ATTN: W LEITH, MS 928